UNIVERSIDADE FEDERAL DO CEARÁ

CENTRO DE CIÊNCIAS

PROGRAMA DE PÓS-GRADUAÇÃO EM QUÍMICA

FERNANDO LIMA DE MENEZES

MAGNETIC NANOPARTICLES: VERSATILE MATERIALS WITH APPLICATIONS IN CATALYSIS

FORTALEZA

2024

FERNANDO LIMA DE MENEZES

MAGNETIC NANOPARTICLES: VERSATILE MATERIALS WITH APPLICATIONS IN CATALYSIS

Thesis presented to the Post Graduate Program in Chemistry at the Federal University of Ceará as a requirement to obtain the Ph.D. degree in Chemistry. Concentration area: Chemistry.

Supervisor: Prof. Dr. Pierre Basílio Almeida Fechine
Co-supervisor: Lillian Maria Uchôa Dutra Fechine

FORTALEZA

2024

FERNANDO LIMA DE MENEZES

MAGNETIC NANOPARTICLES: VERSATILE MATERIALS WITH APPLICATIONS IN
CATALYSIS

> Thesis presented to the Post Graduate Program in Chemistry at the Federal University of Ceará as a requirement to obtain the Ph.D. degree in Chemistry. Concentration area: Chemistry.

Approved on __/__/____

EXAMINATION BOARD

_____

Prof. Dr. Pierre Basílio Almeida Fechine

Universidade Federal do Ceará (UFC)

_____

Prof. Dr. José Heriberto Oliveira do Nascimento

Universidade Federal do Rio Grande do Norte (UFRN)

_____

Prof. Dr. José Cleiton Sousa dos Santos

Universidade da Integração Internacional da Lusofonia Afro-Brasileira (UNILAB)

_____

Prof. Dr. Rafael Melo Freire

Universidad Central de Chile

_____

Prof. Dr. Dráulio Sales da Silva

Universidade Estadual do Vale do Acaraú (UVA)

To my wife, Jéssica, my family and my friends.

ACKNOWLEDGEMENTS

RESUMO

Essa tese de doutorado apresenta uma exploração abrangente da catálise, com processos oxidativos avançados (POAs) e estratégias de imobilização de enzimas usando novos nanocatalisadores. No primeiro trabalho, POAs baseados em sulfato, conhecidos por sua eficácia na degradação de poluentes orgânicos refratários, foram aprimorados por meio da aplicação de nanopartículas (NPs) de FeCo revestidas de carbono. A síntese hidrotérmica desse material, baseada no método do poliol, levou a obtenção de NPs bem caracterizadas com uma fase predominante de FeCo, alcançada em razões específicas de [OH-] / [Metal] = 26 e [Fe] / [Co] = 2. As NPs exibiram morfologia esférica com aglomerados de tamanhos variados e magnetização de saturação influenciada significativamente pela proporção de ferro no sistema reacional. As condições otimizadas de catálise para degradação de Rodamina B foram 5,0 mg de NPs, 2 mM de PMS, pH 7,0 e tempo de reação de 20 minutos, nas quais o potencial do catalisador de FeCo em POAs baseados em sulfato foi demonstrado. Apesar de sua eficácia, foram identificadas preocupações com a lixiviação de metais, exigindo refinamento futuro. O segundo trabalho concentrou-se na síntese de nanopartículas de magnetita revestidas com L-cisteína como matriz de suporte para a imobilização da Lipase A de Candida antarctica (CALA). Empregando uma combinação de interações físicas e ligação covalente, o sistema sintetizado Fe_3O_4@LC-GLU-CALA apresentou rendimento de imobilização e atividade específica superiores em comparação com a adsorção física. Técnicas de caracterização confirmaram o processo bem-sucedido de síntese e imobilização, e o biocatalisador exibiu atividade aprimorada em diversas condições de pH. Os estudos de inativação térmica e de pH revelaram a robustez do sistema, ultrapassando o tempo de meia-vida da CALA livre em mais de 8 vezes a pH 10. O sistema Fe_3O_4@LC-GLU-CALA surge, assim, como uma matriz biocatalítica promissora com aplicações potenciais na produção de biodiesel, síntese de ésteres e precursores farmacêuticos. Esta tese contribui para o design de novos remediadores ambientais e nanocatalisadores para a busca de processos catalíticos sustentáveis e eficientes.

Palavras-chave: nanopartículas magnéticas; catalisador; processos oxidativos avançados; immobilização de enzimas; eficiência catalítica.

ABSTRACT

This doctoral thesis presents a comprehensive exploration of catalysis, encompassing advanced oxidative processes (AOPs) and enzyme immobilization strategies using novel nanocatalysts. In the first work, sulfate-based AOPs, known for their effectiveness in degrading refractory organic pollutants, were enhanced through the application of carbon-coated FeCo nanoparticles (NPs). The hydrothermal synthesis of this material, based on the polyol method, led to the acquisition of well-characterized NPs with a predominant FeCo phase achieved at specific $[OH^-]$ / $[Metal]$ = 26 and $[Fe]$ / $[Co]$ = 2 ratios. The NPs exhibited a spherical morphology with agglomerates of varying sizes and saturation magnetization significantly influenced by the iron proportion in the reaction system. Optimized catalytic conditions for Rhodamine B degradation were 5.0 mg of NPs, 2 mM PMS, pH 7.0, and a 20-minute reaction time, showcasing the potential of the FeCo catalyst in sulfate-based AOPs. Despite its effectiveness, concerns about metal leaching were identified, necessitating future refinement. The second work focused on the synthesis of magnetite nanoparticles coated with L-cysteine as a support matrix for the immobilization of *Candida antarctica* Lipase A (CALA). Employing a combination of physical interactions and covalent bonding, the synthesized Fe_3O_4@LC-GLU-CALA system exhibited superior immobilization yield and specific activity compared to physical adsorption. Characterization techniques confirmed the successful synthesis and immobilization processes, and the biocatalyst displayed enhanced activity under various pH conditions. Notably, thermal and pH inactivation studies revealed the robustness of the system, surpassing the half-life of free CALA by more than 8 times at pH 10. The Fe_3O_4@LC-GLU-CALA system thus emerges as a promising biocatalytic matrix with potential applications in biodiesel production and ester synthesis and pharmaceutical precursors. Collectively, this thesis contributes to the design of novel environmental remediators and nanocatalysts in the pursuit of sustainable and efficient catalytic processes.

Keywords: magnetic nanoparticles; catalyst; advanced oxidation processes; enzyme immobilization; catalytic efficiency.

LIST OF FIGURES

LIST OF TABLES

TABLE OF CONTENTS

1 CHAPTER 1 – INTRODUCTION AND OBJECTIVES

1.1 Introduction

Chemists and engineers explore new processes every day, either to produce novel substances or to enhance the viability of existing production methods. Beyond favorable thermodynamics, economic feasibility often demands swift processes and efficient conversion with minimal impurities, encompassing many principles of Green Chemistry (ANASTAS; EGHBALI, 2009). In this context, catalysts play a crucial role by accelerating reactions through the reduction of activation energies, enabling them to occur at lower temperatures and pressures. To underscore the importance of catalysts, the global catalyst market was valued at USD 29.7 billion in 2022, with an expected annual growth of 4.6% until 2030 (GRANDVIEW RESEARCH, 2023). Crafting the perfect catalyst remains a persistent goal in green science, representing a vital requirement for sustainable industry.

Catalysts are commonly classified into two types based on their phase in the reaction medium. In homogeneous catalysis, closely associated with organometallic chemistry, the catalyst completely dissolves in the reaction medium, allowing catalysis to occur in the same phase as the reactants (COPÉRET *et al.*, 2003). Due to the complete availability and uniformity of active sites, they exhibit high activity and selectivity, and they can be easily designed by altering ligands and metals to achieve specific chemo-, regio-, and enantio-selectivity (GHOBADI *et al.*, 2021). Despite these advantages, challenges in purifying the product and recovering the catalyst, along with low thermal resistance to solvents and pH in some cases, create bottlenecks, limiting the use of this type of catalysis in industry (GHOBADI *et al.*, 2021). Heterogeneous catalysts, on the other hand, are present in about 85% of industrial processes (VOGT; WECKHUYSEN, 2022). Constituting a different phase from the reaction medium, this type of catalytic process occurs at the liquid-solid or gas-solid interface, on specific sites, combining knowledge from surface science and solid-state chemistry (COPÉRET *et al.*, 2003; VOGT; WECKHUYSEN, 2022). Despite advantages such as easy recoverability and higher resistance, heterogeneous catalysts have lower reactivity and selectivity since only a fraction of the total surface area is active, and these sites do not necessarily have identical interaction patterns (GHOBADI *et al.*, 2021; RAI; GUPTA, 2021; VOGT; WECKHUYSEN, 2022). In the quest for a catalyst perfectly aligned with green chemistry, exhibiting high activity and stability, good selectivity, easy recovery and reuse, and low synthesis cost, chemists have

turned to nanotechnology to merge the best of both catalytic types (RAI; GUPTA, 2021; VEISI *et al.*, 2023).

At the nanometer scale, heterogeneous catalysts exhibit unique properties due to their high surface-to-volume ratio (SOMWANSHI; SOMVANSHI; KHARAT, 2020). As a material is finely divided, there is a higher fraction of surface atoms, which are naturally more energetic, and their properties become strongly dependent on size, shape, and structure (GEBRE, 2021; GHOBADI *et al.*, 2021). Thus, nanomaterials can be designed to present specific properties through synthesis control, allowing these catalysts to be precisely calibrated (SOMWANSHI; SOMVANSHI; KHARAT, 2020). The extremely small size, on the other hand, facilitates material dispersion in the reaction medium and increases the availability of active sites, making it act as an almost homogeneous catalyst. In addition to high activity, broad selectivity, and greater stability than homogeneous catalysts, nanostructured catalysts can also be recovered through techniques such as extraction, centrifugation, and filtration, and can be recycled (GEBRE, 2021). Thus, nanocatalysts straddle the border between homogeneous and heterogeneous catalysis, as illustrated in Fig. 1.

Figure 1 – Main advantages (in green) and disadvantages (in red) of homogeneous and heterogeneous catalysts, with the threshold between these two types integrated by magnetic nanocatalysts. This integration combines the primary advantages of both types of catalysis.
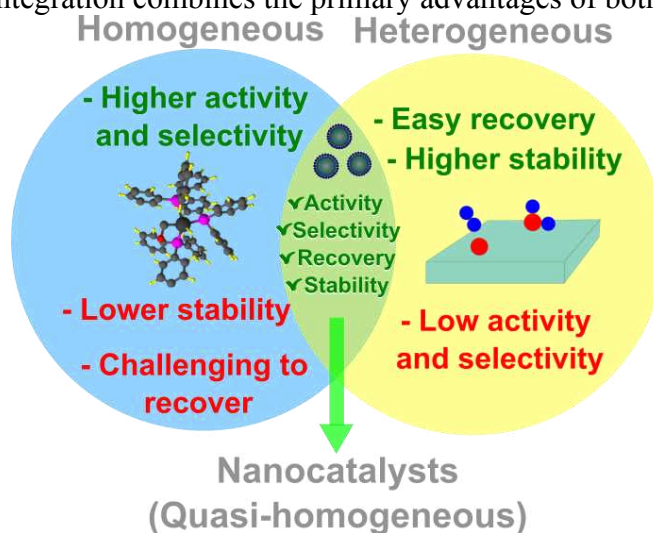
Source: adapted from reference (SOMWANSHI; SOMVANSHI; KHARAT, 2020).

Despite the enormous advantages of nanocatalysts, their recovery for reuse has been a stumbling block in some cases, as their small sizes and high dispersion lead to more laborious, less efficient, and time-consuming recycling processes than in heterogeneous catalysis (GHOBADI *et al.*, 2021). In this context, a class of nanostructured materials that has stood out is magnetic nanoparticles because an external mechanism, such as a magnetic field generator,

could recover the dispersed material. Although the suitable magnetic property for this separation method (superparamagnetism) initially restricted applications to the range of magnetic elements (Fe, Co, and Ni, mainly), chemists have devised methods to design surfaces and active sites as needed, through functionalization, conjugate formation, doping, or even core-shell structuring. There are many possibilities when it comes to surface engineering on the nano scale, many of which are still unexplored.

Figure 2 – Evolution of the number of papers published using the keywords "catalyst" "catalyst" + "nanoparticles", and "catalyst" + "magnetic nanoparticles", as well as the evolution of the number of citations for this last set of keywords.
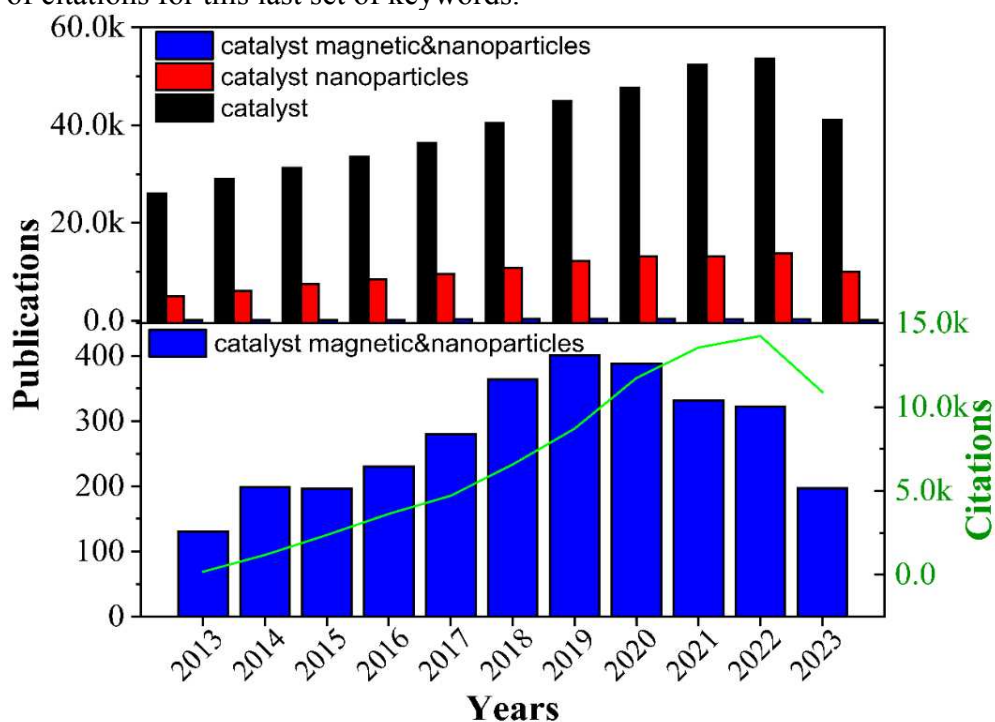
Source: the author (data gathered from the Web of Science on November 10, 2023).

In a search conducted in early November 2023 on the Web of Science, 710,296 articles, review articles, or procedure-related articles related to the term 'catalyst' were found, of which 435,922 (almost 2/3) were published in the last 10 years. In this recent interval, from 2013 onwards, this term appears related to 'nanoparticles' in 109,862 articles and to 'magnetic nanoparticles' in 3,039 works. As shown in Fig. 2, the field of catalysis is progressively expanding, but magnetic nanoparticles are still proportionally underexplored. It is believed that there are still many untested possibilities with magnetic nanoparticles.

This chapter aims to provide a comprehensive overview of the current state of research in the specific field of catalysis with magnetic nanoparticles. By delving into existing literature and recent advancements, both in theoretical frameworks and experimental

approaches, our goal is to contribute to the continuously evolving landscape of magnetic nanoparticle catalysis. We seek not only to summarize the existing body of knowledge but also to offer insights that may inspire and guide future investigations in this intriguing intersection of catalysis and nanotechnology.

1.2 Basic Principles of Magnetic Materials

Before delving into the various synthesis strategies and applications of magnetic materials in catalysis, it is crucial to understand the correlation of magnetism with the structure of materials, why magnetic materials are particularly significant for catalysis at the nanoscale, and which nanomaterials are most suitable for this purpose.

Magnetic materials are composed of atoms or ions that possess a non-neutral net magnetic moment resulting from the electronic orbital angular moment (translation) and spin moment (rotation). These moments are coupled for each atom, and the magnetic properties of a substance depend on whether these moments are completely or partially counterbalanced (NOQTA *et al.*, 2019). Typically, materials spontaneously exhibiting magnetic phenomena consist of elements such as Fe, Co, Ni, and/or certain rare-earth metals, including Gd (GILROY *et al.*, 2016; MAJIDI *et al.*, 2016).

The properties of a material are not solely defined by its magnetization; the variation of this quantity with the applied magnetic field is equally crucial. Based on a material's response to a magnetic field, it can be categorized as diamagnetic, paramagnetic, antiferromagnetic, ferrimagnetic, ferromagnetic, or superparamagnetic.

Diamagnetic materials lack magnetic dipoles in the absence of an external magnetic field, yet their spins align in the opposite direction to the applied magnetic field, resulting in repulsion (NOQTA *et al.*, 2019). Paramagnetic materials have weakly coupled, randomly disordered magnetic moments, aligning only under the influence of an external magnetic field (SOARES *et al.*, 2021).

Antiferromagnetic materials, akin to paramagnetic ones, possess magnetic moments but they are structured in identical interpenetrated sub-lattices. These moments spontaneously align both in the same and opposite directions to the external magnetic field, balanced by exchange interactions (SPALDIN, 2010). Ferrimagnetic materials resemble antiferromagnetic ones in structure but have different magnetic moments in their interpenetrated sub-lattices, only partially counterbalanced, resulting in a net magnetic moment (SOARES *et al.*, 2021). In contrast, ferromagnetic materials have spontaneously aligned

magnetic moments, all in a single direction. Table 1 provides a summary of the mains forms of magnetism and their features.

Table 1 – Summary of the primary forms of magnetism and their characteristics.

Magnetism	Examples	Atomic / Magnetic behavior		
Diamagnetism	Inert gases, many metals (Bi, Au, Cu) and non-metalic elements (Si, P, S), ions (Na^+, Cl^-) and molecules (N_2, H_2O)	$H=0$	Atoms have no magnetic moments.	Susceptibility (χ) is small and negative (-10^{-6} to -10^{-5})
Paramagnetism	Some metals (Al, Mg), diatomic molecules (O_2, NO)	$H=0$	Atoms have randomly oriented magnetic moments	χ: small and positive (10^{-5} to 10^{-3})
Ferromagnetism	Fe, Ni, Co, alloys of ferromagnetic elements	$H=0$	Atoms are organized into domains which have parallel aligned magnetic moments.	χ: large (>100) (below T_c)
Antiferromagnetism	Cr, MnO, CoO	$H=0$	Atoms are organized into domains which have antiparallel aligned magnetic moments.	χ: small and positive (10^{-5} to 10^{-3})
Ferrimagnetism	Fe_3O_4, mixed oxides of iron, Sr ferrite	$H=0$	Atoms are organized into domains which have unequal antiparallel aligned magnetic moments.	χ: large (>100) (below T_c)
Superparamagnetism	Nano-sized ferromagnetic (Fe, Co, Ni) and ferrimagnetic (Fe_3O_4, $ZnFe_2O_4$) materials (single domain)	$H=0$	The atoms are organized into domains, with moments either parallel or partially compensated antiparallel. In this arrangement, each domain behaves as a free particle.	χ: large (>100) (below T_c)
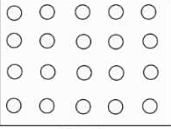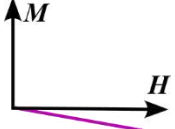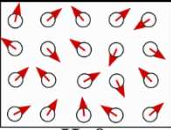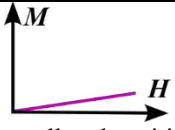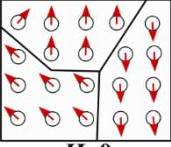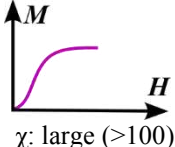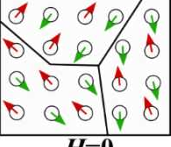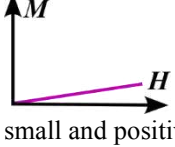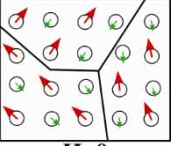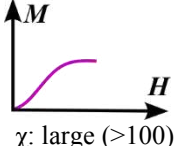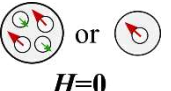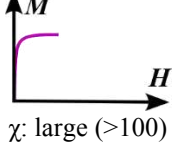
Source: adapted from reference (PALAGUMMI; YUAN, 2016).

The observed magnetic behavior in materials is influenced by factors such as temperature and the configuration of their magnetic domains. For instance, ferromagnetic materials may exhibit neutral magnetic momentum when their uniformly aligned moments are divided into smaller randomly distributed sections called domains. This concept, proposed by

Pierre Weiss in 1907, minimizes external magnetic field (magnetostatic energy) and reduce internal energy (SPALDIN, 2010). Depending on their orientation, individual moments of these domains may be either totally or partially counterbalanced.

Moreover, ferromagnetic, antiferromagnetic, and ferrimagnetic materials may undergo magnetic phase transition at elevated temperature, surpassing their spontaneous magnetization energy. Beyond a critical temperature (T_c), these materials exhibit paramagnetic behavior. The transition temperature for ferromagnetic and ferrimagnetic materials is referred to as the Curie temperature, while for antiferromagnetic materials, it is known as the Néel temperature (SPALDIN, 2010).

Another important aspect related to the properties of magnetic materials is their particle size. Larger particles consist of several domains, minimizing magnetostatic energy. As particle size decreases, the formation of domains becomes energetically unfavorable, because the energy required to create domain walls is no longer offset by the reduction in magnetostatic energy (GALVÃO, Wesley S. *et al.*, 2015). At this point, each particle is composed of a single domain, with magnetic moments aligned in the same directions, as dictated by its magneto-crystalline anisotropy.

Single-domain materials exhibit distinct magnetic properties. Notably, there is an increase in the magnetic field required in magnetization and demagnetization processes, often referred to as the coercive field. In contrast to multi-domains materials where the domain walls movement plays an important role, in single-domain materials, magnetization and demagnetization depend exclusively on the rotation of strongly coupled magnetic moments, demanding higher energy (GUBIN, 2009). As the size of single-domain particles decreases, there is an increase in the coercive field due to a higher ratio between the surface magnetic moments with greater anisotropy and the inner moments. However, as the particle size decreases further, thermal fluctuations becomes more pronounced and below a critical size, the particles' Brownian rotation is sufficient to overcome the coercive force (SOARES *et al.*, 2021). Consequently, each particle behaves as a paramagnetic moment, a phenomenon referred to as superparamagnetic state.

In the pursuit of the primary goal of utilizing magnetic catalysts, recoverability, it is crucial for the materials to respond promptly to the magnetic field (i.e., easy magnetization). Simultaneously, they should lose their magnetization entirely upon the removal of the field, thus avoiding aggregation due to interparticle attractions. Paramagnetic materials, such as Al, Pt, Mg, Ca, etc., prove unsuitable as they align with the field but lack sufficient magnetic susceptibility to be magnetically displaced within the reactor (GAETA *et al.*, 2021). In contrast,

superparamagnetic materials seem to fulfill all the necessary criteria. This category represents a unique facet of magnetism that exclusively emerges in ultra-small sized ferri- and ferromagnetic materials. Chemists are actively exploring methods to modulate material production to effectively harness this phenomenon.

1.3 Magnetism in nanoparticulated materials (Metals, Oxides and Alloys)

Due to their exceptional properties, primarily stemming from their high surface-to-volume ratio, nanoparticles have garnered significant interest in technological development. Among nanoparticles, magnetic ones gained prominence due to their ease of manipulation using a magnetic field. Furthermore, in the range of tens of nanometers, many ferri- and ferromagnetic materials exhibit superparamagnetism, which is of huge importance in catalysis.

The most notable magnetic materials are composed of at least one of the three ferromagnetic elements: Fe, Co, and Ni, either in their elemental nanoparticulate forms (Fe^0, Ni^0 and Co^0) or in oxides (Fe_2O_3), ferrites (MFe_2O_4; $M = Zn^{2+}$, Mn^{2+}, Cu^{2+}, Ni^{2+}, etc.) and alloys (such as FeCo, NiFe and FePt) (MAJIDI *et al.*, 2016). Ferromagnetic materials consist of elemental nanoparticles and alloys containing Fe, Ni, Co or some rare earths. On the other hand, ferrimagnetic materials are characterized by sub-lattices composed of these elements. However, in ferrimagnetic materials, the arrangement of these sub-lattices results in magnetic moments that are only partially offset from each other. A notable example of ferrimagnetism is observed in magnetite (Fe_3O_4), which exhibits an ordered spinel inverse structure, as depicted in Fig. 3. As observed, its unit cell comprises 32 O^{2-} anions arranged in a face-centered cubic pattern. Within this framework, there are 16 tetrahedral and 32 octahedral sites. Specifically, Fe^{2+} ions occupy half of the octahedral sites, while Fe^{3+} ions populate all tetrahedral sites and the remaining half of octahedral sites. This configuration results in incomplete spin compensation between Fe^{2+} and Fe^{3+}, classifying magnetite as a ferrimagnetic material.

Oxides represents the most prevalent magnetic nanomaterials owing to their ease of acquisition. Some relevant examples are the iron oxides, including magnetite, maghemite, and hematite, which are generally either weakly magnetic or susceptible to oxidation, resulting in a loss of susceptibility. However, it is noteworthy that 69 out of the top 100 most cited articles in the "magnetic nanoparticles in catalysis" field over the last 5 years utilized iron oxides, 64 of them specifically employing magnetite.

Figure 3 – Illustration of the unit cell of magnetite, with inverse spinel structure.
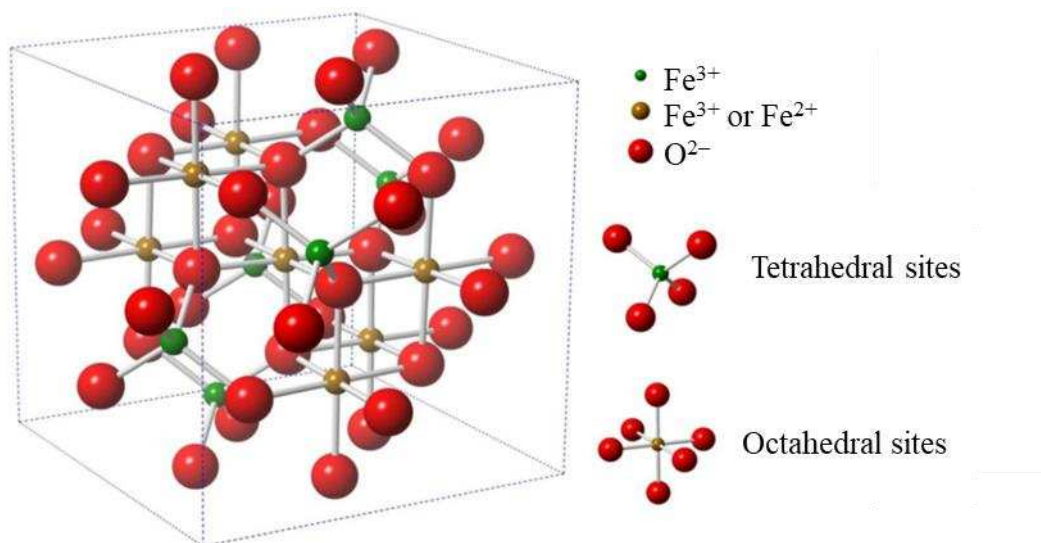
Source: (GALVÃO, Wesley S. *et al.*, 2015)

Conversely, the synthesis of ferrite nanoparticles is a more intricate process, often requiring high temperature and pressure, and is therefore less common (GALVÃO, W. S. *et al.*, 2014; GALVÃO, Wesley S. *et al.*, 2015). Nonetheless, these ferrite nanoparticles exhibit greater stability against oxidation compared to simple oxides, as the Fe^{2+} ions are replaced by less oxidizable divalent ions. Additionally, they generally manifest higher magnetism. For instance, $Zn_{0.4}Fe_{2.6}O_4$ nanoparticles were obtained with a saturation magnetization of 175 emu g^{-1} (JANG *et al.*, 2009).

Magnetic nano-alloys have gained prominence due to their high saturation magnetization, even surpassing that of single-element phases. Among alloys, FeCo nanoparticles have exhibited the highest saturation magnetization, approximately 230 emu g^{-1}, close to the bulk value of 245 emu g^{-1} (ABBAS *et al.*, 2013; WANG, Chao *et al.*, 2009). In contrast, the individual elements Fe, Co, and Ni have 218, 161, and 54 emu g^{-1}, respectively (HOU, Yanglong; SELLMYER, 2017). However, the synthesis of elemental nanoparticles and nanoalloys is far more complex, necessitating a controlled atmosphere and high temperature. Despite the intricacies in their synthesis and their greater susceptibility to oxidation, new techniques for obtaining nano-alloys are continually emerging (GILROY *et al.*, 2016).

1.4 Synthesis of Magnetic Nanoparticles

In the literature, various methods are available for synthesizing magnetic nanoparticles, each with its own set of advantages and disadvantages. The choice of the synthesis method is a critical factor that influences the morphology, average size, and size distribution of nanoparticles, thus affecting catalysis processes (DUAN *et al.*, 2018; MAJIDI *et al.*, 2016). Generally, magnetic nanoparticles are obtained through coprecipitation, solvothermal synthesis, sonochemistry, sol-gel synthesis, microemulsion, microwave, green synthesis, arc discharge, pyrolysis, ball milling, thermal decomposition, chemical reduction, or the polyol method.

1.4.1 Coprecipitation

Coprecipitation is one of the most common and straightforward techniques in the synthesis of magnetic nanoparticles, especially in the formation of iron oxides such as magnetite. It involves the precipitation of Fe, Ni, or Co ions in the form of oxides by the addition of an alkaline substance. The most common case is the synthesis of magnetite, where an aqueous solution containing Fe^{2+} and Fe^{3+} ions in a molar ratio of 1:2 is mixed with a solution of NH_4OH, NaOH, hexamethylenetetramine, or another base, leading to the formation of insoluble hydroxides. These hydroxides undergo condensation reactions, as shown in equations 1-5, forming Fe_3O_4 (GALVÃO, Wesley S. *et al.*, 2015).

$$2\ Fe^{3+}_{(aq.)} + 6\ OH^-_{(aq.)} \rightarrow 2\ Fe(OH)_{3\ (s)} \tag{1}$$

$$2\ Fe(OH)_{3\ (s)} \rightarrow 2\ FeOOH_{(s)} + 2\ H_2O_{(l)} \tag{2}$$

$$Fe^{2+}_{(aq.)} + 2\ OH^-_{(aq.)} \rightarrow Fe(OH)_{2\ (s)} \tag{3}$$

$$2\ FeOOH_{(s)} + Fe(OH)_{2\ (s)} \rightarrow Fe_3O_{4\ (s)} + 2\ H_2O_{(l)} \tag{4}$$

$$2\ Fe^{3+}_{(aq.)} + Fe^{2+}_{(aq.)} + 6\ OH^-_{(aq.)} \rightarrow Fe_3O_{4\ (s)} + 4\ H_2O_{(l)} \tag{5}$$
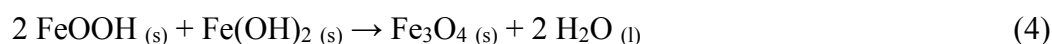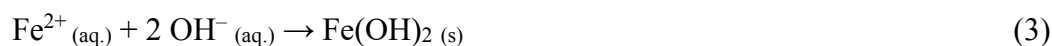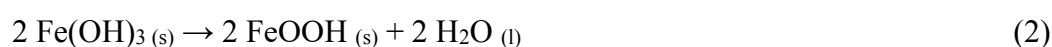
Some advantages of coprecipitation are its minimal equipment requirements, high reproducibility, and scalability. The size and morphology of nanoparticles can be controlled by factors such as the type and concentration of reagents, stirring speed, temperature, pH, reaction time, and the presence of stabilizers, among others (RIAL; FERREIRA, 2021). For example, Gribanov *et al.* showed that the use of strong bases like NaOH and KOH leads to the formation of non-magnetic species, which does not occur when a weak base such as ammonia is used

(GRIBANOV *et al.*, 1990). Yazdani and Seddigh, investigating different precursor salts in magnetite formation, observed that salts with larger anions resulted in smaller-sized particles (YAZDANI; SEDDIGH, 2016).

1.4.2 Sonochemistry

Sonochemistry is an assistive technique that relies on conducting synthesis reactions under radiation generated by a piezoelectric transducer capable of creating high-frequency mechanical waves, typically around 20 kHz (GALVÃO, Wesley S. *et al.*, 2015). As these waves propagate through the reaction medium, they generate disturbances, regions of high and low pressure, forming bubbles that grow and eventually collapse, creating localized conditions of up to 5000 K and pressures exceeding 1000 atm (NETO *et al.*, 2021). These conditions favor and accelerate certain reactions (NETO *et al.*, 2021). In addition to increasing the frequency of collisions between reactants, the agitation generated in the system also promotes rapid mixing of the reagents, reducing concentration gradients. This allows for better control of nucleation and particle growth (DODDS *et al.*, 2007; EVRARD *et al.*, 2020).

Some of the catalysts synthesized through sonochemistry include Fe_3O_4 (ALINEZHAD *et al.*, 2019), $CuFe_2O_4$ (RAJPUT *et al.*, 2015), $ZnFe_2O_4$ (MALEKI; VARZI; HASSANZADEH-AFRUZI, 2019), $BiFeO_3$ (SOLTANI; ENTEZARI, 2014), and $CoFe_2O_4$ (KARAOGLU; BAYKAL, 2014). Due to the microjets of liquid on the surface of the particles during the synthesis itself, the surface of these materials tends to be more active. For example, Rajput *et al.* obtained Cu ferrite with a larger surface area and catalytic activity compared to the conventional coprecipitation method (RAJPUT *et al.*, 2015).

1.4.3 Solvothermal or Hydrothermal

Although coprecipitation and sonochemistry offer pathways for synthesizing numerous catalysts, a critical concern is their tendency to yield products with diminished crystallinity, particularly evident in ferrites (GALVÃO, Wesley S. *et al.*, 2015). This results in weaker magnetic properties, posing challenges in catalyst recovery. To address this, chemists commonly conduct syntheses in Teflon-lined stainless-steel vessels under high pressure (between 1 and 100 MPa) and temperature (ranging from 100 and 1000 °C, typically surpassing the solvent's boiling point) (RIAL; FERREIRA, 2021). In hydrothermal processes, water serves

as the solvent, while solvothermal processes utilize organic solvents like ethylene glycol, diethylene glycol, glycerol, ethanol, among others (RIAL; FERREIRA, 2021).

Despite drawbacks, such as the need for prolonged harsh synthesis conditions and limitations on flow (multiple steps) synthesis and surface engineering processes, reactions in sealed reactors offer precise control over shape, size, and crystallinity (HARISH *et al.*, 2023). This control is achieved through factors like synthesis time, temperature, and the composition of precursors and solvents (RIAL; FERREIRA, 2021). For example, Tanaka *et al.* achieved gamma-Fe_2O_3 with a 2D nanoflakes morphology, possessing high surface area and catalytic activity, following a solvothermal treatment at 180°C for 16 hours, using a solution of ferric nitrate in a mixture of isopropanol/glycerol (TANAKA *et al.*, 2019).

1.4.3.1 Polyol

The polyol method is a promising strategy for producing magnetic nanoparticles, particularly metallic and alloy nanoparticles. It was proposed by Fievet, Lagier and Figlarz in 1989 to synthesize metal powders, such as Co, Ni, and Cu particles, from their respective salts (FIEVET; LAGIER; FIGLARZ, 1989). This methodology is based on the suspension of metal salts precursors in a polyalcohol (such as ethylene glycol and propylene glycol) for their reduction to zero-valent state, usually at the boiling temperature of the solvent. Therefore, the polyalcohol serves two roles, acting as a solvent and a reducing agent (FIEVET *et al.*, 2018). This methodology has excelled in providing particles with uniform sizes and shapes, and it uses low-toxic and renewable solvents (DONG; CHEN; FELDMANN, 2015).

Due to the low reduction potential for Ni, Fe, and Co, at the limit of reductive capacity of polyols, it is imperative to use strong and concentrated bases in magnetic nanoparticles synthesis. The OH^- concentration, as well the metal precursors' concentration, is extremely important in the kinetics of reaction because it is related to the intermediate complex formation with metal ions. The metal ions chelation by the alkoxide formed in strongly alkaline medium has been reported as the determining step in the process. For instance, ethylene glycol, the most used solvent in the syntheses of metallic nanoparticles by polyol method, dehydrates to acetaldehyde followed by the formation of diacetyl, as shown in the following reaction (Fig. 4):

Figure 4 – Mechanism of metal reduction using the polyol method.
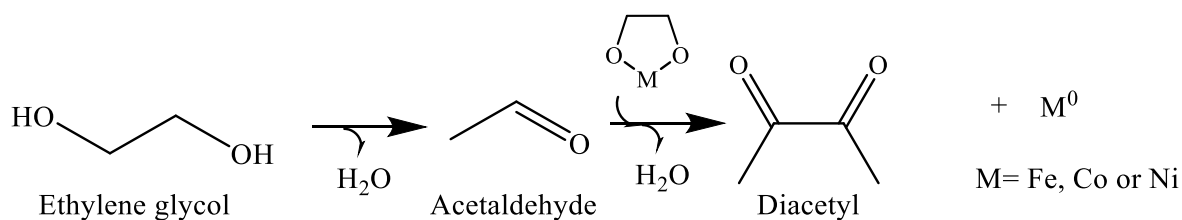
Source: the author.

In addition to the metal precursors and hydroxide concentrations, the kinetics of reaction in polyol synthesis is determined by other factors, such as the temperature and the redox potential of the polyol. Therefore, all these parameters can be used to adjust morphology and size of the produced nanoparticles. Zamanpour *et al.* (2012) studied some of these parameters and observed an increase in particle size and saturation magnetization when the [OH⁻] / [metal precursor] ratio is amplified. However, higher ratio than 27 lead to the formation of secondary phases, such as oxides and hydroxides (ZAMANPOUR *et al.*, 2012). The polyol used in the synthesis is another interferent in the nanoparticle's morphology. Carroll *et al.* (2011) obtained copper nanoparticles with different profiles, such as spheres, pentagons, triangles, hexagons, and rods, just changing the polyol from ethylene glycol to tetraethylene glycol (CARROLL *et al.*, 2011). Furthermore, the higher the redox potential of a polyol, the higher the nucleation rate and smaller particles are formed (JOSEYPHUS, R.J. *et al.*, 2007).

There are two common approaches in the polyol method: (1) solubilizing the metal precursors before heating and (2) adding precursors under boiling temperature. The second approach, generally, leads to the formation of larger particles, but with fascinating morphologies. For example, Karipoth *et al.* (2016) realized the instant and simultaneous reduction of iron and cobalt salts in ethylene glycol at 180 °C and obtained flower-like FeCo crystals with an average particle size of 138 nm (KARIPOTH *et al.*, 2016). However, following the first approach, Zamanpour *et al.* (2012) obtained FeCo particles with diameter around 30 nm. In addition, by adjusting parameters such as time and OH⁻ concentration, the authors were able to tailor their magnetic properties and they obtained a M_s value up to 221 emu/g (ZAMANPOUR *et al.*, 2012).

The polyol technique is still challenging, mainly because it is hard to obtain ultra-small nanometric particles and due to the reducing power of polyols be restricted. According to the literature, the iron reduction occurs through disproportionation, which has a maximum yield value of only 20%, thermodynamically predicted (FIEVET *et al.*, 2018; VIAU; FIÉVET-

VINCENT; FIÉVET, 1996). However, some strategies have been developed, extending the application of the polyol method, co-reducing Fe/Ni/Co with more easily reduced metals, such as Pt, and using seeded growth with small amounts of Cu^{2+}, Ag^+, Pt^{4+}, Pd^{2+} ions (FIEVET *et al.*, 2018; FIEVET; LAGIER; FIGLARZ, 1989; JOSEYPHUS, R. Justin *et al.*, 2010; PONRAJ *et al.*, 2020).

1.4.4 Ball milling

Ball milling is a top-down physical technique for preparing nano-alloys, in which macro-sized materials are ground into finely divided powders by collision between tiny rigid balls in a sealed container. In this method, the precursor can be either the constituent elements or the macro-sized alloy (ALBAAJI *et al.*, 2017; ÇELIK; FIRAT, 2018). Due to processing in high-energy mills, the powder particles are repeatedly melted, fractured, and re-melted until the diffusion of one phase into another or the desired size reduction is achieved (ALBAAJI *et al.*, 2017). The main advantage of this technique is large-scale production. For instance, Albaaji utilized 20 g of FeCo powder and after 6 hours of milling, obtained particles with an average crystallite size of 22.48 nm (ALBAAJI *et al.*, 2017). Starting with Fe and Co powder, Çelik obtained particles with an average size of 11.5 nm after 45 hours of grinding, (ÇELIK; FIRAT, 2018). Bez used grinding for 5 hours under an argon atmosphere and an additional annealing step at 873 K to obtain FeCo particles with an average crystallite size of 25 nm from Fe and Co powders (BEZ *et al.*, 2015).

However, ball milling also has disadvantages, as it is a time-consuming process that depends on the desired grain size and phase. Furthermore, it is challenging to control the morphology and size, and the synthesized nanoparticles are often agglomerate (ÇELIK; FIRAT, 2018). Additionally, obtaining easily oxidized magnetic alloys, such as FeCo, is highly challenging as it requires a controlled atmosphere and the addition of surfactants (BEZ *et al.*, 2015; ÇELIK; FIRAT, 2018).

1.4.5 Thermal decomposition

The synthesis of nano-alloys by thermal decomposition is based on the simultaneous decomposition of metal precursors (usually organic complexes, such as acetylacetonates, oleates, pentacarbonyls, acetates, etc.) in high-boiling temperature organic solvents (oleylamine, oleic acid, octadecene, paraffin, etc.). This technique has been attractive

for controlling the morphology, crystallinity, and average size of magnetic nanoparticles (SOARES *et al.*, 2021). Thermal decomposition allows for the easy separation of nucleation and grain growth steps, resulting in particles with uniform shapes and narrow size distributions (ZAMANI KOUHPANJI; STADLER, 2020).

Thermal decomposition has been the preferred approach for reducing hard-to-reduce metals such as Fe, Co, and Ni. Chaubey *et al.* (2007) used acetylacetonates, $Fe(acac)_3$ and $Co(acac)_2$, in a mixture of 1,2-hexanediol with oleic acid, oleylamine and trioctylphosphine to obtain FeCo nanoparticles with highly-controlled sizes of 20 and 10 nm, depending on the surfactant used (CHAUBEY *et al.*, 2007). Tzitzios *et al.* (2011) conducted the thermal decomposition of $Fe(CO)_5$ and $Co_2(CO)_8$ in paraffin oil, using oleic acid and oleylamine as surfactants, and synthesized FeCo particles with an average size of 8 nm (TZITZIOS *et al.*, 2011).

The thermal decomposition strategy has been very promising, particularly when surfactants are used to control the size and shape of nanoparticles. Nonetheless, it has some drawbacks, such as the requirement for high temperatures, the use of costly precursors and toxic, non-renewable solvents, and limitations for large-scale production in the laboratory (SOARES *et al.*, 2021). Furthermore, nano-alloys formed by thermal decomposition tend to be easily oxidized, especially in aqueous media (ZAMANI KOUHPANJI; STADLER, 2020).

1.4.6 Chemical reduction

Chemical reduction is a synthesis technique focused on the reduction of metal ions in a simple manner, without the need for high pressure and temperature, or sophisticated equipment. To achieve the reduction, strong reducing agents, such as N_2H_4, $NaBH_4$, Al/AlF_6^{3-}, and H_2 gas, are used (FERRANDO; JELLINEK; JOHNSTON, 2008; VADILLO *et al.*, 2021). For example, Vadillo *et al.* (2021) utilized Al and AlF_6^{3-} to obtain FeCo nanoparticles from iron (II) chloride and cobalt (II) acetate. After stirring for 60 min at 80 °C, particles with an average crystalline size of 42 nm were obtained, albeit with an agglomerated structure of 200-500 nm (VADILLO *et al.*, 2021). Yang *et al.* (2018) started with Co (II) and Fe (II) chlorides and, upon reduction with $NaBH_4$ for 50 minutes, obtained amorphous FeCo alloys with average particles sizes ranging from 16 to 25 nm (YANG, Bai *et al.*, 2018).

However, chemical reduction in the synthesis of nano-alloys has disadvantages, as the resulting product is typically poorly crystalline, and therefore poorly magnetic, necessitating

further heat treatment to enhance its properties, which can lead to grain growth. Additionally, reducing agents often generate intractable impurities in combination with the reaction product.

1.5 Main applications in catalysis

The potential applications of magnetic nanoparticles in catalysis are exceedingly diverse. This versatility arises not only from the numerous feasible combinations of Fe, Co, or Ni with other elements to induce magnetization but also the extensive array of possibilities for surface modifications. Some developed catalysts leverage the inherent surface composition of magnetic nanoparticles. Although somewhat constrained, this approach presents advantages, including a more straightforward and streamlined (with few steps) synthesis. Conversely, catalysts in which the magnetic core serves solely as a support afford greater flexibility for customization. In instances where the core does not interact with the reaction medium, these catalysts offer enhanced stability.

1.5.1 Fenton-type, photo-Fenton, and sulphate radical-based processes

Due to its simplicity, it is common for the magnetic material itself to function as the catalyst. Consequently, reactions catalyzed by Fe, Ni, and Co elements undergo more extensive exploration. One of the most investigated catalytic processes involves the degradation of hydrogen peroxide (H_2O_2). Initially examined by Fenton using Fe^{2+} ions as a catalyst in the degradation of tartaric acid, this process has found widespread application in the degradation of pollutants through radicals •OH generated in this pathway (AHMAD *et al.*, 2023; FENTON, 1894). The utilization of magnetic nanoparticles in this context offers advantages, including (i) avoiding precipitation issues of Fe^{2+} ions at pH levels above 3, common in homogeneous catalysis, and (ii) preventing effluent contamination associated with high doses of Fe^{2+} required, thanks to magnetic recoverability (DO NASCIMENTO *et al.*, 2021).

For example, Soufi *et al.* employed $CuFe_2O_4$ nanoparticles for the degradation of tartrazine with H_2O_2, achieving a degradation efficiency of over 90% for five consecutive cycles of use (SOUFI *et al.*, 2022). Optimization using the Box-Behnken design yielded a degradation efficiency of 97.9% with a catalyst dosage of 0.32 g/L, tartrazine concentration of 30.63 mg/L, H_2O_2 concentration of 64.35 mM, and a temperature of 49.92 °C. In another study, Sharma and Singhal evaluated different ferrites (MFe_2O_4, M = Cu, Zn, Ni, and Co) in the degradation of Remazol Black 5, finding that $CuFe_2O_4$ exhibited the best performance (k = 0.228 min^{-1}),

attributed to the coupling between the two redox cycles Fe^{2+}/Fe^{3+} and Cu^{+}/Cu^{2+} (SHARMA; SINGHAL, 2015).

In some instances, the magnetic core retains its role as the catalyst, while surface modifications enhance performance. Qu *et al.* improved the catalytic efficiency of $NiFe_2O_4$ catalysts sized between 40-80 nm by coating them with SiO_2. In this scenario, the porous shell acted as a spacer, preventing agglomeration due to residual magnetization while facilitating H_2O_2 activation (QU *et al.*, 2019). Ahmad *et al.* achieved enhanced catalysis against ofloxacin by impregnating Fe_3O_4-montmorillonite in calcium alginate to prevent iron leaching, maintaining catalytic efficiency over five cycles. Other modifications include carbon coating (BABAEI *et al.*, 2017), amino-modified carbon (QIN *et al.*, 2020), pullulan (CHENG *et al.*, 2021), PEG (NEAMTU *et al.*, 2018), beta-cyclodextrin/g-C_3N_4 (WANG, Hui *et al.*, 2022), MOF-5 (YANG, Ruixia *et al.*, 2021), and carbon nanotubes (CHEN, Yong *et al.*, 2020). A noteworthy case is reported by Chen *et al.*, wherein H_2O_2 from the Fenton process is produced by nanotubes containing Al^0, while nanotubes containing Fe^0 and Cu^0 nanoparticles convert it into OH radicals for sulfamerazine degradation (CHEN, Yong *et al.*, 2020).

Magnetic nanoparticles are also utilized in variants of the Fenton process, such as electro-Fenton, where H_2O_2 is formed on electrodes modified with materials like $SrFe_{12}O_{19}$ (HASSAN *et al.*, 2020) or Fe_3O_4 (ES'HAGHZADE *et al.*, 2017), which simultaneously convert it to OH. Additionally, nanomaterials like $BiFeO_4$ (SOLTANI; ENTEZARI, 2014) and $ZnFe_2O_4$ (BORTHAKUR; SAIKIA, 2019) can have their catalytic properties enhanced when subjected to UV-visible radiation and can be applied in hybrid processes known as photo-Fenton.

Other highly pertinent processes catalyzed by Fe, Ni, or Co ions are those based on sulphate radicals, comprising the list of advanced oxidative processes (AOPs).

AOPs are based on the utilization of highly oxidant radicals, such as $^\bullet OH$, $O_2^{\bullet -}$, and $SO_4^{\bullet -}$, to eliminate recalcitrant pollutants from the environment. The sulfate radical-based AOPs provide a higher reduction potential ($E_0 = 2.5\text{-}3.1$ eV) and therefore are more attractive than conventional methods based on Fenton reactions, which use Fe^{2+} ions and H_2O_2 in acidic medium to generate $^\bullet OH$ radicals (HOU, Jifei *et al.*, 2021). Besides, $SO_4^{\bullet -}$, due to the lack of hydrogen, has higher selectivity and efficiency than $^\bullet OH$ when degrading pollutants containing unsaturated bonds or aromatic π groups through electron transfer (ZHAO, Guoqing *et al.*, 2020).

The sulfate radicals in AOPs are produced from two main reagents, peroxymonosulfate and persulfate or peroxydisulfate, whose structures are shown in Fig. 5.

Figure 5 – Molecular structure of peroxymonosulfate (PMS) and persulfate (PS) ions.

Peroxymonosulfate (PMS)   Persulfate (PS)
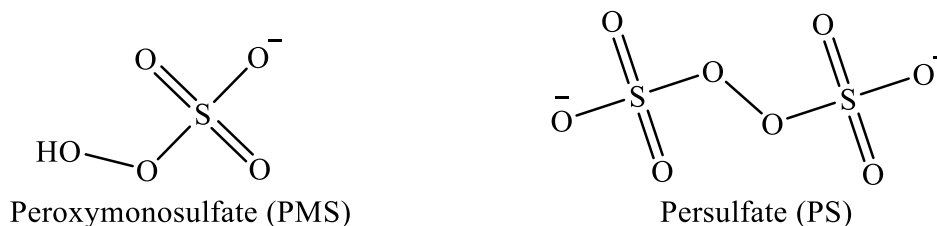
Source: the author.

The formation of radical species from these substances occurs through O–O bond cleavages, either by electron supply from metal ions or by homolytic cleavage resulting from radiation. Besides sulfate radicals, hydroxyl radicals are also formed in aqueous media and they are also powerful oxidants (E_0 ($^\bullet$OH /H_2O) = 2.81 V) (ZHAO, Guoqing $et\ al.$, 2020). However, they are formed immediately when peroxymonosulfate (HSO_5^-) is used, because it results from the O–O bond cleavage, while systems using persulfate ($S_2O_8^{2-}$) depend on side reactions between sulfate radicals and water or hydroxyl ions (WANG, Jianlong; WANG, 2020; ZHAO, Guoqing $et\ al.$, 2020). The activating reactions for PMS and PS are shown in equations from 6 to 12.

$$S_2O_8^{2-} + e^- \rightarrow 2\ SO_4^{\bullet -} \tag{6}$$

$$S_2O_8^{2-} + h\nu \rightarrow 2\ SO_4^{\bullet -} \tag{7}$$

$$SO_4^{\bullet -} + H_2O \rightarrow\ ^\bullet OH + SO_4^{2-} + H^+ \text{ (acidic medium)} \tag{8}$$

$$SO_4^{\bullet -} + OH^- \rightarrow\ ^\bullet OH + SO_4^{2-} \text{ (alkaline medium)} \tag{9}$$

$$HSO_5^- + e^- \rightarrow SO_4^{\bullet -} + OH^- \tag{10}$$

$$HSO_5^- + e^- \rightarrow SO_4^{2-} +\ ^\bullet OH \tag{11}$$

$$HSO_5^- + h\nu \rightarrow SO_4^{\bullet -} +\ ^\bullet OH \tag{12}$$
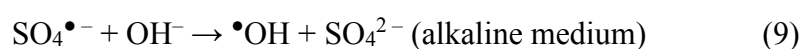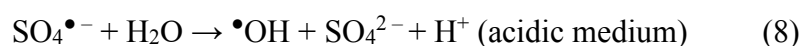
Among the sulphate radical-forming species, PMS has been the most attractive due to its higher reactivity, which comes from its asymmetric structure and longer O–O bond (KOHANTORABI; MOUSSAVI; GIANNAKIS, 2021). Therefore, PMS is more easily activated, and it is moreover able to degrade pollutants by multiple mechanisms, with $SO_4^{\bullet -}$ and $^\bullet$OH.

Nevertheless, PMS activity in AOPs is dependent on some factors, such as pH, oxidant dosage, interferent anions, and temperature. The pKa1 and pKa2 of PMS are 0 and 9.4, respectively, which means that HSO_5^- is the predominant specie at pH values below 9.4, while

SO_5^{2-} is the main form at alkaline pH, with low potential reduction (1.1 V) (WANG, Jianlong; WANG, 2020; ZHANG, Yang *et al.*, 2020)(WANG, Jianlong; WANG, 2020; ZHANG, Yang *et al.*, 2020). Furthermore, it has been shown that the formation of $^{\bullet}OH$ is favored at high OH^- concentrations (alkaline medium), but it has lower reduction potential (1.8 V) than in acidic solutions (2.7 V) (XIAO *et al.*, 2020). Therefore, due to the weaker oxidation power of $^{\bullet}OH$ and its shorter life span, the performance of PMS may reduce under these conditions. Besides, at extremely high pH (pH > 11), PMS can undergo a so-called alkaline activation, forming singlet oxygen and superoxide anion radicals (XIA *et al.*, 2020).

The oxidant and catalyst dosages are also an important issue in sulphate based AOPs. Upon increasing their concentration, degradation should be increased, however high radical loadings enhance the scavenging effect by radical recombination and formation of $SO_5^{\bullet-}$ radical with weaker reactivity (E° = 1.1 V) (GHANBARI; MORADI, 2017).

The removal efficacy is also influenced by coexisting anions. Anionic species such as Cl^-, HCO_3^-, CO_3^{2-}, NO_3^-, $H_2PO_4^-$, HPO_4^{2-} and PO_4^{3-} are very often found in industrial wastewaters and natural water bodies, and can react with $SO_4^{\bullet-}$, forming less reactive radicals, as shown in equations 13-19 (ZHAO, Guoqing *et al.*, 2020).

$$Cl^- + SO_4^{\bullet-} \rightarrow Cl^{\bullet} + SO_4^{2-} \tag{13}$$
$$HCO_3^- + SO_4^{\bullet-} \rightarrow HCO_3^{\bullet} + SO_4^{2-} \tag{14}$$
$$CO_3^{2-} + SO_4^{\bullet-} \rightarrow CO_3^{\bullet-} + SO_4^{2-} \tag{15}$$
$$NO_3^- + SO_4^{\bullet-} \rightarrow NO_3^{\bullet} + SO_4^{2-} \tag{16}$$
$$H_2PO_4^- + SO_4^{\bullet-} \rightarrow H_2PO_4^{\bullet} + SO_4^{2-} \tag{17}$$
$$HPO_4^{2-} + SO_4^{\bullet-} \rightarrow HPO_4^{\bullet-} + SO_4^{2-} \tag{18}$$
$$PO_4^{3-} + SO_4^{\bullet-} \rightarrow PO_4^{\bullet 2-} + SO_4^{2-} \tag{19}$$

Temperature is another relevant factor in AOPs in general. High temperatures usually enhance the reaction rate because the reactant molecules collide more strongly, and the energy barrier of oxidation reactions is more easily overcome.

1.5.2 Reduction reactions

Another facet of magnetic nanoparticles' application in catalysis lies in reduction reactions involving substances like $NaBH_4$ (more commonly employed) and formic acid or H_2 flow. Elements such as Fe, Ni, or Co, as well as other materials strategically anchored on the

surface, play a pivotal role in this process. For instance, Das *et al.* synthesized iron oxide *in situ* on polydopamine-modified montmorillonite and applied it in the reduction of 4-nitrophenol within 12 minutes and Congo red within 16 minutes, with rate constants of 5.3×10^{-3} and 3.01×10^{-3}, respectively, showcasing remarkable recyclability (utilized six times without a loss of activity) (DAS *et al.*, 2019). According to the proposed mechanism, BH_4^- ions from $NaBH_4$ adsorb on the nanoparticle surface, swiftly forming hydrides that can subsequently be utilized in reduction reactions. Other monometallic and bimetallic nanoparticles (in the zero-valence state) can also participate in this type of reaction. Ali *et al.* prepared Co^0, Co^0+Cu^0, and Co^0+Ag^0 impregnated in chitosan-carbon black fibers and effectively utilized them in the reduction of p-nitrophenol, Congo red, and Methyl Orange with $NaBH_4$ (ALI *et al.*, 2017). Trimetallic nanoparticles with a Ni core and Cu and Pd coatings, featuring a blackberry morphology and high surface area, were employed in the reduction of pollutants like methylene blue ($k = 3.19$ min^{-1}), rhodamine B ($k = 7.20$ min^{-1}), and 4-nitrophenol ($k = 1.10$ min^{-1}) (GONG, Zhengjie; MA; LIANG, 2021). The catalyst demonstrated resilience, retaining activity over five cycles without significant loss. These studies involving metallic nanoparticles demonstrated synergistic effects of Ni and Co with noble metals, facilitating electron transfer in catalysis by reducing the binding energy (ALI *et al.*, 2017; GONG, Zhengjie; MA; LIANG, 2021).

In pursuing an alternative reduction mechanism involving H_2 flow, Fe_3O_4 nanoparticles were synthesized through thermal decomposition using polyphenylenepyridyl dendrons as a coating, and palladium acetate was employed to create catalytic sites for the selective hydrogenation of dimethylethynylcarbinol (DMEC) to dimethylvinylcarbinol (DMVC, an intermediate for fragrances and vitamins E and K) (KUCHKINA *et al.*, 2013). The palladium, reduced on the surface, facilitated an increase in activity and selectivity of 98.2%, surpassing that of the Lindlar catalyst (2%-Pd/CaCO₃). In another investigation, where Ru/RuO_2 was utilized to modify the surface of Fe_3O_4 for its application in the reduction of nitrophenol to aniline, it was revealed that synergistic effects between these two types of materials enhanced electron transfer to the Ru surface, markedly elevating the yield (99%) and demonstrating a reaction rate of 2.2 s^{-1} (EASTERDAY *et al.*, 2015).

Halilu et al. synthesized Fe_3O_4 nanoparticles coated with SiO_2 and doped with Ni through a continuous process that involved coprecipitation of Fe^{2+}/Fe^{3+} ions, hydrolysis of tetraethylorthosilicate (TEOS), and Ni^{2+} doping by precipitation (HALILU *et al.*, 2016). The strategically positioned Ni in the octahedral sites of magnetite played a crucial role in dissociating H_2 molecules into hydride and proton, resulting in a notably high selectivity for furfuryl alcohol, attributed to its exclusive interaction with carbonyl groups.

Another important and environmentally relevant application of magnetic nanoparticles involves the reduction of Cr(IV) to Cr(III) using formic acid. Chen *et al.* synthesized Fe_3O_4 through the pyrolysis of the Fe^{3+}-polydopamine complex and coated it with Ag for the catalytic reduction of the pollutant Cr(IV), demonstrating catalyst's efficacy for up to four cycles (CHEN, Changlun *et al.*, 2018). In the proposed mechanism, Ag play a pivotal role by breaking down the formic acid molecule and forming the Ag-carbonyl complex, which subsequently reacts with Cr(IV) to yield Cr(III) and CO_2.

1.5.3 Organic Synthesis Reactions

Magnetic nanoparticles have been systematically tailored for their application as recoverable catalysts in organic synthesis. Among these, the Suzuki-Miyaura reaction, a pivotal process involving the formation of C-C bonds through the coupling of nucleophiles and aryl halides, stands out. Traditionally, this reaction relies on Pd-phenylphosphine complexes as catalysts, but ongoing efforts are exploring alternative catalysts that are more economical and less toxic. One approach involves retaining palladium while substituting the ligands. For instance, utilizing Fe_3O_4 as a magnetic support, researchers immobilized Pd on the surface after functionalization with triethylammonium chloride ionic liquid (VEISI; PIRHAYATI; KAKANEJADIFARD, 2017), o-phenylenediamine (MALEKI *et al.*, 2020), and biguanidine-chitosan (VEISI; NAJAFI; HEMMATI, 2018).

Moradi and Hajjami showcased the feasibility of replacing Pd with other metals. They stabilized the Ru-dithizone complex on Ni-biochar nanoparticles for catalysing cross-coupling reactions between aryl halides and phenylboronic acid (MORADI; HAJJAMI, 2022). The catalyst demonstrated heightened selectivity towards bromine in chloro and bromo-substituted aryl halides, along with enhanced yields in reactions involving iodobenzene. Notably, in reactions with 4-bromotoluene, the catalyst exhibited an impressive efficiency of 95% and proved recoverable for seven consecutive cycles. Employing the same magnetic support, the authors stabilized the Cu-ninhydrin complex on Ni-graphene oxide nanoparticles, achieving a remarkable 97% efficiency in the reaction with 4-bromotoluene (MORADI; HAJJAMI, 2021). This alternative catalyst also effectively facilitated coupling in C-O bonds, offering the potential for reuse up to eight times in the reaction of iodobenzene with phenol.

Ghorbani-Choghamarani, Mohammadi, and Taherinia synthesized $(ZrO)_2Fe_2O_5$ through coprecipitation for its application in C-C cross-coupling reactions between phenylboronic acid and iodobenzene, achieving a yield of 83%. The catalyst proved to be

reusable at least four times without a significant loss of activity (GHORBANI-CHOGHAMARANI; MOHAMMADI; TAHERINIA, 2019).

Inaloo and colleagues showcased the catalytic prowess of Ni^0 in Suzuki-Miyaura reactions, utilizing aryl sulfates and carbamates as alternatives to aryl halides (DINDARLOO INALOO et al., 2020a, b). In the reaction involving phenyl carbamate and phenylboronic acid, the catalyst featuring the Ni^{2+}-EDTA complex exhibited impressive recyclability, with efficiency exceeding 80% for up to 6 cycles. This was achieved using ethylene glycol as a solvent and monosodium ethylene glycolate as a base (DINDARLOO INALOO et al., 2020b). Through pre-reduction of Ni^{2+} ions to form Ni^0 nanoparticles on the catalyst's surface, the authors extended its applicability to Heck reactions, where double coupling occurs between alkenes and aryl halides (DINDARLOO INALOO et al., 2020a). Notably, KOH served as the base in the reaction of aryl carbamates and sulfamates with styrene, yielding impressive results of 92% and 88%, respectively.

Magnetic nanoparticles have proven to be versatile in catalyzing Sonogashira reactions, facilitating the formation of C-C bonds from aryl halides and terminal alkynes. In an innovative approach, Kargar and Luque utilized cellulose nanofiber-surface-modified Fe_3O_4 with Cu as a catalyst for the reaction between aryl halides and various alkynes, employing KOH as a base (GHAMARI KARGAR; LEN; LUQUE, 2022). Remarkably, they achieved a 97% yield in a 15-minute reaction at 40°C, aided by sonication of iodobenzene with phenylacetylene. The versatility of this catalyst was further demonstrated in the Ullmann reaction (between aryl halides and phenols), showcasing high selectivity (>99%) in the coupling of 1-iodo-4-nitrobenzene with phenol, and maintaining efficiency within the range of 95% to 90% over six reuse cycles.

Furthermore, magnetic nanoparticles play a pivotal role in catalyzing the Knoevenagel condensation, a reaction involving aldehydes or ketones with compounds containing active hydrogen to yield α-β-unsaturated compounds. For instance, Fatemeh et al. synthesized Fe_3O_4 and immobilized a Cu-proline complex to catalyze reactions of benzaldehydes with malononitrile using water as a solvent at room temperature (KALANTARI et al., 2022). Impressively, the catalyst displayed recyclability over eight cycles without a significant loss of catalytic activity. The versatility of this complex extended to three-component reactions of malononitrile, dimedone, and aldehydes in ethanol for the synthesis of pyran derivatives (KALANTARI et al., 2021). The catalyst exhibited consistent efficiency over nine consecutive cycles, showcasing its robust recyclability. Additionally, Akbarzadeh and Koukabi demonstrated that nanomagnetite (Fe_3O_4), even without coating, can catalyze

Knoevenagel condensation under both microwave radiation and conventional heating (KALANTARI *et al.*, 2021). Utilizing aldehydes, malononitrile, and sodium azide, they achieved a solvent-free synthesis of 5-substituted-1H-tetrazoles. Significantly, Fe^{3+} played a crucial role as a Lewis acid, coordinating with the carbonyl groups of the aldehyde and attacking the cyano group of malononitrile, facilitating its deprotonation. Impressively, the catalyst demonstrated sustained efficiency over five cycles with only a slight loss in activity.

Intriguingly, Alirezvani, Dekamin, and Valiey reported a noteworthy case wherein they synthesized Fe_3O_4 on chitosan functionalized with melamine to complex Cu^{2+} ions. This composite was employed as a catalyst in a cascade reaction involving the oxidation of benzyl alcohols to benzyl aldehydes, followed by Knoevenagel condensation with malononitrile (ALIREZVANI; DEKAMIN; VALIEY, 2019).

Zhang et al utilized dopamine to modify graphene oxide and complex molybdenum on the surface of Fe_3O_4. They applied this modified catalyst in a one-pot, three-component reaction involving isatins, malononitrile, and anilinolactones under microwave radiation at 90°C (ZHANG, Mo *et al.*, 2017). The catalyst demonstrated a conversion yield of up to 96% and proved to be reusable for up to 8 cycles without a significant loss of efficiency.

Magnetic nanoparticles have also been employed as a support for immobilizing acidic groups to facilitate the conversion of carbohydrates into 5-hydroxymethylfurfural (5-HMF), a pivotal intermediate in the production of fine chemicals, liquid fuels, and pharmaceuticals (KARIMI; SHEKAARI; *et al.*, 2021). Karimi *et al.* prepared Fe_3O_4 nanoparticles coated with SiO_2 (KARIMI; SHEKAARI; *et al.*, 2021) and functionalized them with dendrimer post-modified with chlorosulfonic acid to produce 5-HMF from different sugars. Fructose and glucose exhibited the highest conversions (93% and 89%, respectively). Utilizing the same magnetic support, Karimi *et al.* demonstrated the generation of sulfonic groups through the oxidation of thiol groups on previously functionalized graphene oxide (KARIMI; SEIDI; *et al.*, 2021). With this catalyst, the conversion efficiency of fructose was slightly lower (87%), and significantly reduced with glucose (65%).

Ghavidel, Mirza, and Soleimani-Amiri utilized $Fe_3O_4@C$ nanoparticles to catalyze the synthesis of 4H-Chromenes in water via a one-pot three-component reaction (GHAVIDEL; MIRZA; SOLEIMANI-AMIRI, 2021). Starting with salicylaldehyde, 2-naphthol, and dimedone, using water as the solvent, the authors achieved a yield of up to 95%. They attributed the success of the catalysis to a synergistic combination of Lewis base sites (O^-) activating the active methylene compounds and Lewis acid sites (Fe^{3+}) activating salicylaldehyde.

Several other noteworthy examples include aldehyde amination with nitroarenes (Pd as active site) (NASROLLAHZADEH; SAJADI, 2016; WEI *et al.*, 2013); amination of aryl aldehydes and ketones in aqueous ammonia (Ni) (MANZOLI *et al.*, 2019); amination of aryl carbamates and sulfamates (Ni^{2+}) (MANZOLI *et al.*, 2019); cyanation reactions (Pd) (VEISI *et al.*, 2020; VEISI; HEMMATI; SAFARIMEHR, 2018); azide-alkyne cycloaddition (Ni) (MOHAMMADI; GHORBANI-CHOGHAMARANI, 2022); and the synthesis of triazoles (Cu^{2+}) (GHAMARI KARGAR; BAGHERZADE; ESHGHI, 2020; KHASHEI SIUKI; GHAMARI KARGAR; BAGHERZADE, 2022). While our intention is not to provide an exhaustive list of applications, these examples illustrate the versatility of magnetic nanoparticles in various organic reactions.

1.5.4 Transesterification Reactions and Biodiesel Production

Catalysts for transesterification reactions, crucial for biodiesel production, demand basicity among other physicochemical features, such as a high surface area. In a study by Xie, Han, and Wang, sodium silicate, anchored on the surface of Fe_3O_4 nanoparticles through crosslinking with epichlorohydrin, proved effective in the transesterification of soybean oil (XIE; HAN; WANG, 2018). They catalytic system achieved an impressive yield of 99.2% with a 3% catalyst dosage, demonstrating a remarkable potential for up to five reuses while retaining at least 85% of its initial activity. Another surface modification strategy, employing $CaSO_4$, exhibited an efficiency of 94% in biodiesel production with *Jatropha curcas* oil, with a 12% catalyst dosage, and demonstrated reusability for up to nine cycles (TEO *et al.*, 2019).

A more straightforward and environmentally friendly approach was presented by Changmai *et al.*, who employed an extract derived from *Citrus sinensis* peels ashes for the one-step synthesis and functionalization of Fe_3O_4 (CHANGMAI *et al.*, 2021). This material found application in transesterification reactions for biodiesel production from cooking oil. The presence of highly alkaline oxides of K, Ca, and Mg from the ashes, incorporated into the catalyst's surface, played a pivotal role in deprotonating methanol. This process directed methanol to attack the electron-deficient carbonyl of triglycerides on the nanoparticles surface. The catalytic system achieved an impressive 98% yield with a 6% catalyst dosage, showcasing its usability for up to 9 reaction cycles.

Dantas *et al.* synthesized $Ni_{0.5}Zn_{0.5}Fe_2O_4$ through the combustion of the salts of the respective metals with urea (DANTAS *et al.*, 2020). The resulting material was applied without any modification in transesterification and esterification reactions for biodiesel production.

Remarkably, it exhibited high efficiency in esterification reactions with methanol, reaching an impressive 99.54% conversion rate, and demonstrate the potential for reuse for up to three cycles.

1.5.5 Enzyme immobilization

A distinctive form of homogeneous catalysis is enzymatic catalysis, known for its exceptional catalytic efficiency and superior chemo-, regio-, and stereoselectivities in comparison to other catalyst types. Furthermore, enzymatic pathways offer shorter synthetic routes under mild conditions and pose minimal environmental risks due to reduced toxic effluents (LANDARANI-ISFAHANI *et al.*, 2015; PEIMAN; BAHARFAR; MALEKI, 2021). However, like other homogeneous catalysts, enzymes present challenges in terms of recovery. The cost-intensive extraction processes often make their utilization impractical without being anchored on supports, in the form of aggregates, or encapsulated. Additionally, enzymes, being proteins, tend to exhibit lower stability in the presence of organic solvents, variations in pH, and temperature fluctuations, necessitating immobilization as a strategy to address these concerns. Magnetic nanoparticles emerge as particularly well-suited for convenient recovery, as even though ferromagnetic metal ions constitute the active sites of enzymes (such as Fe in catalase), free enzymes are not magnetically recoverable.

The predominant magnetic support for enzyme immobilization is magnetite, chosen for its ease of acquisition, minimal environmental impact, and remarkable magnetic susceptibility. Fe_3O_4 has been applied as a support for a variety of enzymes, including lipases (CARVALHO *et al.*, 2020; GALVÃO, W. S. *et al.*, 2018; NEMATIAN *et al.*, 2020; NEMATIAN; SALEHI; SHAKERI, 2020; PARANDI *et al.*, 2022; SARNO; IULIANO, 2019; TOUQEER *et al.*, 2019), xylanases (LANDARANI-ISFAHANI *et al.*, 2015), laccases (FORTES *et al.*, 2017), pectinases (FANG *et al.*, 2016), and proteases (PEIMAN; BAHARFAR; MALEKI, 2021). Since magnetite is an oxide containing Fe^{2+} ions susceptible to oxidation and prone to aggregation, it is customary to apply a protective layer of SiO_2 (FANG *et al.*, 2016; LANDARANI-ISFAHANI *et al.*, 2015; PARANDI *et al.*, 2022; PEIMAN; BAHARFAR; MALEKI, 2021) to the nanoparticles. Molecules such as 3-aminopropyltriethoxysilane (APTES) (FANG *et al.*, 2016; GALVÃO, W. S. *et al.*, 2018; NEMATIAN *et al.*, 2020; NEMATIAN; SALEHI; SHAKERI, 2020), polydopamine (TOUQEER *et al.*, 2019), polyglycerol (LANDARANI-ISFAHANI *et al.*, 2015), and

polyethyleneimine (KHOOBI *et al.*, 2015) play a crucial role in complementing the colloidal stability of the support, thereby averting aggregation.

Amino groups are commonly found in most molecules used to functionalize magnetic nanoparticles for immobilizing enzymes. These groups can be easily activated with glutaraldehyde (GLU) to covalently immobilize enzymes through the amino groups present in terminal amino acids (GALVÃO, W. S. *et al.*, 2018; KHOOBI *et al.*, 2015). The advantage of immobilizing enzymes through multipoint covalent bonds is that it preserves the enzyme in its active state, preventing leaching during use. However, it's important to note that this method may have a negative impact on catalytic activity due to molecular rigidity (KHOOBI *et al.*, 2015). Moreover, chemical immobilization poses a challenge to the reusability of the support in other applications.

In certain studies, for cost-effectiveness and to minimize interference from non-magnetic materials that could reduce magnetization and impede recovery, enzymes are immobilized solely through physical adsorption. An illustrative example is presented by Carvalho *et al.*, who utilized Fe_3O_4 without surface protection and functionalization to immobilize lipase from *Yarrowia lipolytica* (CARVALHO *et al.*, 2020). They achieved nearly 20 cycles of hydrolysis of olive oil with only a 20% loss in activity. Furthermore, they observed an enhancement in thermostability (2.7 times higher denaturation energy) and increased affinity of the enzyme for the substrate under specific conditions.

Khoobi *et al.* utilized Fe_3O_4 modified with polyethyleneimine (PEI) for both covalent immobilization and adsorption of lipase from *Thermomyces lanuginosa* (KHOOBI *et al.*, 2015). To prevent the enzyme's rigidity on the rigid support, the authors elongated the PEI chain with spacer arms (hexamethylene diisocyanate or glutaraldehyde). They observed enhanced performance in the covalently linked enzyme regarding thermal stability (100% relative activity compared to 66.5% in the free enzyme at 55°C) and pH variations (91.7% relative activity compared to 0.66% at pH 3 for the free enzyme). The improvement was attributed to conformational restriction due to the use of glutaraldehyde. In comparison, chemical immobilization retained 85% of the enzyme activity after 12 usage cycles, as opposed to only 65% in the case of chemical adsorption.

Among the enzymes already immobilized on magnetic catalysts, lipases stand out as the most widely utilized in the scientific literature. These enzymes, classified as triacylglycerol acyl hydrolases, naturally operate on oils and fats without the need for cofactors in ester bond cleavage (CHANDRA *et al.*, 2020; MONTEIRO, Rodolpho R.C. *et al.*, 2020). Lipases extracted from various microorganisms have found extensive applications in biodiesel

production, aligning with the global trend towards renewable energies (BRANDÃO JÚNIOR *et al.*, 2023; MIAO *et al.*, 2018; NEMATIAN *et al.*, 2020; NEMATIAN; SALEHI; SHAKERI, 2020; PARANDI *et al.*, 2022; SARNO; IULIANO, 2019; TOUQEER *et al.*, 2019). Moreover, they demonstrate versatility across diverse sectors, including food (KHOOBI *et al.*, 2015), pharmaceuticals (BEZERRA *et al.*, 2017; GALVÃO, W. S. *et al.*, 2018), detergents and fine chemicals (CHANDRA *et al.*, 2020).

One of the most intriguing features of lipases is their remarkable combination of high regio- and enantioselectivity, combined with the ability to recognize a broad spectrum of substrates (ALEJALDRE *et al.*, 2023). This characteristic proves exceptionally valuable in the synthesis of pharmaceuticals, where achieving enantiomers with high purity is crucial. For example, Galvão *et al.* employed a covalently linked lipase from Pseudomonas fluorescens immobilized on Fe_3O_4@APTES-GLU nanoparticles for the kinetic resolution of secondary alcohols used as precursors for important drugs such as (+)-Indatraline, (+)-Sertraline, and rasagiline mesylate. They achieved (S)-indanol with remarkable selectivity (enantiomeric excess > 99%, enantioselectivity > 200) in just 1.75 hours at 50°C (GALVÃO, W. S. *et al.*, 2018).

Another noteworthy aspect of most lipases is the presence of a polypeptide chain that isolates their active sites from the reaction medium, requiring strategies to stabilize their open forms. This lid opens when the enzyme encounters hydrophobic species (akin to the chemical nature of its substrate) (SARNO; IULIANO, 2019). Chemists have leveraged this characteristic to modify nanoparticle surfaces, achieving, in some cases, purification, activation, and stabilization simultaneously in a single step (BARBOSA, Oveimar *et al.*, 2015; MONTEIRO, Rodolpho R.C. *et al.*, 2020).

The surveyed studies highlight that the advancement of supports constitutes a dynamic realm striving to enhance stability and customize the mechanisms through which enzymes function. Surface engineering, involving considerations of morphology and functional groups, the microenvironment in which enzymes are housed, along with immobilization conditions such as pH, temperature, ionic strength, agitation, time, and surfactants, presents a diverse set of variables that can be precisely adjusted to further maximize the potential of enzymes.

1.6 Conclusions and thesis outline

The exploration of magnetic nanoparticles in catalysis, environmental applications, biodiesel production, and enzymatic catalysis presents a diverse scenario. Surface modification and protection strategies, as well as enzyme immobilization, offer ways to obtain catalysts with high stability and activity. The continuous development of support materials, controlling size, morphology, structural composition, and surface functional groups, along with the optimization of reaction conditions, will allow the full potential of these systems in science and industry to be exploited.

In this PhD thesis, magnetic nanoparticles in the form of alloys or oxides were used as chemical or biochemical catalysts, acting as a support or as the catalyst itself. These multiple facets explored aim to contribute to the knowledge of the synthesis, characterization, and application of magnetic nanoparticles, as well as to highlight the potential of these materials in environmentally relevant catalysis.

Chapter 2 focuses on FeCo nanoalloys, leveraging the metals in this composition as catalysts for the oxidation of organic pollutants (rhodamine B) with peroxymonosulfate. The synthesis parameters of the polyol are explored with a view to achieving the highest alloy yield. The high saturation magnetization of these materials is put to the test to demonstrate the recoverability of this catalyst.

Chapter 3 shifts the focus to the use of magnetic nanoparticles as supports for enzymes, with a specific emphasis on lipases, particularly Lipase A from *Candida antarctica*. Surface modification was carried out with L-cysteine, providing multiple biocompatible functional groups ($-COO^-$, $-SH$, and $-NH_2$) to anchor the enzyme. The material underwent thorough investigation with structural, morphological, and magnetic characterizations. Immobilization parameters were studied to achieve the best performance and stability of the enzyme.

Finally, Chapter 4 presents the general conclusions of the thesis, while Chapter 5 lists the publications made during the doctorate. Bibliography and the appendix are provided at the end of this document.

1.7 Thesis objectives

This thesis aimed to develop magnetic nano catalysts for environmentally relevant reactions. The specific objectives of the thesis are as follows:

- Synthesize magnetic nanoparticles in the form of alloys and oxides and characterize them in terms of their structural, morphological, and magnetic properties.

- Develop a magnetic catalyst for the activation of peroxymonosulfate and identify the optimum catalysis conditions.

- Devise a suitable support for the immobilization of lipases, while investigating the parameters associated with immobilization and stability.

2 CHAPTER 2 – FeCo@C NANOCOMPOSITES AS EFFICIENT PEROXYMONOSULFATE ACTIVATOR FOR ORGANIC POLLUTANTS DEGRADATION

Sulfate-based advanced oxidation processes (AOPs) are renowned for their exceptional capacity to degrade refractory organic pollutants due to their wide applicability, cost-effectiveness, and swift mineralization and oxidation rates. The primary sources of radicals in AOPs are Persulfate (PS) and peroxymonosulfate (PMS) ions, sparking significant interest in their mechanistic and catalytic aspects. To develop a novel nano-catalyst for AOPs, particularly for PMS activation, we synthesized carbon-coated FeCo nanoparticles (NPs) using hydrothermal methods based on the polyol approach. Various synthesis conditions were investigated, and the NPs were thoroughly characterized regarding their structure, morphology, magnetic properties, and catalytic efficiency. The FeCo phase was primarily obtained at $[OH^-]$ / $[Metal] = 26$ and $[Fe]$ / $[Co] = 2$ ratios. Moreover, as the $[Fe]$ / $[Co]$ ratio increased, the degree of xylose carbonization to form a carbon coating on the NPs also increased. The NPs exhibited a spherical morphology with agglomerates of varying sizes. Vibrating-sample magnetometer analysis (VSM) indicated that a higher proportion of iron resulted in NPs with higher saturation magnetization (up to 167.8 emu g^{-1}), attributed to a larger proportion of FeCo bcc phase in the nanocomposite. Optimal catalytic conditions for degrading 100 ppm rhodamine B (RhB) included 5.0 mg of NPs, 2 mM PMS, pH 7.0, and a 20-minute reaction at 25 °C. Notably, singlet oxygen was the predominant specie in the AOP, followed by sulfate and hydroxyl radicals. The catalyst could be reused for up to five cycles, retaining over 98% RhB removal, albeit with increased metal leaching. Even in the first use, dissolved Fe and Co concentrations were 0.8 ± 0.3 and 4.0 ± 0.5 mg L^{-1}, respectively. The FeCo catalyst proved to be effective in dye removal and offers the potential for further refinement to minimize Co^{2+} leaching.

2.1 Introduction

In recent decades, escalating industrialization and the continual introduction of novel chemicals into water bodies have accentuated the need for effective remediation strategies. Particularly, synthetic organic dyes originating from the textile industry have emerged as a significant concern due to their toxicity and resistance to biodegradation (GONG, Cheng *et al.*, 2017). Among these, rhodamine B (RhB), a xanthene compound extensively used in various industries, poses ecological hazards, including inhibiting sunlight penetration and impeding oxygen regeneration in water bodies (ISARI *et al.*, 2018; JOSHIBA *et al.*, 2021). The stable and water-soluble nature of RhB, coupled with its adverse effects on human health, necessitates its removal from wastewater before disposal into the environment (SPESSATO *et al.*, 2021).

Various strategies have been proposed to address this issue, such biological treatment (PAVITHRA *et al.*, 2019), adsorption (SPESSATO *et al.*, 2021), filtration membrane (TAO *et al.*, 2017), electrocoagulation (PIRKARAMI; OLYA, 2017), and advanced oxidation processes (AOPs) (LI, Tong *et al.*, 2021). AOPs, relying on reactive oxygen species like singlet oxygen ($^1O_2$), and hydroxyl ($^\bullet OH$), superoxide ($O_2^{\bullet-}$), and sulfate ($SO_4^{\bullet-}$) radicals, originated from the activation of oxidants such as peroxymonosulfate (PMS), have gained attention for their efficiency, versatility, environmental compatibility, and rapid kinetics (CAO *et al.*, 2020; LI, Tong *et al.*, 2021).

PMS, widely employed in AOPs, produces sulfate radicals with superior reduction potential (E_0 = 2.5 - 3.1 eV), good selectivity, and a broad working pH range (2.0 - 11.0) (GONG, Cheng *et al.*, 2017; HOU, Jifei *et al.*, 2021; ZHAO, Guoqing *et al.*, 2020). The activation of PMS generates singlet oxygen, sulfate, peroxymonosulfate ($SO_5^{\bullet-}$) and hydroxyl radicals, with sulfate radicals predominating due to primary reactions, while the contribution of $SO_5^{\bullet-}$ is typically negligible (FAN, Yanan *et al.*, 2017; GHANBARI; MORADI, 2017; GONG, Cheng *et al.*, 2017). In specific scenarios where PMS serves as an electron donor, $^1O_2$ becomes predominant (XUE *et al.*, 2023). Despite its moderate redox potential (2.2 V), singlet oxygen offers advantages, including the ability to withstand a broad pH range (3-11) and resist the interference of inorganic ions and organic matter, both of which can significantly disrupt sulfate radicals (ZHANG, Rui *et al.*, 2023).

Transition metals, notably Fe, Co, Mn, and Ce, are widely used in PMS activation for their efficiency, simplicity, and cost-effectiveness. Cobalt-based catalysts, despite their high efficacy, are hindered by toxicity, necessitating methods to prevent leaching and secondary

pollution. Consequently, heterogeneous catalysis, particularly using magnetic nanoparticles, has become preferable for catalyst recovery.

Among magnetic nanoparticles, Fe and Co oxides and hydroxides exhibit noteworthy catalytic properties, leveraging synergistic effects to enhance catalyst stability (GONG, Cheng *et al.*, 2017; ZHOU; ZHANG; HU, 2020). This study focuses on assessing the catalytic potential of a FeCo nanoalloy, synthesized using a novel polyol method in a hydrothermal reactor, for the degradation of RhB employing PMS. Apart from providing advantages like improved quality control over the obtained material, this approach demonstrates promise in the one-step synthesis of FeCo and its protection with carbon structures known as hydrochar.

Hydrochars, also recognized as PMS activators, operate predominantly through the non-radical route, offering the potential to fortify the catalyst with robustness and anti-interference capabilities (GASIM *et al.*, 2022; XUE *et al.*, 2023; ZHANG, Rui *et al.*, 2023). The parameters governing the synthesis of FeCo with biochar were optimized within this innovative polyol approach to enhance the catalyst's performance.

2.2 Materials and Methods

2.2.1 Materials

Iron (II) chloride tetrahydrate ($FeCl_2 \cdot 4H_2O$, Sigma-Aldrich – São Paulo – Brazil, purity $\geq$ 98 %), cobalt (II) acetate tetrahydrate ($Co(CH_3COO)_2$, Neon – São Paulo – Brazil, purity $\geq$ 98 %), ethylene glycol ($C_2H_6O_2$, Dinâmica – São Paulo – Brazil, purity $\geq$ 99.5%), sodium hydroxide (NaOH, Dinâmica – São Paulo – Brazil, purity $\geq$ 98%), xylose ($C_5H_{10}O_5$, Dinâmica – São Paulo – Brazil, purity $\geq$ 99%), rhodamine B ($C_{28}H_{31}ClN_2O_3$, Sigma-Aldrich – São Paulo – Brazil, purity $\geq$ 95%), OXONE® potassium peroxymonosulfate ($KHSO_5 \cdot 0.5KHSO_4 \cdot 0.5K_2SO_4$, Sigma-Aldrich – São Paulo – Brazil), L-histidine monohydrochloride monohydrate ($C_6H_9N_3O_2 \cdot HCl \cdot H_2O$, INLAB – São Paulo – Brazil, purity $\geq$ 98.5%), tert-butyl alcohol (($CH_3)_3COH$, Neon – São Paulo – Brazil, purity $\geq$ 99%), ethanol (C_2H_6O, Vetec – Rio de Janeiro – Brazil, purity $\geq$ 99.5%), nitric acid (HNO_3, Synth – São Paulo – Brazil, purity $\geq$ 65%), sulfuric acid (H_2SO_4, Vetec – Rio de Janeiro – Brazil, purity $\geq$ 99%), potassium iodide (KI, Dinâmica – São Paulo – Brazil, purity $\geq$ 99%), sodium bicarbonate ($NaHCO_3$, Vetec – Rio de Janeiro – Brazil, purity $\geq$ 99.5%) were of analytical grade and used without further purification.

2.2.2 Synthesis of FeCo@Co/C nanoparticles

The FeCo-Co/C nanoalloys were synthesized by a modified polyol process, as shown in Fig. 6 (a) (ZAMANPOUR *et al.*, 2012). Briefly, 409 mg of $FeCl_2·4H_2O$ and 254 mg of $Co(acac)_2·4H_2O$ were dissolved in ethylene glycol, and the mixture was stirred at 60°C. Once a clear solution formed, 450 mg of xylose was introduced to form the hydrochar structures, and OH^- concentration was adjusted to 1.30, 1.50, 1.75, or 2.03 mol L^{-1} by adding NaOH. The final mixture, with a volume of 60 mL, was vigorously stirred for 30 min and then transferred into a Teflon-lined stainless-steel autoclave, heated at 200°C for 12 hours. The resulting product was collected via magnetic decantation, washed multiple times with ethanol and distilled water, and then vacuum-dried for 24 hours. Another synthesis batch followed the same procedure, but the molar ratio [Fe] / [Co] was varied at 1.0, 1.5, 2.0, 2.5, or 3.0, while maintaining a constant OH^- concentration of 2.03 mol L^{-1}.

2.2.3 Characterization methods

The nanoparticles were subjected to various analyses. X-ray Powder Diffraction (XRPD) was conducted using an Xpert Pro MPD diffractometer (Panalytical) with Bragg–Brentano geometry in the range of 30° – 100° at a rate of 1°·min^{-1}. We used CoKα radiation (k = 1.78896 Å), and the tube operated at 40 kV and 30 mA. The selected samples underwent Rietveld refinement, and the average crystallite sizes (D) were determined using the Scherrer equation, $D = K·\lambda/\beta·cos(\theta)$ (BAGBI *et al.*, 2017). In this equation, K is a constant dependent on the shape of the particles (for spheres, K=0.94), λ represents the wavelength of the electromagnetic radiation ($K_{alpha1}Co$ = 1.788965 Å), β is the full width at half maximum, and θ is the diffraction angle.

Fourier Transform Infrared Spectroscopy (FTIR) analysis was performed with a Perkin-Elmer 2000 spectrophotometer. Prior to analysis, the samples were dried, grounded to a powder, and then pressed into disk format (~ 10 mg of the sample to 100 mg of KBr).

Transmission Electron Microscopy (TEM) analyses were carried out using a HITACHI HT7700 operating at an accelerating voltage of 120 kV. The samples were dispersed in ethanol, a droplet was placed on a 300-mesh carbon-coated copper grid, and they were dried overnight under ambient conditions. Scanning Electron Microscopy (SEM) was performed on a SEM FEG Quanta 450 with EDS. The samples were deposited on carbon tape and metalized

with silver using the Metalizator Quorum QT150ES. A pressure of 10 Pa was applied in the SEM chamber, with an incident electron beam of 20 kV.

Figure 6 – Schematic illustration of the hydrothermal synthesis of FeCo nanoparticles (a) and their application as a catalyst for RhB degradation using PMS (b).
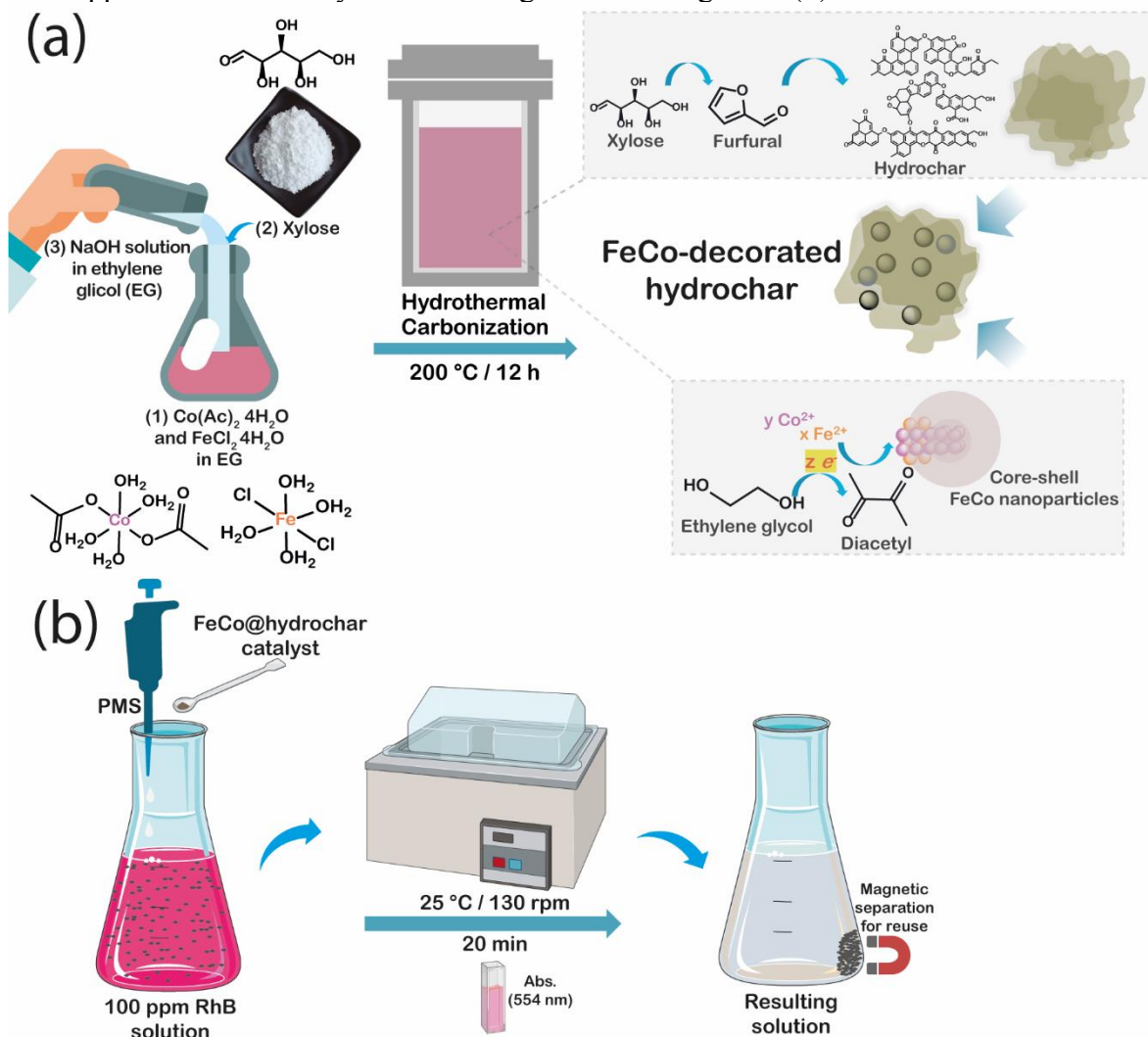
Source: the author.

Thermogravimetric analysis (TGA) was carried out under a nitrogen atmosphere using a Thermogravimetric Analyzer Q50 V20. The weight loss (%) was monitored by heating the samples from 25 to 900 °C at a rate of 10 °C.min^{-1}. The zero time for the thermal degradation study was determined after temperature stabilization.

K-Alpha X-ray photoelectron spectrometer (XPS) was performed using a Thermo Fisher Scientific XPS system equipped with a hemispherical electron analyzer and an aluminum anode (Kα = 1486.6 eV) X-ray source. The analysis was conducted under charge compensation, and the chamber's pressure was maintained below 2×10^{-8} mbar. Survey and high-resolution

spectra were recorded using pass energies of 1 and 0.1 eV, respectively. Data analysis was performed using Origin Pro 9.0.0, and spectrum fitting was carried out using the Shirley method, assuming a mixed Gaussian / Lorentzian peak shape with a fixed Gaussian to Lorentzian ratio of 0.4. The X-ray photoelectron spectra represent the average of three spectra collected at three different regions.

Magnetic properties were investigated using a Vibrating Sample Magnetometer (VSM) Mini 5 Tesla from Cryogenic Ltd. Calibration was performed using a YIG sphere, and after measuring the mass of each sample, the magnetization was expressed in $emu \cdot g^{-1}$.

2.2.4 Catalytic activity tests

Degradation experiments were conducted following the procedure shown in Fig. 6 (b) at room temperature (25 ± 1 °C) maintained by a thermostatic bath. A 250 mL conical flask containing 100 mL of a 100 ppm RhB solution and 5.0 mg (0.05 g L^{-1}) of the $Fe_2Co@C$ catalyst sample was employed. The solution's pH was adjusted to the desired value (3.0 - 9.0) using H_2SO_4 or NaOH solutions, and the appropriate amount of PMS (1.0-2.5 mM) was added.

The RhB concentration was monitored every 2 minutes during the reaction using a Varian Cary 1E UV-Vis spectrometer. For this, the catalyst was separated by precipitation using a NdFeB magnet, and when necessary, 100 µL aliquots of the supernatant were taken and diluted in polystyrene cuvettes containing 2.9 mL of water. The rate of pollutant mineralization was determined after 20 minutes using a Shimadzu TOC-L Total Organic Carbon Analyzer.

To identify the reactive oxygen species responsible for RhB degradation, quenching qualitative assays were performed. Various concentrations of methanol (1-2 M) (OH and SO_4^{2-} radical scavenger), tert-butanol (20-526 mM) (OH scavenger) and l-histidine (5-50 mM) (singlet oxygen scavenger) were studied until the maximum inhibition of the reaction was reached.

The PMS concentration during the RhB oxidation process was monitored using the iodometric spectrophotometric method (WACŁAWEK, S.; GRÜBEL; ČERNÍK, 2015). For this, 400 µL aliquots of the supernatant were taken, mixed with 2.6 mL of a 10% KI and 0.5% $NaHCO_3$ solution. After 1 minute of reaction, the absorbance at 395 nm was measured.

In the recycling experiment, after each use, the catalyst was recovered by magnetic separation, washed successively with water, ethanol, and acetone, and dried at room temperature. Following each use, the supernatant was collected and filtered using a 0.45 µm

Millipore membrane, acidified with HNO_3, and then analyzed for the total concentration of leached Co and Fe using Atomic Absorbance Spectroscopy.

All kinetic curves were fitted using the pseudo-first-order Langmuir-Hinshelwood kinetic model, where PMS is assumed to be in excess, and the reaction rate solely depends on the concentration of rhodamine B ($v=k$[RhB]). In this model, the concentration (C) at a given time (t) is calculated as $C=C_o exp(-kt)$, where C_0 is the initial concentration of RhB, and k is the rate constant. To determine the k values, the linearized version of the equation, $ln\ (C/C_0) = -kt$, was utilized. Graphs of $ln\ (C/C_0)$ *versus* t were plotted to facilitate this analysis.

2.3 Results and Discussion

2.3.1 XRPD

The physical-chemical properties and phase composition of the nanoparticles synthesized through the polyol process depend significantly on the $[OH^-]$ / [Metal] and [Fe] / [Co] ratios used in the synthesis. These parameters were studied and optimized.

First, the impact of the molar ratio $[OH^-]$ / [Metal] was assessed through XRPD, as shown in the diffraction patterns Fig. 7. The sample synthesized with a $[OH^-]$ / [Metal] molar ratio of 26 exhibited diffraction peaks assigned to body centered cubic (bcc) FeCo (JCPDS 00-049-1568), hexagonal close-packed (hcp) Co (JCPDS 00-005-0727), and face centered cubic (fcc) Co (JCPDS 00-15-0806) phases. A higher molar ratio than 26 notably increased the intensity of the peaks related to the bcc FeCo phase compared to those of fcc Co. However, another secondary phase, $CoFe_2O_4$ (JCPDS 00-022-1086), was observed. This suggests that excess hydroxyl ions may promote the formation of hydroxides on the sample's surface, which can be oxidized to $CoFe_2O_4$ due to the presence of oxygen in the solution (JOSEYPHUS, R.J. *et al.*, 2007). In fact, the peaks associated with this oxide had lower intensity than those of the FeCo phase, indicating partial oxidation.

Given that a high $[OH^-]$ / [Metal] molar ratio led to oxide formation, which has weaker magnetism than metal nanoparticles, the molar ratio of 26 was retained, and an optimization of the [Fe] / [Co] molar ratio was conducted. As demonstrated in the XRPD patterns (Fig. 8), two crystalline phases were identified for the sample with a molar ratio of 1, namely, hcp Co (JCPDS 00-005-0727) and fcc Co (JCPDS 00-15-0806). No peak related to FeCo was observed, suggesting no significant reduction from Fe^{2+} to Fe^0 for the formation of the FeCo alloy. Although this phase is present, it is in too low a quantity to be detected by XRD.

As Fe^{2+} ions have a lower reduction potential than cobalt, they are more challenging to reduce, necessitating their excess in the reaction medium.

Figure 7 – XRD patterns obtained for FeCo samples synthesized with different [OH-] / [Metal] molar ratios at 200 °C and [Metal]=0.05 mol/L.
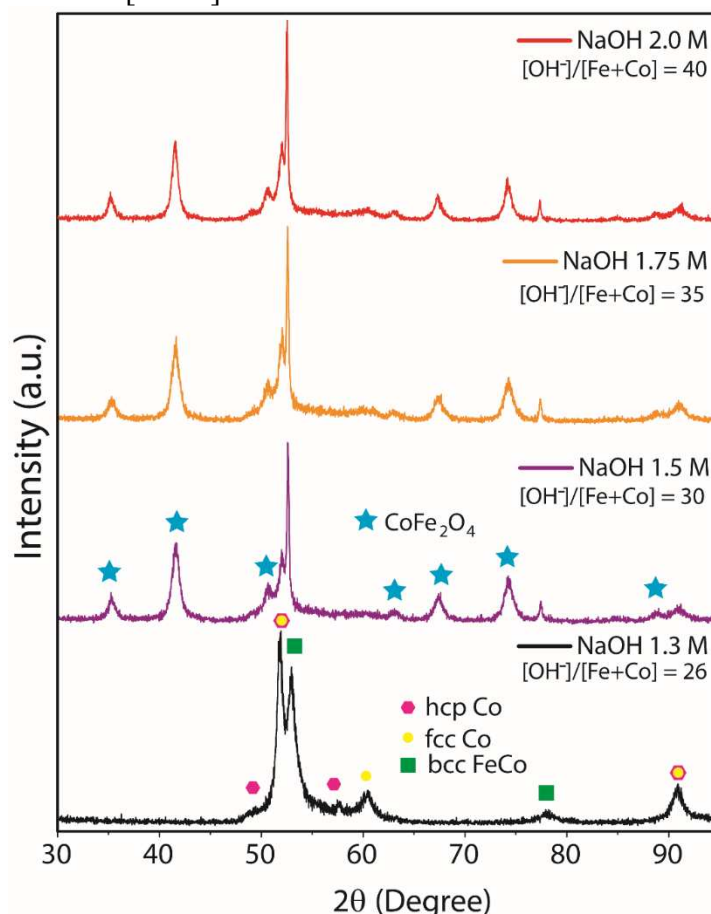
Source: the author.

When the [Fe] / [Co] molar ratio ranged from 1.5 to 3.0, the FeCo phase (JCPDS 00-049-1568) was identified. The alloy-related peaks became progressively more intense with increasing Fe concentration. However, when molar ratios of 2.5 and 3.0 for [Fe] / [Co] were applied, a secondary phase (JCPDS 00-022-1086) associated with Co ferrite was also detected. Its formation appears to be favored by the excess of Fe in the solution. Notably, the peaks assigned to $CoFe_2O_4$ had lower intensity than those for FeCo or Co phases, suggesting its possible formation on the surface of FeCo nanoparticles, likely through their partial oxidation.

Figure 8 – XRD patterns for obtained for FeCo samples synthesized with different [Fe] / [Co] molar ratios and [NaOH] = 1.35 mol/L.
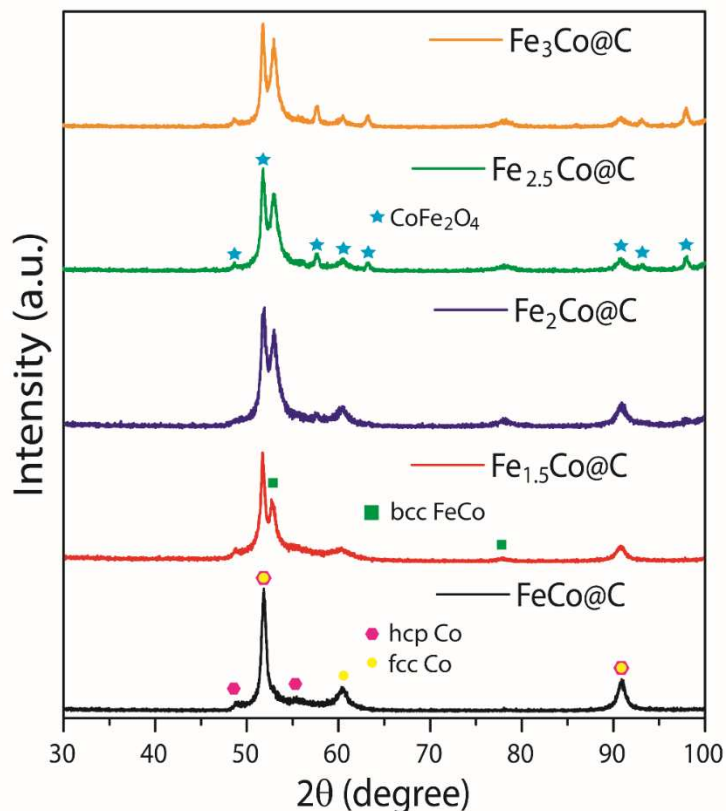
Source: the author.

As samples with high Fe/Co molar ratios produced oxides with low magnetization, the FeCo@C, Fe$_{1.5}$Co@C and Fe$_2$Co@C samples were selected for further investigation. An in-depth structural analysis was conducted by refining the XRPD patterns using the Rietveld method (RIETVELD; IUCR, 1969). Fig. 9 (a) shows the successful fitting of the experimental data to the Inorganic Crystal Structure Database (ICSD) reference standards.

The structural parameters obtained through Rietveld refinement are presented in Table 2, where the percentage of errors (R_{WP}, %) and goodness of fit (χ^2) confirm a close match between the experimental and theoretical values. For the 1:1 molar ratio of metal precursors, the weight fractions of cubic and hexagonal Co phases were 71.82 and 28.18 %, respectively. Under this reaction condition, the polyol method was unable to reduce iron ions sufficiently to form detectable FeCo alloy, as indicated by the absence of FeCo-related peaks in the XRPD analysis.

Figure 9 – Refined XRPD patterns (a), FTIR spectra (b), and TGA (c) and DTG (d) curves for the thermal degradation for FeCo samples synthesized with [NaOH] = 1.35 mol/L and [Fe] / [Co] molar ratios from 1:1 to 2:2.
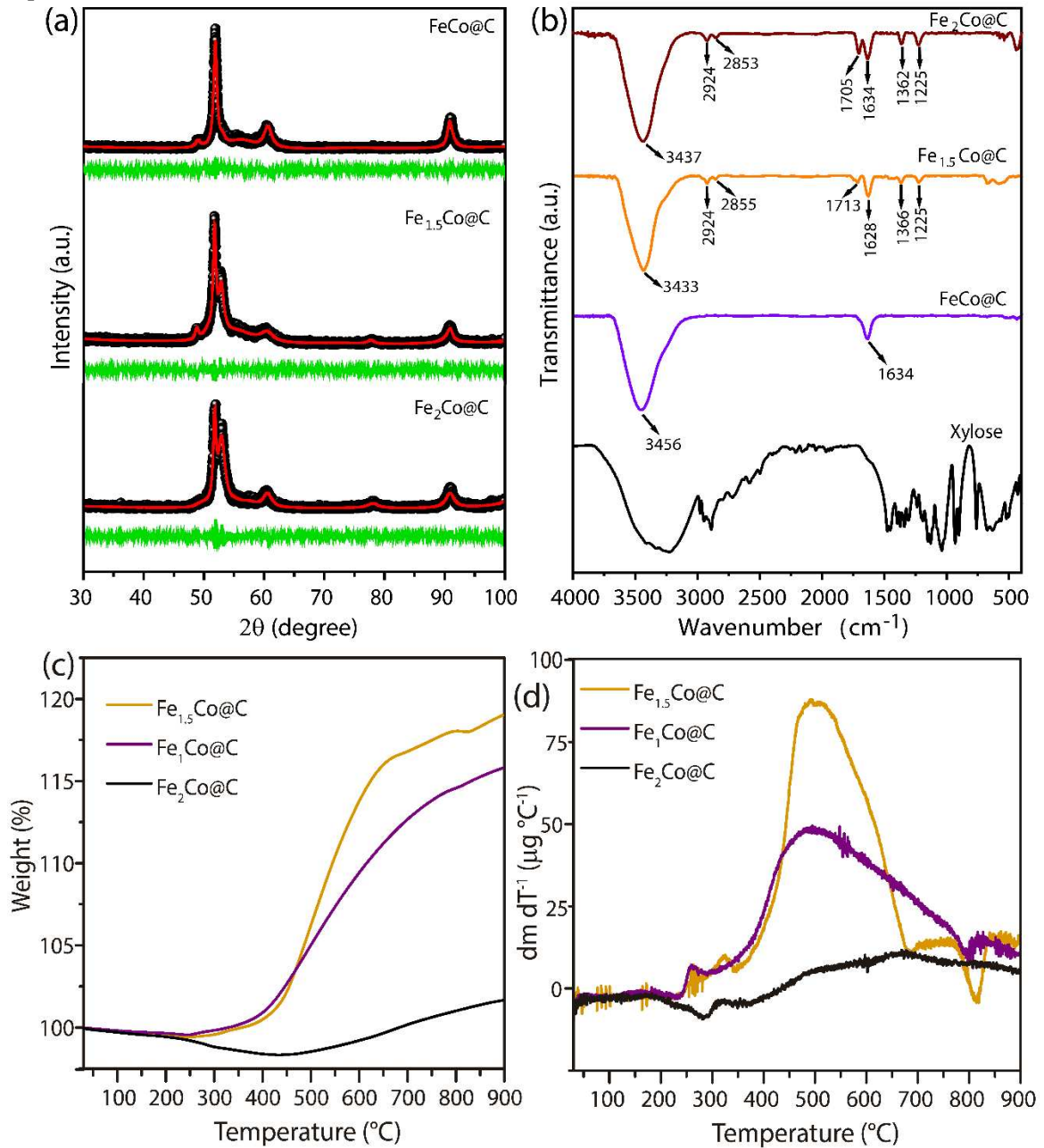
Source: the author.

By increasing the molar fraction of iron ([Fe] / [Co]) to 1.5:1 and 2:1, 52.58 and 65.50% w/w of FeCo (bcc) were obtained. The weight fraction of Co (fcc) decreased to 34.42 and 11.94%, respectively, while the yield of Co (hcp) was reduced to 13% w/w and then increased to 22.56 % w/w. Therefore, the synthesis of FeCo nanoparticles has a greater influence on the formation of Co (fcc). The energy difference between these phases is small, and while Co (hcp) is thermodynamically more stable at temperatures below ~ 693 K, both hcp and fcc phases are typically obtained in the synthesis (ANDREEV *et al.*, 2015). The

predominance of Co (fcc) over Co (hcp) in FeCo/Co-C and Fe$_{1.5}$Co/Co-C samples can likely be attributed to the prevalence of kinetics over thermodynamic equilibrium for the chemical reaction (KALYAN KAMAL *et al.*, 2009). At a 2:1 molar ratio, the Co^{2+} concentration is significantly reduced, impairing the kinetics of Co (fcc) NPs formation.

The average crystallite size of Co (fcc) and Co (hcp) nanoparticles obtained with 1:1 molar ratio of precursors was 14.88±0.03 and 10.38±0.01 nm, respectively. When the available Co^{2+} concentration for reduction decreases, the average crystallite sizes increase as the reduction rate decreases and the nucleation time increases. At low Co^{2+} concentrations, fewer Co (fcc) seeds are formed, and the remaining ions are utilized for crystal growth (SHOKUHFAR; AFGHAHI, 2014).

Table 2 – Structural parameters extracted through Rietveld refinement of the XRPD patterns.

Sample	R_{wp} (%)	χ^2	Phases	Lattice parameters (Å)	Weight fraction (%)	Average crystallite size (nm)
FeCo/Co-C	23.67	1.173	Co (fcc)	a = 3.5614	71.82	14.88±0.03
			Co (hcp)	a = b = 2.5047 c = 4.0237	28.18	10.38±0.01
Fe$_{1.5}$Co/Co-C	14.35	0.8948	FeCo (bcc)	a = 2.8622	52.58	9.93±0.01
			Co (fcc)	a = 3.5759	34.42	33.4±0.3
			Co (hcp)	a = b = 2.5184 c = 4.2107	13.00	14.88±0.01
Fe$_2$Co/Co-C	20.81	0.9126	FeCo (bcc)	a = 2.8434	65.50	9.38±0,01
			Co (fcc)	a = 3.5544	11.94	21.78±0.09
			Co (hcp)	a = b = 2.4679 c = 3.8722	22.56	6±2

Source: the author.

2.3.2 FTIR

The FTIR analysis was conducted to examine the chemical interactions in the FeCo samples consisting of only metallic phases. The spectra for these samples and pure xylose are displayed in Fig. 9 (b). All FeCo samples exhibited bands around 3440 and 1630 cm^{-1}, which were attributed to the stretching and bending vibrations of hydroxyl groups in the xylose derivative (YI *et al.*, 2020). Additionally, the Fe$_{1.5}$Co@C and Fe$_2$Co@C samples displayed bands around 2924, 2855, 1705, 1360, and 1225 cm^{-1}, which became more pronounced with the increased Fe^{2+} molar ratio in the reaction medium. This observation suggests that iron ions influence xylose carbonization. Indeed, the literature reports that carbon sources like

saccharides, under solvothermal conditions, undergo dehydration and polymerization catalyzed by iron ions, leading to the formation of carbon-based structures known as hydrochar (HUANG *et al.*, 2020; SAADATTALAB *et al.*, 2020; SHI *et al.*, 2019).

The bands observed in the spectra around 2924 and 2855 cm^{-1} can be attributed to asymmetric and symmetric stretching of aliphatic C-H bonds, respectively (YI *et al.*, 2020). The band observed around 1705 cm^{-1} may be associated with a carboxyl group and/or a carbonyl group, formed through the dehydration of hydroxyl groups in xylose (KANG *et al.*, 2012). Interestingly, this band is evident only in the samples containing the FeCo phase, suggesting a connection between xylose oxidation (carboxylate formation) and the supply of electrons to reduce iron ions and form the FeCo phase. The bands at approximately 1360 cm^{-1} and 1225 cm^{-1} are related to C-H bending and C-O stretching from carbonized xylose, respectively (SHI *et al.*, 2019; YI *et al.*, 2020). After the solvothermal process, most of the vibrational modes in the fingerprint region (1450-400 cm^{-1}) for xylose, related to hemiacetal bonds, anomers of its cyclic form, and C-OH stretching from alcohol, disappear, indicating its degradation (URBANSKI; HOFMAN; WITANOWSKI, 1959).

2.3.3 TGA

TGA was conducted to assess the thermal stability of samples containing solely metallic phases. The TGA curves and their first derivative (DTG) for each sample are displayed in Figs. 9 (c) and 9 (d), respectively. Up to 246 °C, weight losses were minimal, measuring only 0.55, 0.58, and 0.88% for samples with Fe / Co molar ratios of 1:1 (FeCo@C), 1.5:1 (Fe$_{1.5}$Co@C) and 2:1 (Fe$_2$Co@C), respectively. These values indicate a low presence of moisture absorbed in the samples and suggest a correlation between the higher presence of xylose derivatives (as suggested by FTIR analysis) and the weight loss in this range. Beyond this temperature, the samples exhibited varying behaviors.

While the Fe$_2$Co@C sample continued to experience weight loss, the others showed an increase in mass. According to the DTG curves, this phenomenon was more pronounced in the Fe$_{1.5}$Co@C sample, with a peak at 493 °C, while the FeCo@C sample peaked at 495 °C. Weight increments in TGA, due to thermal events, are common for metallic materials and are associated with metal oxidation, as documented in the literature (BARBOSA, Felipe Fernandes *et al.*, 2020; BARBOSA, Felipe Fernandes; PERGHER; BRAGA, 2019; THIRUMAL *et al.*, 2010).

Since samples with higher iron levels are more susceptible to oxidation, resulting in heavier residues, it was expected that the Fe$_2$Co@C sample would exhibit a greater weight increase. However, interestingly, this sample displayed a lower weight increase, indicating a level of protection against oxidation. This observation aligns with the formation of a carbon layer surrounding the nanoparticles, as reported in the literature (BARBOSA, Felipe Fernandes; PERGHER; BRAGA, 2019).

The residues at 900 °C amounted to 119.0%, 115.7% and 101.6%, respectively, for samples with iron molar ratios of 1.5:1, 1:1 and 2:1. These values are lower than those observed in other studies, indicating partial oxidation of the metals (BARBOSA, Felipe Fernandes *et al.*, 2020; BARBOSA, Felipe Fernandes; PERGHER; BRAGA, 2019; THIRUMAL *et al.*, 2010). An explanation for the higher residue percentages in samples with the molar ratios of 1.5:1 and 1:1 may be associated with the lesser amount of organic matter deposited on their surfaces, preventing the formation of a fully effective carbon coating.

2.3.4 SEM

SEM analysis was conducted to assess the morphology of the FeCo nanoparticles. Fig. 10 (a) – (f) displays the micrograph, the EDS mapping, and their respective spectra for each sample. All samples exhibited primarily spherical morphology with varying sizes. Many of these spheres had a rough surface. Interestingly, the Fe$_{1.5}$Co@C sample showed some particles with a flower-shaped morphology. Although the XRPD analysis indicated average crystallite sizes not exceeding 33.4 ± 0.3 nm and broad diffraction peaks (associated with nanometric particles), the spheres had an average size of 0.82±0.36, 1.45±0.79 and 1.62±1.00 μm, respectively, for samples with an iron molar ratio from 1 to 2. These values can be explained by considering that these spherical structures are clusters of nanoparticles. With an increase in the iron molar ratio, these agglomerates increased in size and became more polydisperse.

Figure 10 – SEM images for FeCo samples synthesized with [NaOH] = 1.35 mol/L and [Fe]/[Co] molar ratios from 1:1 to 2:2, FeCo@C (a), $Fe_{1.5}Co@C$ (c) and $Fe_2Co@C$ (e). EDS mapping is shown in insets in the images (a), (c) and (e), while their respective spectrum is given in (b), (d) and (f).
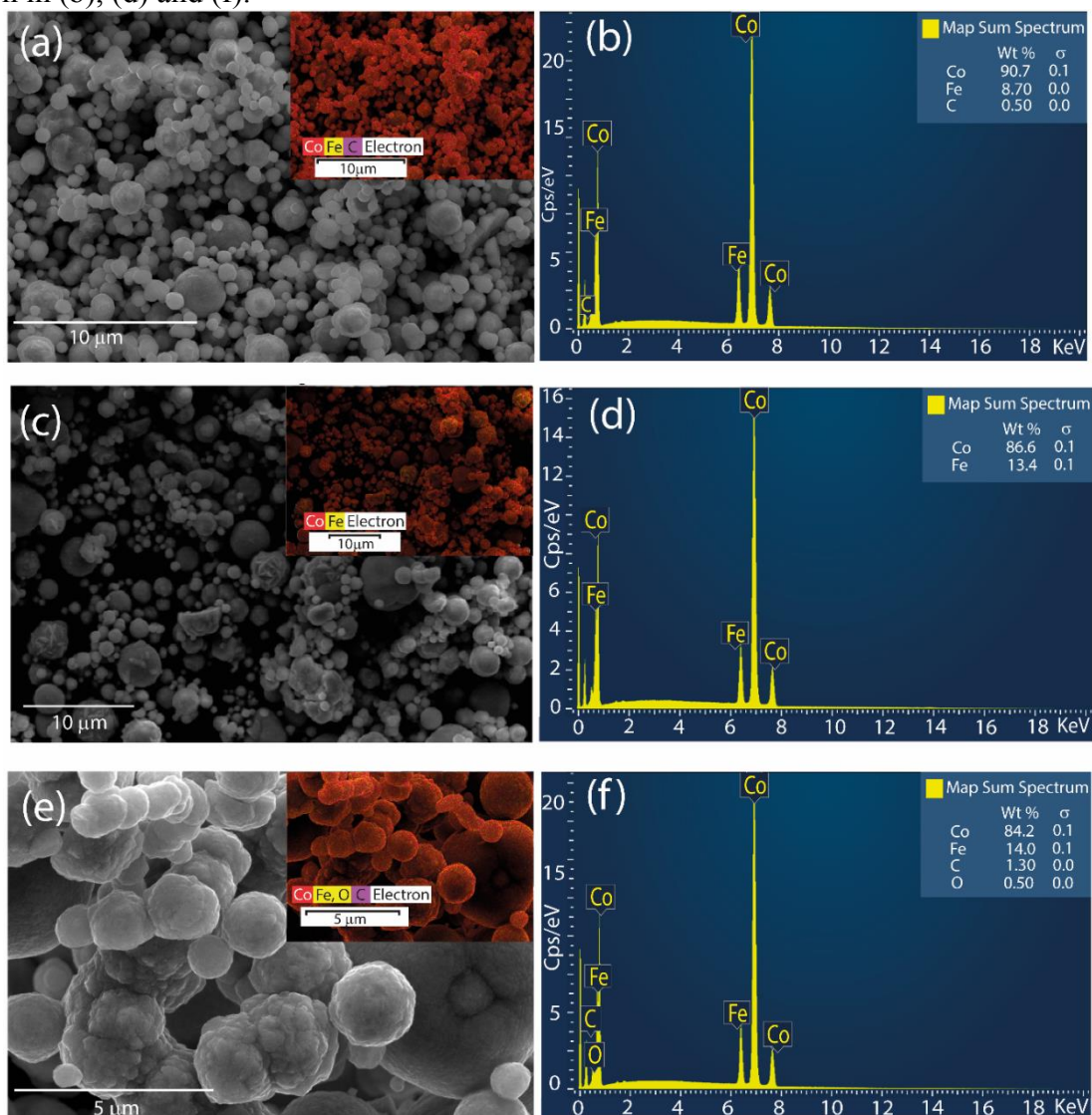
Source: the author.

The insets in Figs. 10 (a), 10 (c) and 10 (e) display the EDS images of the samples. A noticeable high density of cobalt is apparent on the surface of the clusters, particularly in the FeCo@C sample. This density diminishes as the molar proportion of iron increases, as illustrated in the EDS spectra, Figs. 10 (b), 10 (d) and 10 (f). Moreover, the distribution of elements on the cluster surfaces is more uniform for the $Fe_2Co@C$ sample, as expected due to the progressive increase in the percentage of the FeCo phase.

It is noteworthy that larger particles, including those with flower-shaped morphology, exhibit a higher iron density. This observation suggests a pronounced tendency for the FeCo phase to agglomerate, either due to interactions between the particles or the

remaining magnetization. Additionally, the higher density of cobalt in relation to iron on the surface of the microspheres implies that the FeCo phase is more concentrated in the center of these structures, which goes unaccounted for due to the limitation of the EDS technique to the surface.

2.3.5 TEM

As SEM analysis did not allow for the identification of nanoparticles within the clusters, TEM analysis was conducted on samples separated through centrifugation and magnetic decantation. The micrographs for samples separated using a magnet are presented in Fig. 11. These images depict particles with morphology and sizes like those observed in the SEM analysis. These particles are closely clustered, making it challenging to discern the boundaries of the nanoparticles. Additionally, a veil-like structure surrounding these particles, identified as carbon sheets, is evident. Fig. 11 (d) also reveals a cluster of nanoparticles around a micrometric particle, with sizes consistent with the XRPD analysis findings.

Figure 11 – TEM images of FeCo (a, and b), $Fe_{1.5}Co$ (c and d) separated by magnetic decantation.
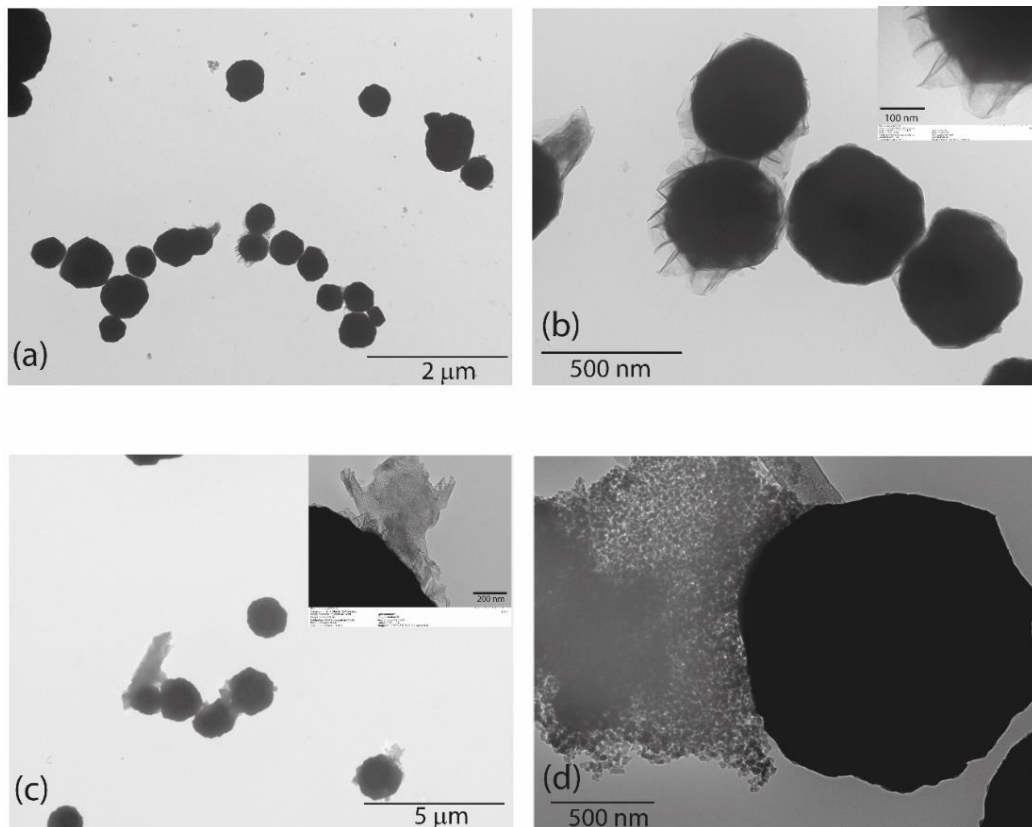
Source: the author.

Fig. 12 displays the micrographs for samples separated by centrifugation. In contrast to magnetically separated samples, no micrometric spheres were observed. Thus, the formation of these structures appears to be influenced by exposure to a magnetic field, aligning with the hypothesis that the clusters' formation is partially related to the remaining magnetization. The nanoparticles' boundaries are more easily identifiable in the micrographs, but calculating their average particle size remains challenging due to their mixture with carbon sheets.

Figure 12 – TEM images of FeCo@C (a and d), Fe$_{1.5}$Co@C (b and e) and Fe$_2$Co@C (c and f) samples, synthesized using [NaOH] = 1.35 mol/L.
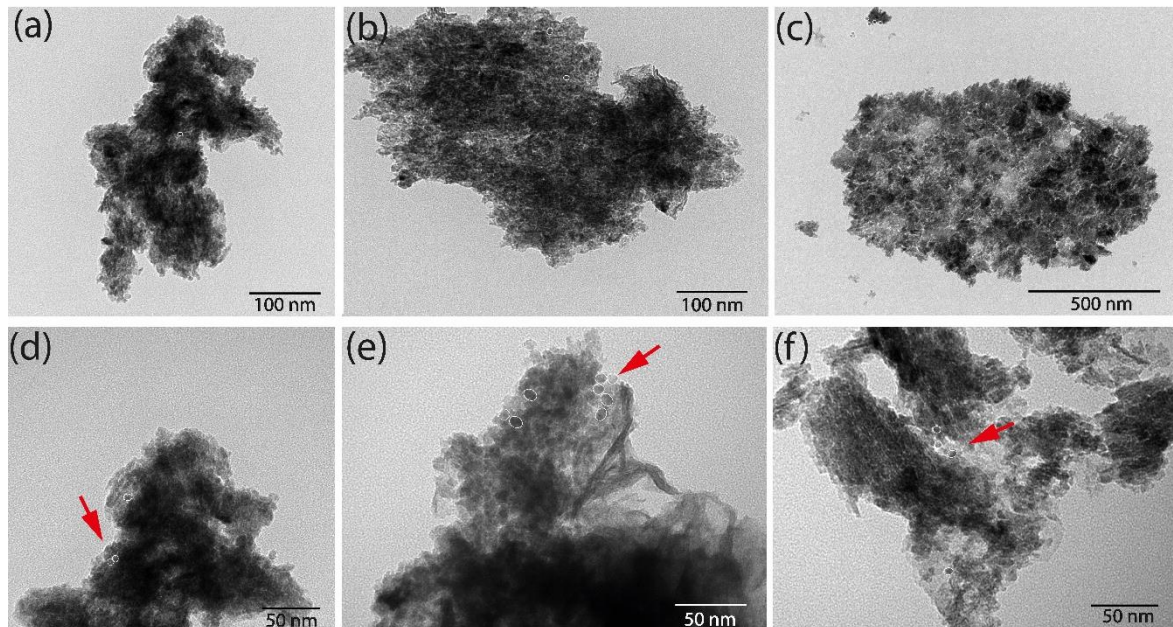
Source: the author.

2.3.6 Magnetic measurements

The magnetization curves at 300 K for the samples containing only metallic phases are displayed in Fig. 13. The low-field sections of the curves are shown in the inset, where noticeable narrow hysteresis loops are evident for all samples, indicating typical behavior of a soft magnetic material. The VSM analysis supports the relationship between the micrometric particles observed in TEM and SEM analyses and the formation of clusters due to interparticle interactions. Moreover, a more significant hysteresis would be observed if the particle size were in the micrometer range (PONRAJ *et al.*, 2020).

The saturation magnetization (M_s), remanent magnetization (M_r), and coercivity (H_c) values were extracted from the magnetization curves in Fig. 13, and the results are

presented in Table 3. The Fe₂Co@C sample exhibited the highest M_s value (167.8 emu g⁻¹), which aligns with the highest FeCo weight fraction observed in XRPD analysis. However, the Fe₁.₅Co@C sample had a slightly lower M_s value than that found for FeCo@C. This observation suggests the presence of non-magnetic and/or low-moment materials in the samples, such as carbon sheets and partially oxidized metallic phases. The TGA results indicated a greater predisposition for the Fe₁.₅Co@C sample to become oxidized. Furthermore, the FTIR analysis suggested a larger percentage of organic phase in Fe₁.₅Co@C than in FeCo@C, contributing to the lower M_s value. Considering the M_s values of FeCo and Co bulks, which are 240 and 163 emu g⁻¹, respectively, the M_s values for all samples are below expectations, indicating a significant quantity of organic matter within them (I. SCHWERDT *et al.*, 2012).

Figure 13 – Magnetization curves for FeCo samples synthesized with [NaOH] = 1.35 mol/L and [Fe] / [Co] molar ratios ranging from 1:1 to 2:2.
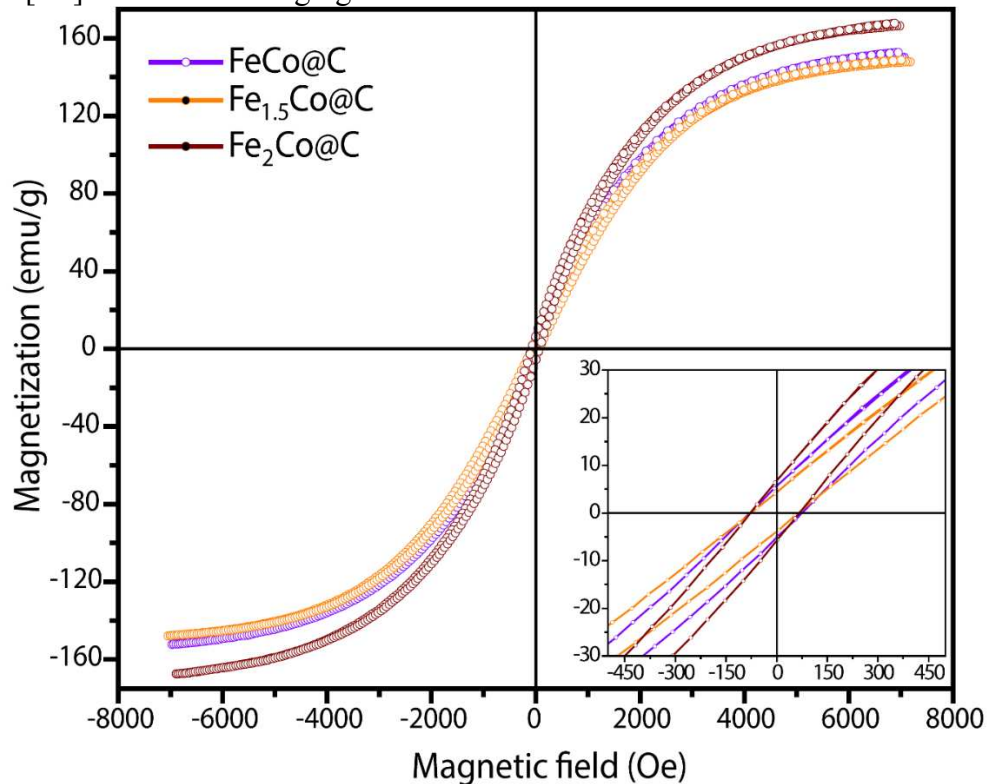
Source: the author.

Table 3 – Magnetic parameters extracted from magnetization curves for FeCo samples synthesized with [NaOH] = 1.35 mol/L and [Fe] / [Co] molar ratios ranging from 1:1 to 2:2.

Sample	M_s (emu g⁻¹)	M_r (emu g⁻¹)	H_c (Oe)
FeCo@C	152.7	5.1	77.5
Fe₁.₅Co@C	148.8	3.9	69.8
Fe₂Co@C	167.8	5.9	72.6

Source: the author.

The ZFC and FC magnetization curves for the Fe$_{1.5}$Co@C sample under a magnetic field of 10 mT are depicted in Fig. 14. As the temperature increases from 5 to 300 K, the ZFC magnetization increases, with more spins overcoming the energy barrier to align with the applied magnetic field. Then, the samples reach a maximum, after which the magnetization decreases, indicating that there is sufficient thermal energy to randomly disorganize the magnetic moments, akin to paramagnetic materials. The temperature at which this occurs is referred to as the blocking temperature, T_B. For the Fe$_{1.5}$Co@C sample, the T_B value was 55.2 K, corroborating the narrow hysteresis curves at room temperature. An ideal superparamagnetic material should have its ZFC and FC curves overlapping at T_B (LI, Xinyuan *et al.*, 2020). However, the Fe$_{1.5}$Co@C sample showed this overlap at a much higher temperature, 218.6 K, possibly due to a wide particle size distribution. As this sample is cooled from 300 to 5 K under the same magnetic field, 10 mT, the magnetic moment significantly increases, suggesting the presence of weak dipolar magnetic interactions in the sample (AMSARAJAN; JAGIRDAR, 2020; ANSARI *et al.*, 2019).

Figure 14 – ZFC and FC magnetization curves of the Fe$_{1.5}$Co@C sample.
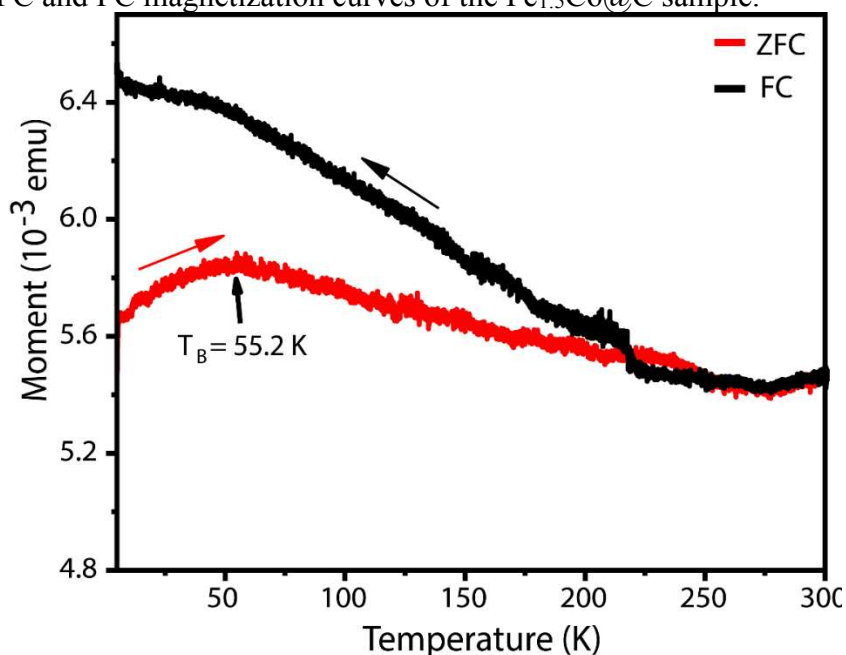
Source: the author.

2.3.7 XPS

The XPS analysis was conducted to analyze the surface composition and the oxidation states of Fe and Co on the Fe$_2$Co@C nanoparticles. The survey spectra and deconvoluted peaks for Fe, Co, O and C are presented in Fig. 15. The Fe 2p peak was split into

six peaks, at 706.57, 710.23, 712.32, 718.13, 724.13, and 732.63 eV, corresponding to Fe^0, Fe^{2+}, Fe^{3+} and three satellite peaks, respectively (AN *et al.*, 2018). The Co 2p binding energies were 777.53, 780.68, 782.71, 786.37, 796.39, and 802.85 eV, assigned to Co^0, Co^{3+}, Co^{2+}, and three satellite peaks, respectively (PARK *et al.*, 2020). The three peaks at 529.66, 531.58, and 533.39 eV are related to O^{2-}, OH^-, and O-C=O, respectively (PARK *et al.*, 2020).

Figure 15 – XPS spectra of Fe₂Co@C nanoparticles: survey (a) and deconvoluted peaks showing the surface composition and oxidation states of Fe 2p (a); Co 2p (b); O 1s (c); and C 1s (d).
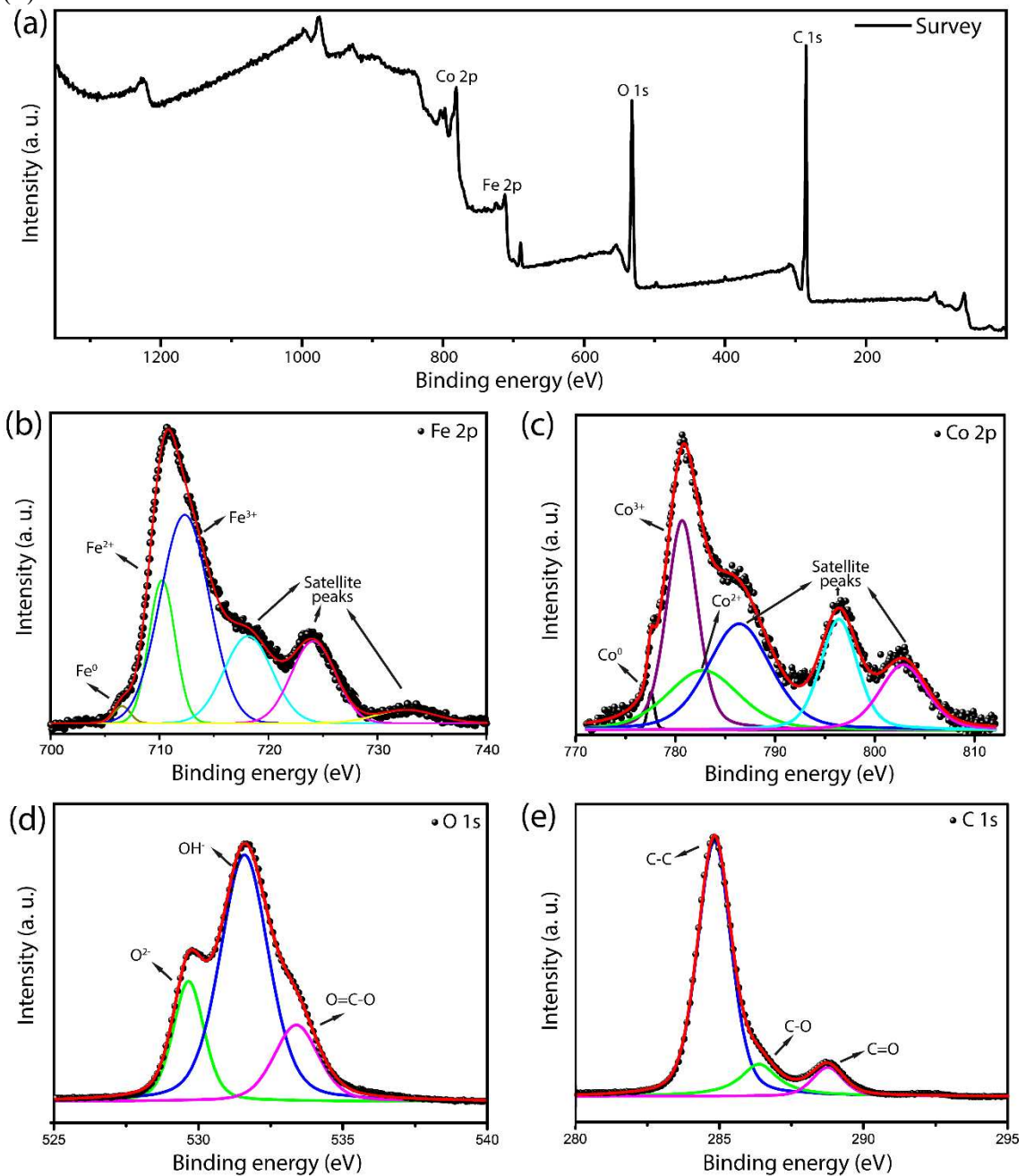
Source: the author.

These XPS results indicate that the surface of the FeCo nanoparticles is partially oxidized, likely formed through a passivation process leading to the formation of a layer of metal oxyhydroxide and hydroxide. The C 1s spectrum was deconvoluted into the main peak of C-C at 284.83 eV and two others corresponding to C-O-H at 286.36 eV and C=O 288.76 eV (CHEN, Tianju *et al.*, 2020). The C-O-H and C=O peaks support the presence of carbonyl groups, likely formed through the dehydration of hydroxyl groups from xylose, as indicated by the FTIR analysis.

2.3.8 Degradation of rhodamine B

2.3.8.1 Effect of adsorption, PMS dosage and pH on degradation reaction

In order to optimize the degradation of rhodamine B, we evaluated the effects of adsorption, pH, and PMS dosage in the reaction system. As depicted in Fig. 16 (a), there was no reduction in RhB concentration when the NPs were used in the absence of PMS. However, when PMS was added (in the absence of NPs), the RhB concentration decreased, reaching a degradation efficiency of 15.2% after 20 minutes of reaction and a degradation kinetics of $k = 8.49 \times 10^{-3}$ min^{-1}. This result highlights the absence or insignificance of the adsorption effect in the degradation study and underscores the pivotal role of Fe$_2$Co@C NPs in enhancing the production rate of reactive species for RhB degradation. The degradation of rhodamine B by PMS itself is common and occurs through the dissociation of the peroxymonosulfate molecule, even at low rates (ZHU *et al.*, 2019). This process is slightly intensified by adjusting the initial pH to 7.0, which in turn slightly increases the activation rate (WACŁAWEK, Stanisław *et al.*, 2022).

Fig. 16 (b) illustrates the decrease in rhodamine B concentration over time for various PMS concentrations. Remarkably, a PMS concentration higher than 2.0 mM was adequate to remove over 99% of the dye in just 12 minutes of reaction, with a degradation kinetics of $k = 3.61 \times 10^{-1}$ min^{-1}. Although a 2.5 mM PMS concentration initially accelerated degradation slightly, over the experimental time frame, and with very similar degradation kinetics of $k = 4.45 \times 10^{-1}$ min^{-1}, the 2.0 mM PMS concentration achieved a comparable degree of removal and was thus selected for further investigations. Even after 20 minutes of reaction, PMS concentrations of 1.0 and 1.5 mM were insufficient to completely eliminate the dye, resulting in removal efficiencies of 76.1% and 95.4%, respectively.

Figure 16 – Comparative study of the addition of NPs alone, PMS alone and the combination of both at pH 7.0 and [PMS] = 2.0 mM (a), and effects of PMS dosage with no control of pH (b) and initial pH with [PMS] = 2.0 mM (c) in the degradation of RhB at 25°C; (d) variation of PMS concentration over time. The rate constants shown in this figure were obtained by linear interpolation on the graph of $\ln(C/C_0)$ versus time, following pseudo-first order kinetics (see Fig. A1).
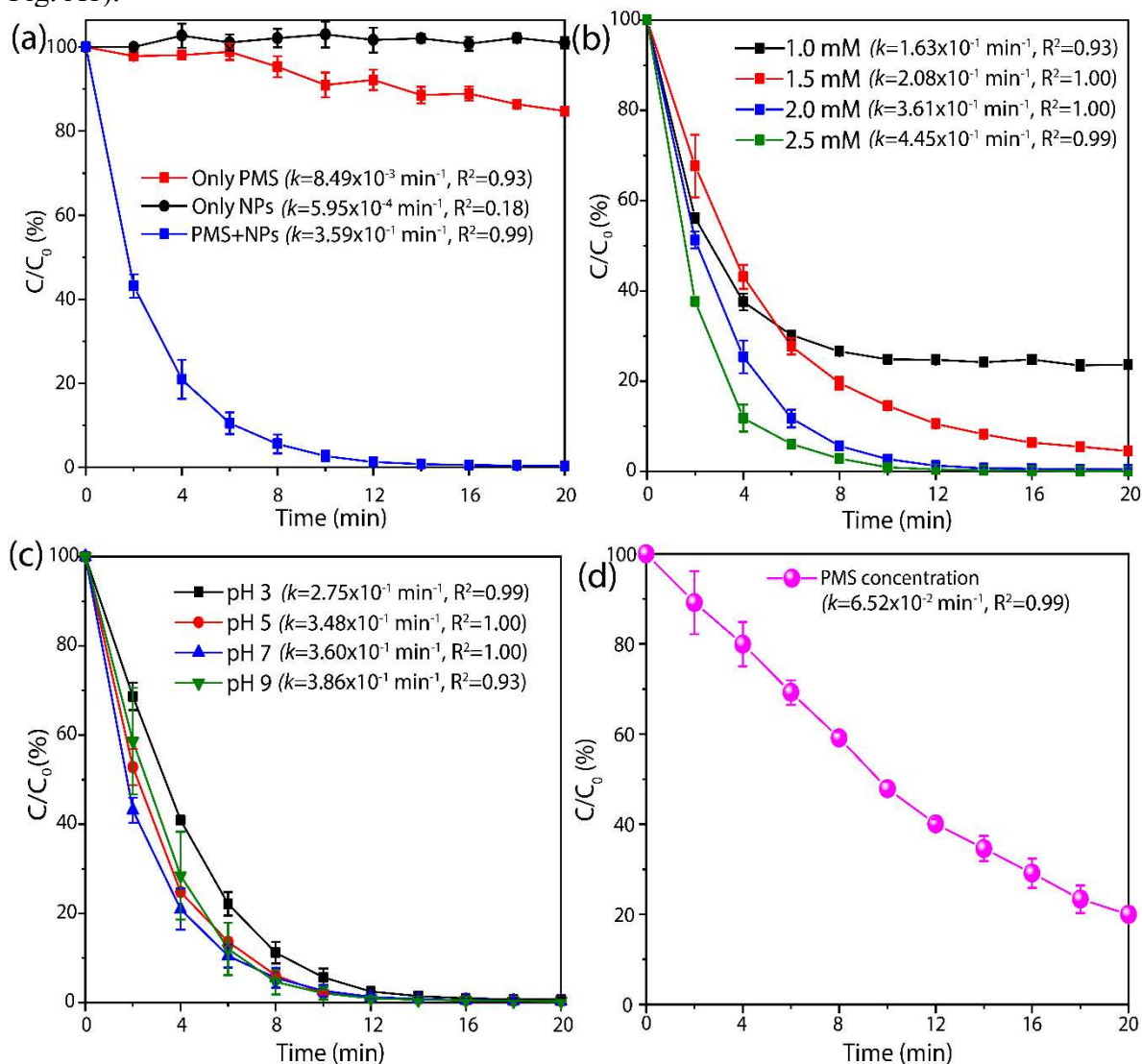
Source: the author.

By increasing the concentration of the oxidant, the efficiency of dye removal increased, as a greater number of PMS molecules could interact with the catalyst surface and be activated, forming more radical species (XU *et al.*, 2019). However, as the concentration increases, the catalyst surface becomes saturated, and substantial increases in performance are no longer observed. Furthermore, a high concentration of radicals enhances the scavenging effect through radical recombination, thereby suppressing the oxidizing capacity of the reactional system (GHANBARI; MORADI, 2017).

The effect of pH on PMS-based AOPs is closely associated with the protonation state of the PMS anion. Generally, at pH values below 9.4, the HSO_5^- form dominates, which has a stronger oxidizing capacity, while pH values above 11 promote alkaline activation of PMS, forming singlet oxygen and superoxide anion radicals (GHANBARI; MORADI, 2017; ZHOU; ZHANG; HU, 2020).

Surprisingly, pH had little effect on rhodamine B removal efficiency after 20 minutes of the reaction, even after 12 min (Fig. 16 (c)), as the degradation kinetics remained between $k = 2.75 \times 10^{-1}$ min^{-1} and $k = 3.86 \times 10^{-1}$ min^{-1}, approximately. However, increasing the pH up to 7 led to a slight increase in the initial reaction rate, followed by a reduction at pH 9, as supported by the degradation kinetic at these pH levels. The lower reaction rate at an alkaline medium is related to the formation of $^{\bullet}OH$ radicals, which have a shorter lifespan and a lower reduction potential (1.8 V) than sulfate radicals (XIAO $et\ al.$, 2020). In addition, alkaline pH levels hinder homogeneous catalysis by metal ions in the solution due to their reduced solubility. The slightly slower reaction at pH 3 might be associated with the stabilizing effect of H^+ on HSO_5^- ions, which inhibits the interaction between PMS and the FeCo@C nanoparticles (FAN, Yanan $et\ al.$, 2017; GONG, Cheng $et\ al.$, 2017; ZHANG, Tao; ZHU; CROUÉ, 2013).

It is also worth mentioning that the investigated effect pertains to the initial pH and it decreases after the addition of PMS, especially in large quantities, as indicated by reactions 20-22 (GHANBARI; MORADI, 2017):

$$HSO_5^- \rightarrow SO_5^{2-} + H^+ \tag{20}$$

$$HSO_5^- + e^- \rightarrow SO_4^{\bullet-} + OH^- \tag{21}$$

$$SO_4^{\bullet-} + H_2O \rightarrow {}^{\bullet}OH + SO_4^{2-} + H^+ \tag{22}$$

While it would be possible to maintain a constant pH throughout the reaction by using buffers, such strategy would entail the addition of interfering ions known to hinder the oxidation process (WAN $et\ al.$, 2022).

Following a series of optimizing experiments, the total organic carbon (TOC) was determined before and after the degradation process under the optimized conditions to investigate the mineralization efficiency. After 20 minutes of reaction, the TOC removal efficiency was 89.0±0.6%. This percentage of mineralization was excellent, albeit slightly below the degradation value (99.66±0.03%), monitored by the absorbance of the solution. During the degradation process, the dye molecules continuously break down into smaller

molecules until they are fully mineralized. The difference can be attributed to the portion of the dye that has not been entirely converted into inorganic carbon but does not exhibit absorbance in the visible spectrum.

The catalyst used in this work has shown great promise for the mineralization of organic pollutants. Many previous works lack results regarding mineralization. Therefore, degradation efficiency was used for comparison with previous studies, as shown in Table 4. This work stands out for its high efficiency, short reaction time, and minimal catalyst usage. It is worth noting that some cases of degradation with very poor mineralization capacity exist, as reported by Du et al. (2016) (only 12.4%) (DU *et al.*, 2016). In this work, the TOC removal efficiency demonstrates a high conversion yield with reduced generation of potentially polluting intermediates.

Table 4 – Performances comparison of recently reported Fe-Co based catalysts for RhB degradation using PMS.

Catalyst	Dosage (g/L)	PMS (mM)	RhB (mg/L)	Efficiency (%)	Time (min)	Ref.
CoFe$_2$O$_4$/TNTs	0.20	13	100	97.0	30	(DU *et al.*, 2016)
CoFe$_2$O$_4$/Ag-fMWCNTs	0.2	3.2	20	100	14	(ABDEL-SALAM; YOON, 2022)
C@Co$_3$O$_4$-Q5	0.2	1	100	50.0	20	(LIANG; FU, 2021)
CoFe$_2$O$_4$	0.3	7	20	100	90	(LIU *et al.*, 2022)
Co-HAP	200	0.4	40	93.3	12	(PANG *et al.*, 2020)
NiCo$_2$O$_4$ nanoflakes	0.2	0.5	24	95	20	(ZHANG, Wenwen *et al.*, 2016)
M-Co$_{1+x}$Fe$_{2-x}$O4	0.2	0.65	40	97.9	20	(ZHAO, Jujiao *et al.*, 2021)
Fe$_3$O$_4$/CoFeCu-LDHs	0.2	1	50	100	20	(LI, Tong *et al.*, 2021)
CoFe$_2$O$_4$/OMC	0.05	1.5	100	100	60	(DENG *et al.*, 2017)
Fe$_2$Co@C	0.05	2	100	99.7	20	This work

Source: the author.

The degradation of rhodamine B is directly linked to the conversion of PMS into reactive species. Since quantifying the concentration of these species during the reaction is challenging, one way to track the activation of PMS is to monitor its concentration over time, as shown in Fig. 16d. Within 20 minutes, approximately 20% of the PMS concentration remains in the solution. However, this level drops rapidly upon activation. After 25 min (data not shown), the concentration was only 12 ± 2 % ($2.4 \pm 0.4 \cdot 10^{-4}$ mol L^{-1}).

2.3.8.2 Reaction quenching studies and reusability of Fe₂Co@C

To gain further insight into the degradation mechanism, additional experiments were conducted by adding specific radical scavengers. Fig. 17 (a) displays the degradation kinetics of rhodamine B under the influence of different scavenger agents: methanol (Met-OH), tert-butyl alcohol (TBA) and L-histidine (L-hyst). Methanol molecules can scavenge both $^\bullet$OH and $SO_4^{\bullet-}$ radicals. On the other hand, tert-butyl alcohol, due to steric effects associated with methyl groups, better attaches to hydroxyl radicals, being 1000-fold more reactive compared to sulfate radicals (GONG, Cheng *et al.*, 2017).

Figure 17 – (a) Effect of different scavengers, TBA (200 mM), Met-OH (2 M), L-hyst (15 mM) in the RhB degradation under optimized conditions; (b) performance of the Fe₂Co@C catalyst for each cycle of use. The rate constants shown in this figure were obtained by linear interpolation on the graph of ln(C/C0) versus time, following pseudo-first order kinetics (see Fig. A2).
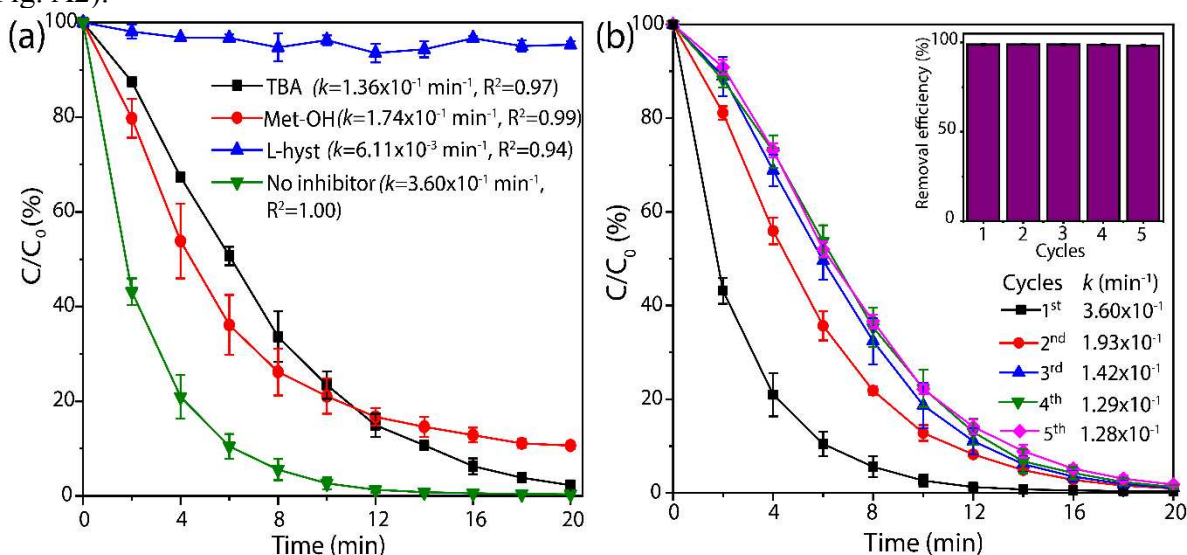
Source: the author.

As observed in Fig. 17 (a), TBA and Met-OH slowed down the reaction rate, suggesting the involvement of $SO_4^{\bullet-}$ and $^\bullet$OH species in the RhB degradation. However, these scavengers had almost no effect on the removal efficiency of RhB at 20 minutes of reaction, indicating that the oxidation process also proceeds via another mechanism. Using the endpoint of 20 minutes for comparison, inhibition with methanol was slightly more effective than with TBA, leading us to assume that sulfate radicals are predominant among the radical species. Although the constant calculated for the first 8 minutes is higher for Met-OH, there is a slight curvature in the graph of ln(C/C0) versus time in Fig. A2, with the Met-OH curve intersecting that of TBA at 12 minutes.

Given the weak impact of $^\bullet$OH and $SO_4^{\bullet-}$ radical scavengers in the oxidation process, it was postulated that non-radical reactive oxygen species played a more significant role in RhB degradation. Therefore, singlet oxygen ($^1O_2$), known for its high reactivity towards unsaturated carbons and negligible reactivity towards alcohols, was suspected to be present in the FeCo/PMS system (RAO *et al.*, 2020). To confirm this hypothesis, L-histidine was employed as a $^1O_2$ probe. As shown in Fig. 17, there was a substantial inhibition of the reaction upon the addition of L-histidine, resulting in a dye removal of only 4.67%, with a degradation kinetics of k=6.11x10^{-3} min^{-1}. Hence, the oxidation of RhB mainly occurs via a non-radical pathway, with $^1O_2$ being the primary reactive species, while $^\bullet$OH, and $SO_4^{\bullet-}$ are less prevalent. Similar results were obtained in the degradation of methyl orange, using PMS/FeCo-MCM41 (SUN *et al.*, 2020), and in the degradation of bisphenol AF, using PMS/BiFeO$_3$ (WANG *et al.*, 2020). In this study, hydrochar is presumed to play a crucial role, contributing significantly to the predominance of the mechanism involving singlet oxygen.

Based on the aforementioned results and the literature (DING *et al.*, 2021; LI, Xiaowan *et al.*, 2019; SUN *et al.*, 2020), a hybrid degradation mechanism can be proposed, as outlined in reactions 18-25. Initially, PMS (HSO$_5^-$) adsorbs onto the activated catalyst surface and is subsequently cleaved to generate $SO_4^{\bullet-}$ radicals (18-19), which can also react with water to produce $^\bullet$OH (20). PMS also reacts with the Fe^{3+} and Co^{3+} ions generated in previous steps, restoring the catalyst and producing $SO_5^{\bullet-}$ radicals (23-30). These radicals either combine to form persulfate and singlet oxygen (28) or react with water, generating $^1O_2$ and hydrogen sulfate (HSO$_4^{2-}$) ions (29).

$$\equiv Co^{2+} + HSO_5^- \rightarrow \ \equiv Co^{3+} + SO_4^{\bullet-} + OH^- \tag{23}$$

$$\equiv Fe^{2+} + HSO_5^- \rightarrow \ \equiv Fe^{3+} + SO_4^{\bullet-} + OH^- \tag{24}$$

$$SO_4^{\bullet-} + H_2O \rightarrow SO_4^{2-} + \ ^\bullet OH \tag{25}$$

$$\equiv Co^{3+} + HSO_5^- \rightarrow \ \equiv Co^{2+} + SO_5^{\bullet-} + H^+ \tag{26}$$

$$\equiv Fe^{3+} + HSO_5^- \rightarrow \ \equiv Fe^{2+} + SO_5^{\bullet-} + H^+ \tag{27}$$

$$SO_5^{\bullet-} + SO_5^{\bullet-} \rightarrow S_2O_8^{2-} + \ ^1O_2 \tag{28}$$

$$4\ SO_5^{\bullet-} + 2\ H_2O \rightarrow 4\ HSO_4^{2-} + 3\ ^1O_2 \tag{29}$$

$$^1O_2/\ SO_4^{\bullet-}/^\bullet OH + RhB \rightarrow intermediates \rightarrow CO_2 + H_2O \tag{30}$$
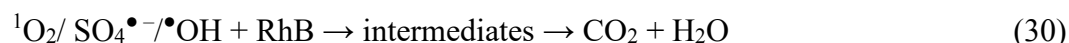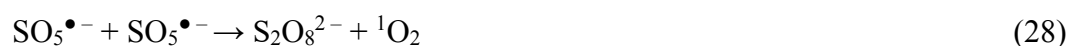
To assess the reusability of the catalyst, Fe$_2$Co@C nanoparticles were recovered after each reaction and reused in the RhB degradation. The experiments were repeated up to five cycles (inset of Fig. 17 (b)), and the catalyst's performance remained consistent for five consecutive uses. By the fourth cycle, the removal efficiency exceeded 99%, while 98% was

observed in the fifth cycle. However, as depicted in Fig. 17, the initial rate of the degradation reaction decreased with each reuse. This decline was expected, as the catalyst can be negatively influenced by an intermediate product of the reaction. Additionally, a portion of Fe^{2+} and Co^{2+} ions on the nanoparticle surface is oxidized and leached out (approximately 0.8 ± 0.3 and 4.0 ± 0.5 mg/L of the Fe^{2+} and Co^{2+} ions, respectively). The sharp decline in the degradation curves indicates a trend toward homogeneous catalysis, which weakens with successive reuses. To investigate whether homogeneous catalysis contributes to the process, experiments were conducted by adding metals at the concentration levels at which they are leached. As demonstrated in Fig. 18, the kinetics catalyzed by the nanoparticles were very similar to those observed when the supernatant of the reaction was used to prepare a new dye solution. However, when only the metals ions (at the concentrations at which they are leached) were added, the kinetics displayed some variation, becoming somewhat slower. It is hypothesized that the supernatant, which contains traces of PMS and other impurities, accelerates the process. Thus, homogeneous catalysis plays a significant role, but the process is not purely homogeneous.

Figure 18 – Comparison of the kinetics of RhB degradation using the catalyst (blue line), the supernatant collected after 20 min of reaction containing the leached metals (red line), and Co(II) and Fe(II) at the concentrations at which they leached in the first use of the NPs (gray line).
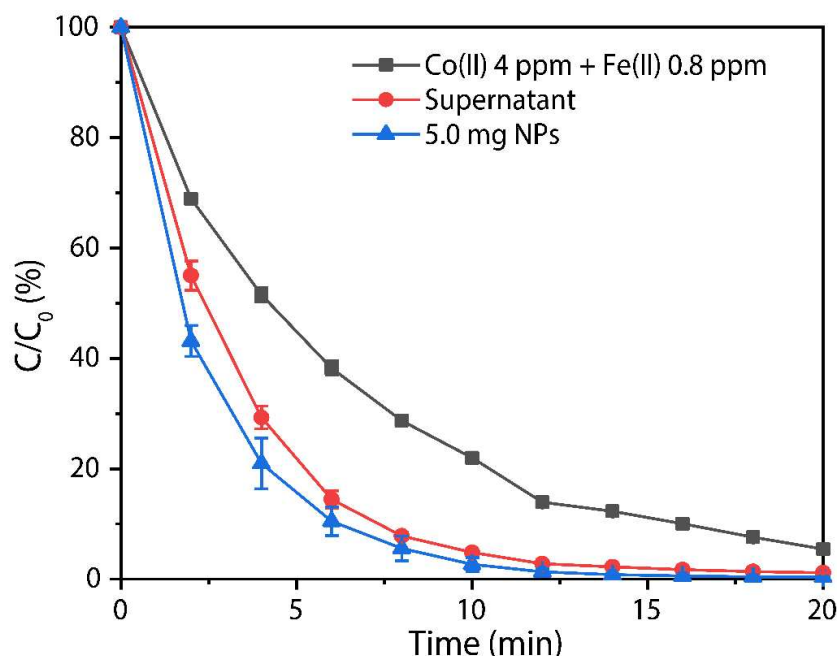
Source: the author.

The stability of the catalyst was also assessed through SEM and VSM analysis, as presented in Figs. 19 and 20, respectively. Prior to its initial use, the catalyst exhibited zones of

high iron concentration. This concentration increased after the first use due to the loss of a portion of the carbonaceous material in an oxidative environment. The Fe/O ratio rose due to the loss of part of the passivating oxide layer. Subsequently, after the fifth use, the catalyst displayed a higher concentration of cobalt on its surface. Notably, the material's surface became more porous, markedly differing from its initial appearance. However, according to the VSM results (Fig. 20), only a slight difference was observed in the Ms values for the catalyst between the beginning and after the fifth cycle.

Figure 19 – SEM images of the Fe2Co@C catalyst before using (a) and after the 1st (c) and the 5th (e) cycles of use under optimized conditions. EDS mapping is shown in insets in the images (a), (c) and (e), while their respective spectrum is given in (b), (d) and (f).
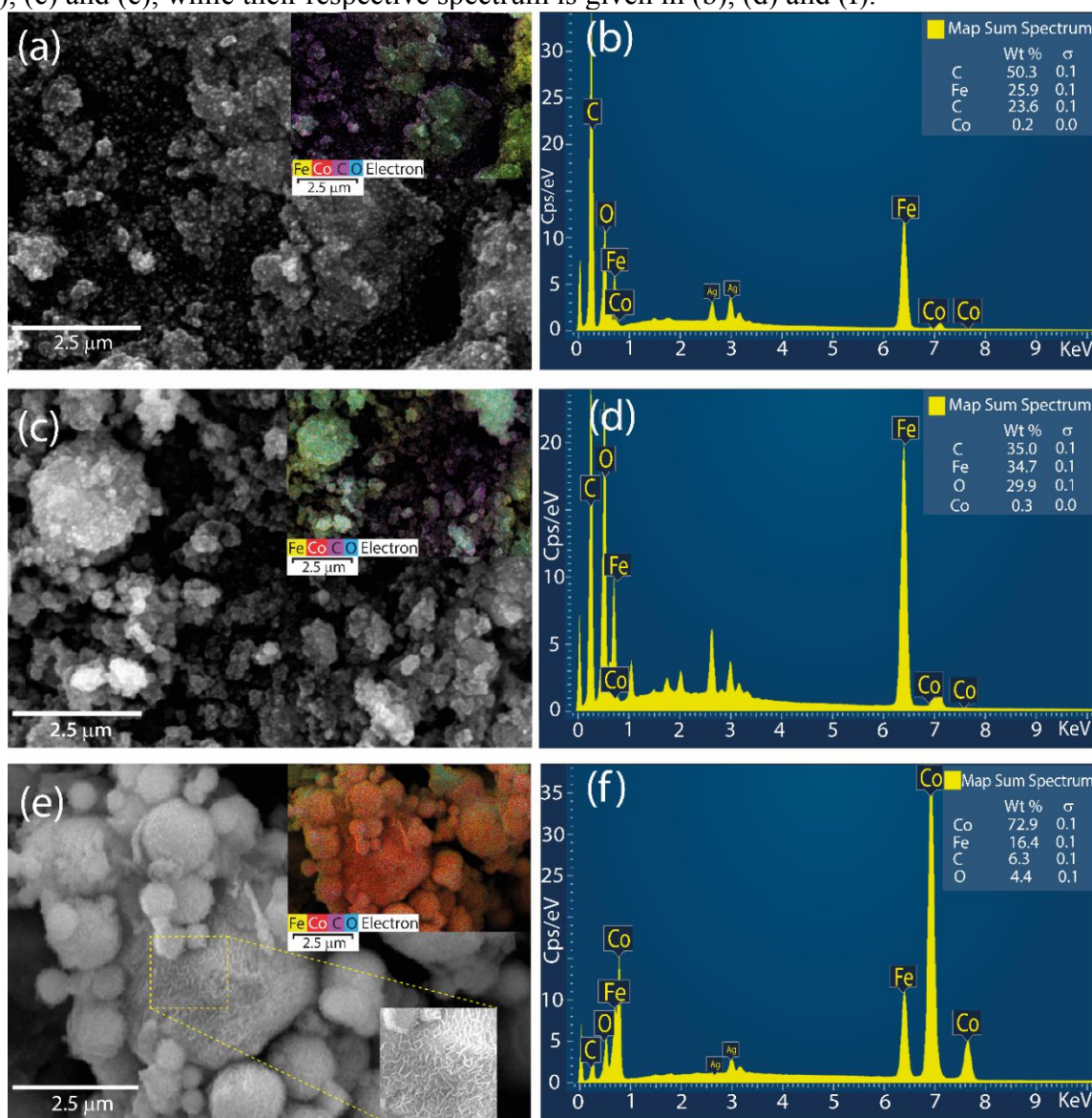
Source: the author.

Figure 20 – Magnetization curves for the Fe2Co@C catalyst before using (blue) and after the 5th cycles of use (red) under optimized conditions.
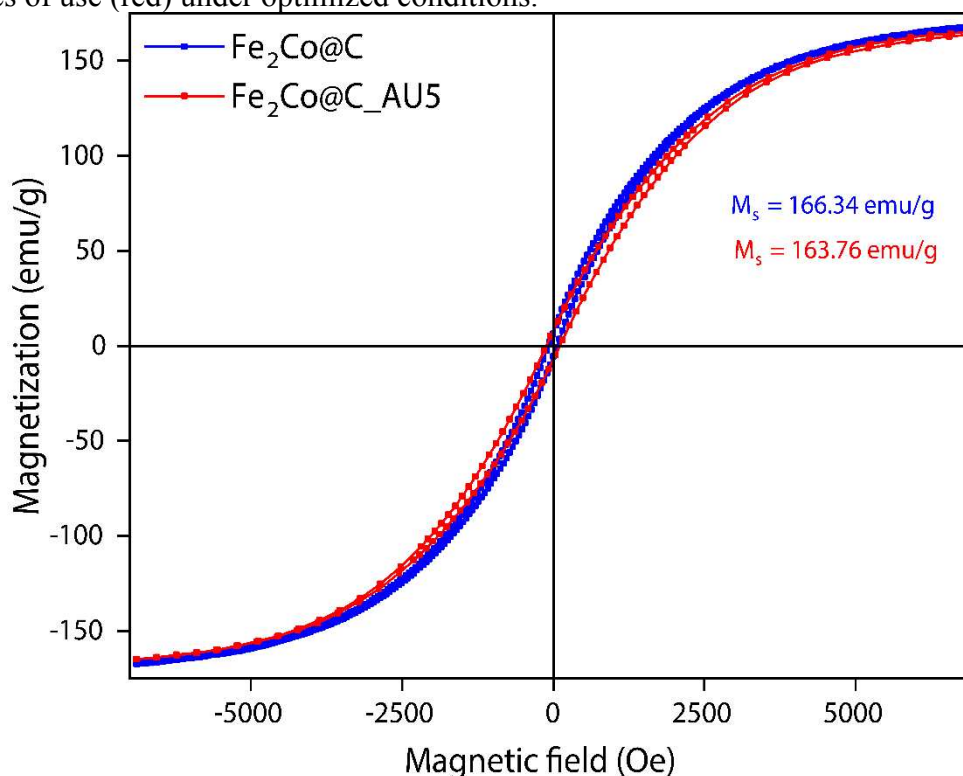
Source: the author.

2.4 Conclusions

FeCo nanoparticles were synthesized using the polyol method, resulting in a combination of secondary phases of Co hcp and Co fcc. The higher the iron proportion in the precursor solution, the greater the yield of the FeCo phase, the formation of a carbon capping on the nanoparticles, and the saturation magnetization of the material. The optimal synthesis conditions were achieved with [OH-] / [Metal] = 26 and [Fe] / [Co] = 2, producing spherical agglomerates of particles with varying sizes.

The most efficient catalysis for degrading 100 ppm RhB was observed when using 5.0 mg of catalyst, 2 mM PMS, pH 7.0, and a reaction time of 20 minutes. Interestingly, the pH parameter had minimal impact on the efficiency of dye removal. Radical scavenging studies revealed that singlet oxygen was the predominant species in the AOP, with sulfate and hydroxyl radicals also contributing to the RhB oxidation.

The catalyst demonstrated consistent performance in removing RhB, achieving at least 98% removal in up to 5 consecutive uses. Notably, there was a significant level of metal

leaching ($[Fe^{2+}] = 0.8\pm0.3$ mg/L and $[Co^{2+}] = 4.0\pm0.5$ mg/L), and further research is needed to develop strategies for preventing this metal leaching during the oxidation process.

3 CHAPTER 3 – L-CYSTEINE-COATED MAGNETITE NANOPARTICLES AS A NEW PLATFORM FOR ENZYMES IMMOBILIZATION: AMPLIFYING BIOCATALYTIC ACTIVITY FOR INDUSTRIAL APPLICATIONS

This study presents the synthesis of magnetite nanoparticles coated with L-cysteine (Fe_3O_4@LC) and their subsequent utilization as a support matrix for the immobilization of *Candida antarctica* Lipase A (CALA). The immobilization process involved physical interactions and covalent bonding mediated by glutaraldehyde. Comprehensive characterization was conducted using techniques including X-ray diffraction (XRD), transmission electron microscopy (TEM), scanning electron microscopy (SEM), Fourier-transform infrared spectroscopy (FTIR), X-ray photoelectron spectroscopy (XPS), and vibrating sample magnetometry (VSM), providing compelling evidence of a successful synthesis. Under optimized conditions, employing 1 mg of protein per gram of support, pH 7 in a 25 mM phosphate buffer, and a 5-hour reaction at 25 °C, immobilization on glutaraldehyde-activated support achieved an impressive yield of 85.0% ± 2.6, accompanied by a specific activity of 212.5 ± 1.3 U/g, outperforming the physical adsorption approach. Remarkably, the immobilized enzyme exhibited higher activity than the free enzyme at alkaline and acidic pH levels. Furthermore, thermal and pH inactivation studies revealed that the biocatalyst's half-life exceeded that of free CALA by more than 8 times at pH 10. These results underscore the potential of the Fe_3O_4@LC-GLU-CALA system as a robust biocatalytic matrix with promising applications in biodiesel production, ester synthesis, and pharmaceutical manufacturing.

3.1 Introduction

Enzymes, biological catalysts primarily comprised of specialized globular proteins, stand out for their remarkable specificity and efficiency, capable of accelerating reactions by up to 10^{26} times their natural rate (QUINN; SIKORSKI, 2014). Due to these attributes and their environmentally friendly appeal, enzymes have garnered substantial interest in industrial and biotechnological applications, leading to significant energy and chemical savings (JEGANNATHAN; NIELSEN, 2013; KOŁODZIEJCZAK-RADZIMSKA; JESIONOWSKI, 2020). Among enzymes, lipases (triacylglycerol acyl hydrolases) occupy a prominent position, finding particular relevance in the hydrolysis of oils and fats (their natural substrates) as well as in the synthesis of ester bonds in various substrates (transesterification, aminolysis, alcoholysis, and acidolysis), thanks to their broad substrate specificity and high enantioselectivity and regioselectivity (ALEJALDRE *et al.*, 2023; CHANDRA *et al.*, 2020; MONTEIRO, R.R.C. Rodolpho R.C. *et al.*, 2022).

Lipases derived from the basidiomycete Candida antarctica, specifically Lipase A (CALA) and Lipase B (CALB), have attracted considerable attention in biocatalysis. CALB has established itself in organic synthesis and is commercially available as Novozym® 435. CALA, although explored more recently, has demonstrated tremendous potential due to its high thermal tolerance (up to 100 °C), solvent resistance, kinetic resolution capacity of sterically hindered tertiary alcohols, high specificity for medium-chain fatty acids (C6-C12), promiscuity towards alcohols and amines, and selectivity for esters of trans fatty acids (ALEJALDRE *et al.*, 2023; MONTEIRO, Rodolpho R.C. *et al.*, 2020).

However, successfully utilizing CALA often requires immobilization to enhance its thermal and solvent stability, reusability, and ease of separation from reaction mixtures. Various strategies have been employed for this purpose, including confinement or encapsulation in polymeric matrices, adsorption or covalent binding to insoluble supports, and the formation of cross-linked enzyme aggregates (CLEAs) (CHANDRA *et al.*, 2020). Among these approaches, the adsorption and covalent binding onto magnetic nanoparticles show promise due to their high surface area, superparamagnetism, and ease of separation under external magnetic fields (FAN, Hong Lei *et al.*, 2016; XIE; HUANG, 2018). Additionally, the improved dispersion of the nanoparticle-anchored enzyme in the reaction medium addresses common substrate diffusion issues encountered with CLEAs (MONTEIRO, Rodolpho R.C. *et al.*, 2020).

Magnetite is one of the most used magnetic supports for enzyme immobilization due to its ease of acquisition and low cost. However, magnetite is easily oxidized due to Fe^{2+}

presence in its structure, leading to a loss of magnetization and dispersibility (MONTEIRO, Rodolpho R. C. *et al.*, 2019). Thus, to improve their oxidation resistance, magnetite can be modified with various molecules, including chitosan (MONTEIRO, Rodolpho R. C. *et al.*, 2019), 3-amino-propyltriethoxysilane (MOREIRA *et al.*, 2020), graphene oxide (XIE; HUANG, 2018), polyethyleneimine (BEZERRA *et al.*, 2017), and amino acids (BEZBRADICA; MATEO; GUISAN, 2014; SCHWAMINGER *et al.*, 2015). In addition, these molecules also enhanced the interaction between the magnetic nanoparticles and enzymes. Amino acids offer certain advantages due to their zwitterionic nature, resembling enzymes, as they are electrically neutral while stabilizing the support through carboxylate and amino groups (CHEN, Ning *et al.*, 2019). These groups also react with acids and bases, and their hydrophilicity keeps the enzyme microenvironment moist and less susceptible to pH changes, preserving the native structure of the lipase (CHEN, Ning *et al.*, 2019).

Among amino acids, cysteine stands out due to its unique thiol group, which can guide anchoring through thiol-thiol interaction with particular regions of the lipase, considering the low quantity of this amino acid on its surface (GRAZÚ *et al.*, 2005; ZAHIRINEJAD *et al.*, 2021). Furthermore, supports coated with cysteine are already noted in the literature for enhancing enzyme activity and/or stability compared to their free forms (CHEN, Ning *et al.*, 2019; GRAZÚ *et al.*, 2005; KOŁODZIEJCZAK-RADZIMSKA; JESIONOWSKI, 2020; MUTHUKUMAR *et al.*, 2020).

Accordingly, this study focuses on the immobilization of Lipase A from *Candida Antarctica* onto L-cysteine-coated magnetic nanoparticles (Fe_3O_4@LC) as a novel biocatalytic system. The immobilization process, known for its efficiency and ease of recovery, holds significant potential for biotechnological applications, including biodiesel production (MOREIRA *et al.*, 2020), ester synthesis (JIANG *et al.*, 2019), and pharmaceutical manufacturing (BEZERRA *et al.*, 2017).

This article aims to provide a comprehensive overview of the immobilization methodology, characterization of the resulting biocatalyst, and its catalytic performance compared to free CAL-A. Furthermore, insights into the structural and kinetic aspects of the immobilized lipase will be explored. The findings presented here contribute to the growing body of knowledge on enzyme immobilization and pave the way for implementing Fe_3O_4@LC nanoparticles as a versatile support matrix for lipase biocatalysis. This is due to their ease of recovery from the reaction medium and rapid synthesis process based on low-cost and readily available precursors.

3.2 Materials and Methods
3.2.1 Materials

The commercial extract of lipase A from *Candida antartica* (CALA, 20.88 mg/mL) was obtained from Novozymes (Madrid, Spain). Ferric chloride hexahydrate ($FeCl_3 \cdot 6H_2O$), 25% (v/v) aqueous solution of glutaraldehyde, *p*-nitrophenyl butyrate (*p*-NPB) and Triton X-100 were supplied by Sigma-Aldrich (St. Louis – USA). Ferrous sulphate heptahydrate ($FeSO_4 \cdot 7H_2O$) was purchased from Dinâmica Química Contemporânea Ltda (São Paulo – Brazil). Ammonium hydroxide was purchased from Synth (São Paulo – Brazil). L-cysteine was purchased from Êxodo científica (São Paulo - Brazil). All other reagents and solvents used are of analytical grade.

3.2.2 Synthesis of Iron Magnetic Nanoparticles (Fe₃O₄) Functionalized with L-Cysteine (LC)

The L-cysteine-coated Fe_3O_4 NPs were synthesized by a three-step method based on ultrasound-assisted co-precipitation, as shown in Fig. 21a (ANDRADE NETO *et al.*, 2017). Firstly, 4 mmol of $FeSO_4 \cdot 7H_2O$ and 7.0 mmol of $FeCl_3 \cdot 6H_2O$ were dissolved in 15 mL of deionized water, heated to 60 °C, and sonicated for 1 min, using an ultrasonic processor Sonics VCX 500 (20 kHz, 500 W) operating at 40% of power and pulse 3s on 1s off. Then, 7.0 mL of 27% w/w NH_4OH was added (0.23 mL·s^{-1}) to the solution under sonication, which was kept for 4 min. Finally, 4 mL of a 2.06 mol L^{-1} L-cysteine solution was added to the reactional medium, which was sonicated for 4 min. Then, the resultant NPs, labelled as Fe_3O_4@LC, were washed with deionized water to remove the impurities, dried, and stored under vacuum until application.

3.2.3. Activation of Fe₃O₄@LC with Glutaraldehyde (GLU)

The amino terminal groups of Fe_3O_4@LC were activated with GLU (Fe_3O_4@LC-GLU) to promote covalent bonding between the enzyme and the support, as shown in Fig. 21b. Briefly, 50 mg of previously dried Fe_3O_4@LC NPs were dispersed in 5 mL of a sodium phosphate buffer solution (PBS 25 mM, pH 7.0), and 125 μL of 25% (v/v) aqueous glutaraldehyde solution were added to this mixture, which was subsequently kept for 2 h under constant stirring at 25 °C. Then, the support Fe_3O_4@LC-GLU was washed 3 times with 5 mL of sodium phosphate buffer solution (pH 7.0 and 25 mM) to remove the excess glutaraldehyde (BEZERRA *et al.*, 2017).

Figure 21 – Schematic for the synthesis of Fe$_3$O$_4$@LC NPs (a) and their application as a support for immobilizing the CALA enzyme by physical interaction and chemical bonding (b).
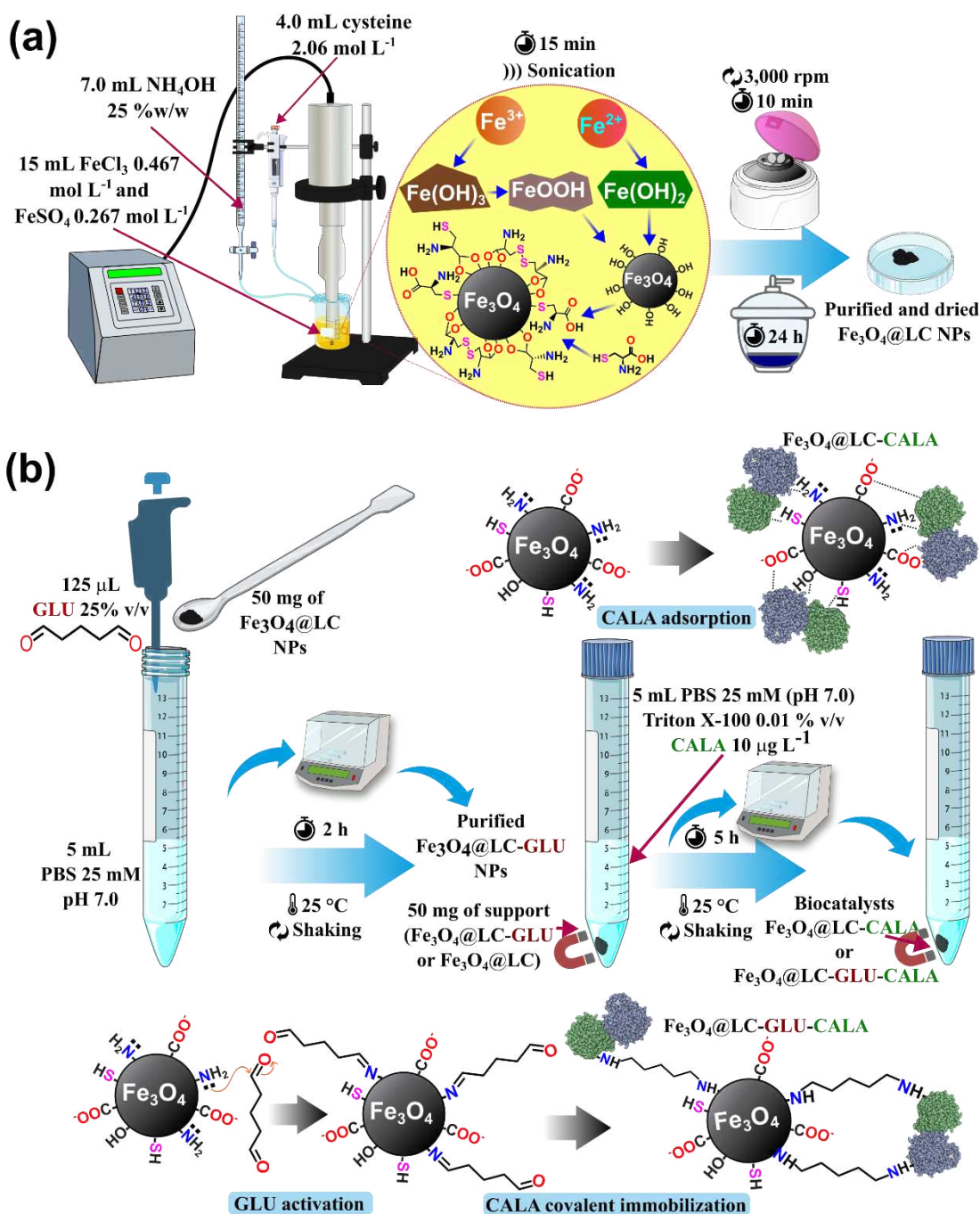
Source: the author.

3.2.4. Immobilization of CALA on Fe$_3$O$_4$@LC-GLU

50 mg of Fe$_3$O$_4$@LC-GLU were suspended in 5 mL of sodium phosphate buffer solution (PBS 25 mM, pH 7.0) containing 0.01% Triton X-100 and 10 µg L^{-1} of CALA (1 mg of protein per g of support). The system was kept under constant stirring for 5 h at 25 °C.

Additionally, a reference solution, identical to the enzyme solution, was prepared without support, which kept its activity intact during immobilization. Finally, immobilized CALA was separated from the solution by magnetic decantation and washed with 5 mL of sodium phosphate buffer solution (pH 7.0 and 25 mM) to neutrality (MONTEIRO, Rodolpho R. C. *et al.*, 2019).

3.2.5. Immobilization of CALA on Fe₃O₄@LC

CALA was immobilized on Fe_3O_4@LC by physical adsorption, as shown in Fig. 21b. For this, 50 mg of Fe_3O_4@LC were suspended in 5 mL of sodium phosphate buffer solution (pH 7.0 and 25 mM) containing CALA (1 mg of protein per g of support) in the presence of 0.01% Triton X-100. The immobilization process was similar to that described in the previous section (MONTEIRO, Rodolpho R. C. *et al.*, 2019).

3.2.6. Determination of enzymatic activity and protein concentration

The hydrolysis of p-NPB determined the activity of the soluble and immobilized CALA; the *p*-nitrophenol concentration was quantified spectrophotometrically at 348 nm. Activity measurements were performed in sodium phosphate buffer solution (25 mM and pH 7.0) under constant stirring for 1.5 min at 25 °C, from the measurement of *p*-nitrophenol released during the hydrolysis of 50 mM *p*-NPB ($\varepsilon = 10.052$ mol^{-1} cm^{-1} under these conditions). To initiate the reaction, 50 μL of suspended lipase solution was added to 50 μL of *p*-NPB and 2.5 mL of the buffer solution (MONTEIRO, Rodolpho R.C. *et al.*, 2019). An international unit of activity (U) was defined as the amount of enzyme that hydrolyses 1 μmol of *p*-NPB per minute under the conditions described above. The Bradford method measured the protein concentration, and bovine serum albumin was used as a reference (BRADFORD, 1976). All experiments were performed at least in duplicate, and the results are presented as the average of these values and the standard deviation (generally below 5%).

3.2.7 Immobilization parameters

The immobilization parameters assessed the performance of immobilization. In short, the Immobilization Yield (IY) was defined as the ratio between the enzymatic activity of the supernatant before and after a specific time (it is worth mentioning that this strategy is only

valid if the activity of the reference is maintained during the immobilization time, as it is in this study). The Theoretical Activity (At_T) was calculated using IY and the enzyme load. The Recovery Activity (At_R) was determined as the ratio between the Derivative Activity (At_D) and At_T (SILVA *et al.*, 2012).

3.2.8 pH profile

The effect of pH on soluble and immobilized CALA activity was evaluated. Briefly, CALA or Fe_3O_4@LC-GLU-CALA were suspended in 5 mL of different buffers (pH 5-10, 25 mM). The activity was measured using *p*-NPB as described previously, using buffers at pH ranging from 5 to 10 (sodium acetate, sodium phosphate or sodium carbonate). The activity was measured when the enzyme was added to the buffer after 15 min (ARANA-PEÑA; LOKHA; FERNÁNDEZ-LAFUENTE, 2019).

3.2.9 Thermal deactivation

The effect of temperature on soluble and immobilized CALA activity was evaluated. The CALA and Fe_3O_4@LC-GLU-CALA catalysts were incubated in sodium acetate buffer solution (pH 5.0 and 25mM), sodium phosphate buffer solution (pH 7.0 and 25mM) or sodium carbonate buffer solution (pH 10.0 and 25 mM) at 70 °C for 24 hours. The activity was measured periodically using *p*-NPB as described previously, and the residual activity was expressed as a percentage of the initial activity (MONTEIRO, Rodolpho R. C. *et al.*, 2019).

3.2.10 Immobilization course

The course of immobilization of CALA onto Fe_3O_4@LC-GLU was evaluated. For this purpose, 50 mg of Fe_3O_4@LC-GLU were suspended in 5 mL of sodium phosphate buffer solution (pH 7.0 and 25mM) containing CALA (enzyme loading: 1 mg of enzyme per g of support). The system was constantly stirred for 0.5-6 hours at 25 °C (MONTEIRO, R.R.C. Rodolpho R.C. *et al.*, 2022).

3.2.11 Loading capacity

50 mg of Fe$_3$O$_4$@LC-GLU were suspended in 5 mL of sodium phosphate buffer solution (pH 7.0 and 25mM) containing CALA (enzyme loading: 1, 5, 10, 15, 20 or 25 mg of enzyme per g of support). The system was kept under constant stirring for 5 hours at 25 °C (MONTEIRO, R.R.C. Rodolpho R.C. *et al.*, 2022).

3.2.12 Material characterization

To assess the crystal structure, functionalization, and interaction of the support with glutaraldehyde and CALA, X-ray diffraction (XRD) and Fourier transform infrared spectroscopy (FTIR) analyses were carried out. XRD measurements were obtained using an Xpert Pro MPD X-ray powder diffractometer with Bragg-Brentano geometry, operating at 40 kV and 30 mA with CoKα1 radiation (k = 1.78896 Å). The measurement range was from 10° to 100° with a step rate of 1°·min^{-1}. For FTIR analysis, the samples were previously dried, ground into a fine powder, mixed with KBr and compressed into pellets. Spectra were collected in the 4000-400 cm^{-1} range using a Perkin Elmer 2000 spectrophotometer. Scanning Electron Microscopy (SEM) was conducted using a Quanta 450 FEG microscope and an Energy Dispersive Detector (EDS). The electron beam was accelerated at a voltage of 20 kV in a chamber maintained at a pressure of 10 Pa. For this analysis, the samples were deposited onto a carbon tape and coated with a thin layer of gold (~ 10 nm) using a Quorum QT150 ES sputtering evaporator. The materials were also imaged using a Hitachi HT7700 Transmission Electron Microscope (TEM), with an acceleration voltage of 120 kV. Prior to imaging, the samples were dispersed in ethanol and deposited onto a carbon-coated copper grid sample holder. X-ray photoelectron spectroscopy (XPS) was performed using a ThermoFisher Scientific K-alpha$^+$ spectrometer with monochromatic Al K-α radiation calibrated to the adventitious C1s peak at 284.8 eV. A beam energy of 200 eV was used for the survey and 50 eV for high-resolution scanning spectra. The elemental analysis was conducted on a Perkin Elmer 2400 series Elemental Analyser in the CHNS mode. The number of thiol groups (-SH) on the surface of Fe$_3$O$_4$@LC nanoparticles was determined using the Ellman's reagent (colorless) (ELLMAN, 1959). This involved measuring the absorbance at 412 nm (ε = 14150 L mol^{-1} cm^{-1}), which is characteristic of the yellow reaction product, 5-mercapto-2-nitrobenzoic acid. For this purpose, 2.0 mg of dried nanoparticles were dispersed in 2.6 mL of pH 7.4 phosphate buffer and allowed to react with 400 μL of the Ellman's reagent (DTNB 5 mmol L^{-1}

+ EDTA 0.8 mmol L^{-1} in PBS buffer pH 7.4) (BRITOS *et al.*, 2019; ELLMAN, 1959). After a 5-minute incubation, the nanoparticles were separated using a magnet, and the absorbance reading was recorded.

3.3 Results and Discussion

The synthesis strategy implemented in this study involved the coprecipitation of Fe^{2+} and Fe^{3+} ions in the form of hydroxides. This process was facilitated by raising the pH by adding ammonium hydroxide (GALVÃO, Wesley S. *et al.*, 2015). These hydroxides subsequently underwent dehydration and condensation reactions, forming a mixed iron oxide comprised of both Fe^{3+} and Fe^{2+}, commonly referred to as magnetite (Fe_3O_4), as illustrated in Fig. 21.

Following the formation of the magnetic core, cysteine was introduced into the reactional medium, anchored to the surface through its metal-chelating functional groups, particularly the sulfhydryl (-SH) and carboxylate (-COO$^-$) groups. The specific binding configuration of cysteine led to three distinct functional groups on the surface of the nanoparticles.

Remarkably, the synthesis and functionalization process were completed within 9 minutes. This exceptional efficiency was made possible by employing sonochemistry, a powerful technique in which 20 kHz waves are introduced into the reaction medium. The resulting perturbations within the medium increased the frequency of collisions between the reactants, generating microbubbles. These microbubbles, upon implosion, are well-known for creating localized conditions of up to 5000 K and 1000 bar, significantly accelerating chemical reactions (BARBOSA, J.S. *et al.*, 2018; NETO *et al.*, 2021).

Furthermore, sonochemistry has been linked to improved crystallinity and dispersibility of processed materials (BARBOSA, J.S. *et al.*, 2018). The combined approach of coprecipitation, cysteine functionalization, and sonochemical synthesis demonstrates a rapid and effective method for preparing magnetite nanoparticles for diverse applications, such as in nanotechnology and biocatalysis.

3.3.1. Characterization
3.3.1.1 XRD

Fig. 22a shows the diffraction patterns of the Fe_3O_4 nanoparticles (magnetic support) and Fe_3O_4@LC-CALA biocatalyst. Both diffractograms exhibit peaks at 2θ values of 21.44, 35.30, 41.69, 50.67, 63.16, 67.50, 74.29, 85.34, 89.14 and 95.53°. These peaks correspond to the (111), (220), (311), (400), (422), (511), (440), (620), (533), and (444) planes of the inverse spinel cubic structure, space group Fd3M, of the magnetite phase (ICSD 84611). In this structural arrangement, 16 out of 32 tetrahedral sites are occupied by Fe^{3+} ions, while the remaining tetrahedral sites and the 16 octahedral sites are filled by Fe^{2+} ions (GALVÃO, Wesley S. *et al.*, 2015).

Figure 22 – XRD patterns obtained through Rietveld refinement for the Fe_3O_4 support and the Fe_3O_4@LC-CALA biocatalyst, where $I_{calc.}$ is the simulated intensity, $I_{obs.}$ is the experimentally measured intensity and Ires. is the residual intensity ($I_{obs.} - I_{calc.}$) (a); and FTIR spectra for the support materials, cysteine functionalizing agent, CALA enzyme, and the resulting biocatalysts (b).
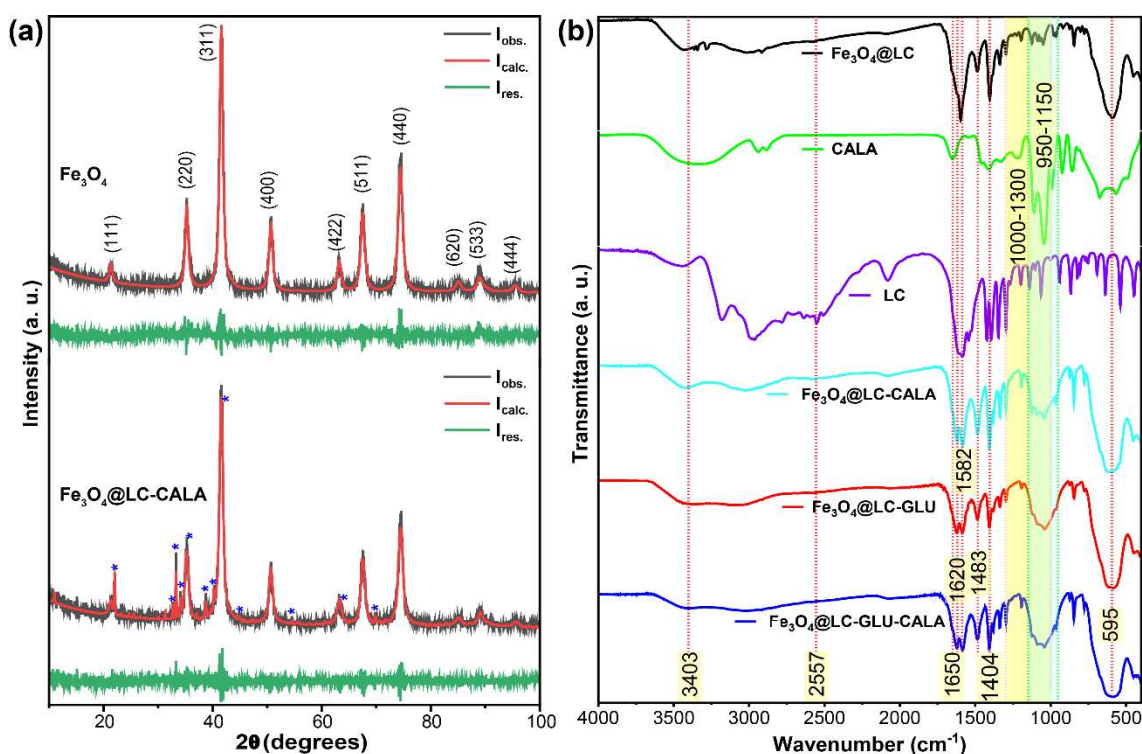
Source: the author.

Additionally, the biocatalyst shows peaks at 2θ of 22.05, 32.67, 33.28, 34.10, 35.54, 38.75, 40.30 41.98, 44.85, 54.55, 63.68 and 69.83°, which can be attributed to the hexagonal phase, space group $P6_122$, of the crystalline L-cystine phase (PDF code 00-023-1663) (SU *et al.*, 2022). Thus, it is hypothesized that a fraction of L-cysteine undergoes oxidation and dimerization through disulfide bonds, leading to L-cystine formation, likely facilitated by the

influence of heat and ultrasonic radiation (CAMPOS *et al.*, 2021; KOŁODZIEJCZAK-RADZIMSKA; JESIONOWSKI, 2020; SCHWAMINGER *et al.*, 2015).

For a detailed analysis of the diffractograms, Rietveld refinement was conducted. The parameters, such as the percentage of errors (weighted profile parameter, R_{WP}) and the goodness of fit (χ^2), are presented in Table 5, indicating a strong agreement between the experimental data and the reference standards. Interestingly, the average crystallite size (L_C), calculated by using Scherer's equation, was slightly smaller for the Fe_3O_4@LC-CALA sample (12.08 ±0.98 nm) (BAGBI *et al.*, 2017). This observation aligns with previous reports in the literature, where the introduction of a functionalizing agent in the nanoparticle synthesis reaction resulted in similar behavior (ANDRADE NETO *et al.*, 2017). The thiol groups of cysteine, known for their metal-binding solid capabilities, likely hindered the crystal growth of Fe_3O_4 nanoparticles during the third step of the synthesis, wherein they became covered.

Table 5 – Structural parameters of Fe_3O_4@LC-CALA and Fe_3O_4 NPs obtained through Rietveld refinement.

Sample	Phase	Weight fraction (%)	Lattice parameters	R_{WP} (%)	χ^2	L_C (nm)
Fe_3O_4	Fe_3O_4	100	a = b = c = 8.3794 Å α = β = γ = 90°	17.41	0.9024	12.53±1.31
Fe_3O_4@LC-CALA	Fe_3O_4	78.18	a = b = c = 8.3695 Å α = β = γ = 90°	18.62	0.9249	12.08 ±0.98
	L-cystine	21.82	a = b = 5.4274 Å c = 56.3769 Å α = β = 90° γ = 120°			46.28±17.15

Source: the author.

3.3.1.2 FTIR

Fig. 22b shows the FTIR spectra for the Fe_3O_4@LC nanoparticles, cysteine, CALA, and the materials obtained during the biocatalysts design. A band at 595 cm^{-1}, corresponding to stretching vibrations of Fe-O bonds in tetrahedral sites in all samples containing magnetite corroborates their formation (BASHIR *et al.*, 2021; TODERASCU *et al.*, 2023). The band at 3403 cm^{-1}, along with a shoulder at 1650 cm^{-1}, suggests overlapping contributions from O-H and N-H stretching vibrations and water bending vibrations due to the presence of slight moisture in the samples (BAGBI *et al.*, 2017).

Several characteristic bands indicate the functionalization of magnetite nanoparticles with cysteine: a band at 1582 cm^{-1}, associated with the asymmetric bending of amino groups (NH$_3^+$) (CAMPOS *et al.*, 2021); bands at 1620 cm^{-1} and 1404 cm^{-1}, corresponding to the asymmetric and symmetric stretching of COO$^-$ groups, respectively (CAMPOS *et al.*, 2021); a band at 1483 cm^{-1} assigned to N-H bending (FAN, Hong Lei *et al.*, 2016); and bands between 1000 and 1300 cm^{-1}, indicating vibrations of C-O, C-N, and C-S bonds (FAN, Hong Lei *et al.*, 2016; SAFAEI-GHOMI; EBRAHIMI, 2022). Moreover, the disappearance of the band at 2557 cm^{-1}, related to -SH groups of cysteine, indicates that the functionalization occurs through Fe-S interaction (BASHIR *et al.*, 2021; CAMPOS *et al.*, 2021). However, this evidence should be viewed with caution, as the -SH band is weak, and its disappearance may also result from the formation of disulfide bridges due to cysteine dimerization to cystine (CAMPOS *et al.*, 2021).

Upon CALA immobilization on the supports, there is a noticeable increase in the intensities of the bands between 950 and 1150 cm^{-1}, characteristic of this enzyme, as shown in the spectrum of the free CALA in Fig. 22b (MONTEIRO, R.R.C. Rodolpho R.C. *et al.*, 2022). This provides evidence that the immobilization of CALA was successfully achieved.

3.3.1.3 Elemental analysis

Through elemental analysis of Fe$_3$O$_4$@LC nanoparticles, the following essential percentages were determined: 6.43% ± 0.10% of C, 1.32% ± 0.07% of H, 2.68% ± 0.22% of N, and 5.71% ± 0.66% of S. These values are in good agreement with the centesimal composition of cysteine (elemental proportions): 29.7% C, 5.8% H, 11.6% N, 26.4% O, and 26.5% S. The mean percentages of N and H were slightly higher than the theoretical prediction, although within the limits of experimental error. These deviations could be attributed to residual ammonia and surface hydroxyl groups.

The recorded percentages for the sample are approximately 1/5 (22%) of the theoretical values, attributed to the inorganic nature of most of the material weighed for measurement and which does not respond in the analysis. Consequently, 22% may represent the organic matter (cysteine) present on the surfaces of the functionalized nanoparticles. The fact that the elemental proportions match those in cysteine provides strong evidence that the core structure of the functionalizing agent was preserved during synthesis without fragmentation.

3.3.1.4 Quantification of free thiol groups on the surface of Fe₃O₄@LC

To determine the quantity of thiol groups on the surface of Fe_3O_4 nanoparticles coated with cysteine, the material reacted with the specific thiol reagent, DTNB. Based on a standard curve constructed through the reaction of solutions with varying concentrations of cysteine with DTNP (Abs = 0.0045 [-SH] + 0.1067, R^2 = 0.9992), it was estimated that the Fe_3O_4@LC sample contained 22 ± 1 μmol of thiols per gram. These values are notably higher, nearly double, compared to those reported in the literature, which typically hover around 12 μmol g^{-1} (BRITOS *et al.*, 2019; HADDAD *et al.*, 2015). In other studies, weight-to-weight ratios of magnetite: cysteine between 10 and 20 were used, while the theoretical ratio in this work is 1:2. This may indicate a higher functionalization efficiency owing to the powerful sonochemical technique (BRITOS *et al.*, 2019; HADDAD *et al.*, 2015).

It is also important to note that the quantity of free thiols on the surface suggests that this functional group does not solely mediate cysteine interaction. Taking into account the estimate of organic matter derived from elemental analysis (22%), it is conceivable that approximately 1.21 ± 0.06% of cysteine on the surface exists in its reduced form. The remaining portion of this functionalizing agent either interacts through thiol groups (-SH) or is converted to cysteine.

3.3.1.5 SEM

Fig. 23 shows SEM micrographs depicting the evolution of Fe_3O_4@LC nanoparticles and their subsequent modifications (Fe_3O_4@LC-GLU) leading to the development of biocatalysts, namely Fe_3O_4@LC-CALA and Fe_3O_4@LC-GLU-CALA. As evident, these nanoparticles exhibit a predominantly quasi-spherical morphology. Following the modification processes, the surface texture becomes notably smoother, with inter-particle voids being filled by compounds generated during the immobilization process, originating from glutaraldehyde (GLU) and CALA. These observations corroborate the successful enzyme immobilization process.

Figure 23 – SEM images of the samples Fe3O4@LC, Fe$_3$O$_4$@LC-CALA, Fe$_3$O$_4$@LC-GLU and Fe$_3$O$_4$@LC-GLU-CALA, obtained at 250 000 x magnification.
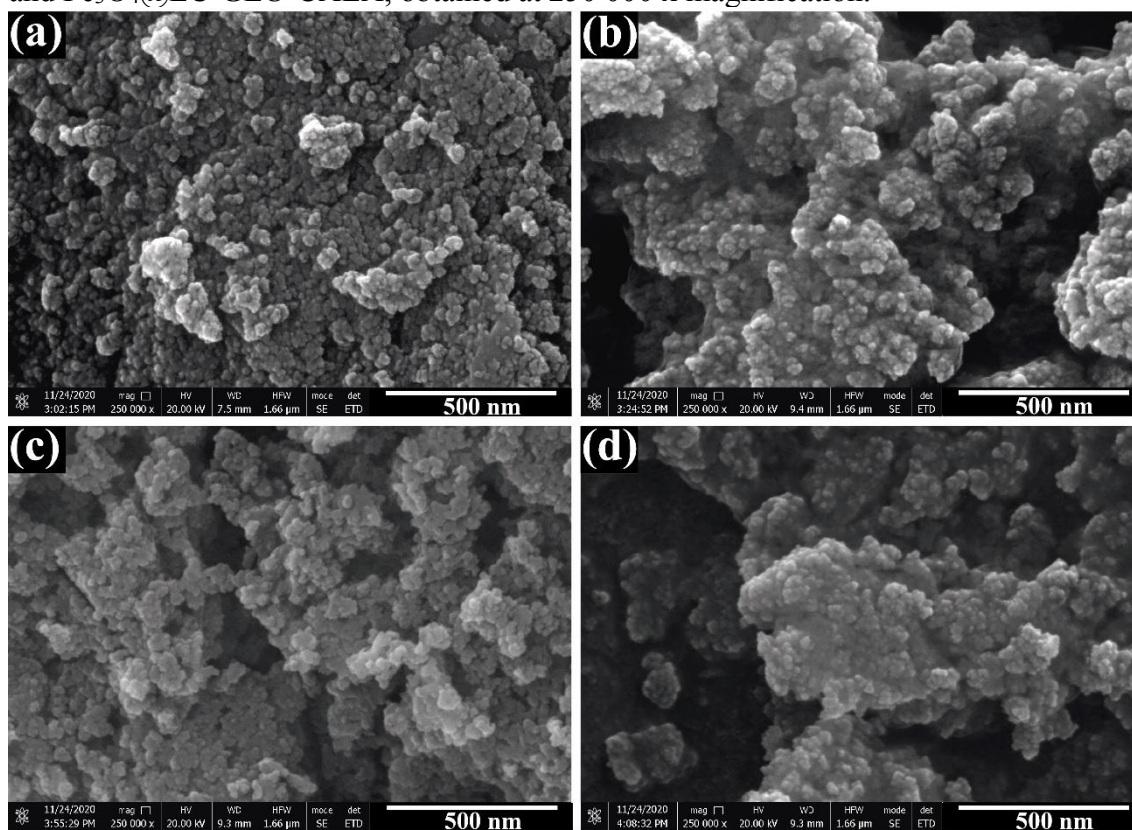
Source: the author.

In order to obtain further insights into the elemental composition of the biocatalyst surfaces, EDS mapping was employed. Fig. 24 presents the SEM images showcasing element distribution alongside their respective spectra. Both the Fe$_3$O$_4$@LC and Fe$_3$O$_4$@LC-GLU samples exhibit a high concentration of iron and oxygen on their surfaces, aligning with the anticipated characteristics of magnetite. Upon CALA immobilization via physical and chemical routes, there is a discernible elevation in carbon density on the surface, further confirming the effectiveness of the immobilization process.

Figure 24 – SEM images showing element mapping by EDS (inset) for samples Fe_3O_4@LC (a), Fe_3O_4@LC-CALA (c), Fe_3O_4@LC-GLU (e) and Fe_3O_4@LC-GLU-CALA (g), as well as their corresponding EDS spectra ((b), (d), (f) and (h)).
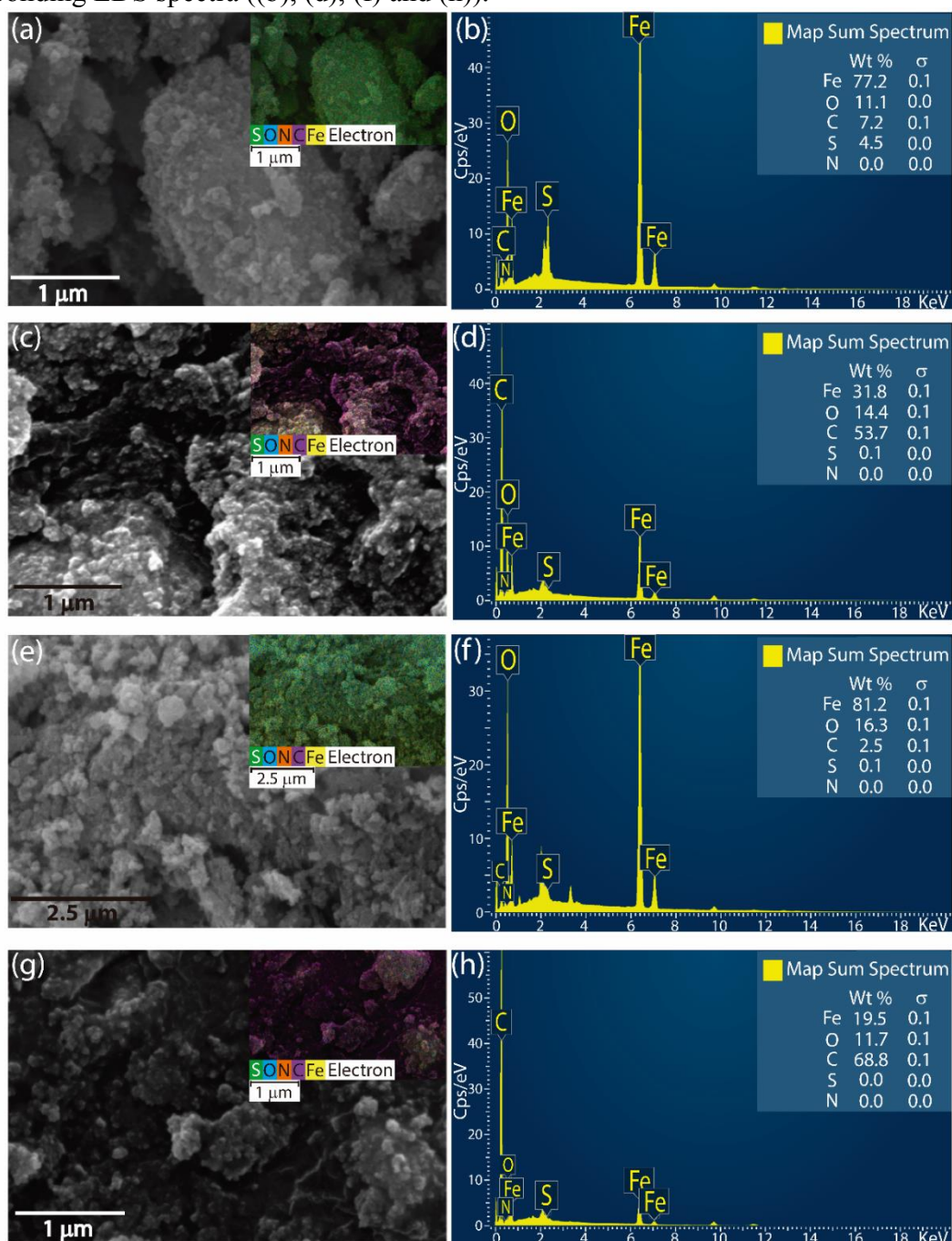
Source: the author.

3.3.1.6 TEM

TEM analysis was employed to gain a clearer understanding of the bulk morphology of Fe_3O_4 within the materials. Fig. 25 provides micrographs of the Fe_3O_4@LC sample ((a) and (b)) as well as Fe_3O_4@LC-CALA ((c) and (d)), alongside particle size

distribution histograms derived from the images. The quasi-spherical morphology is likewise confirmed by TEM. The Fe_3O_4@LC particles measure approximately 11.3±2.4 nm in size, while the Fe_3O_4@LC-CALA particles exhibit a size of roughly 11.1±2.4 nm. Statistical analysis reveals no significant size disparity between the two sample types. This is attributed to TEM size estimation focusing only on bulk Fe_3O_4, as the immobilized CALA does not have sufficient opacity to allow a reliable estimation of its length through imaging. Notably, a faint halo is discernible around the Fe_3O_4 bulk in Fig. 25c, providing compelling evidence that CALA immobilization occurred on the nanoparticle surface.

Figure 25 – TEM micrographs for the Fe3O4@LC sample ((a) and (b)) and Fe3O4@LC-CALA sample ((c) and (d)). Particle size distribution histograms are provided as insets in (a) and (c).
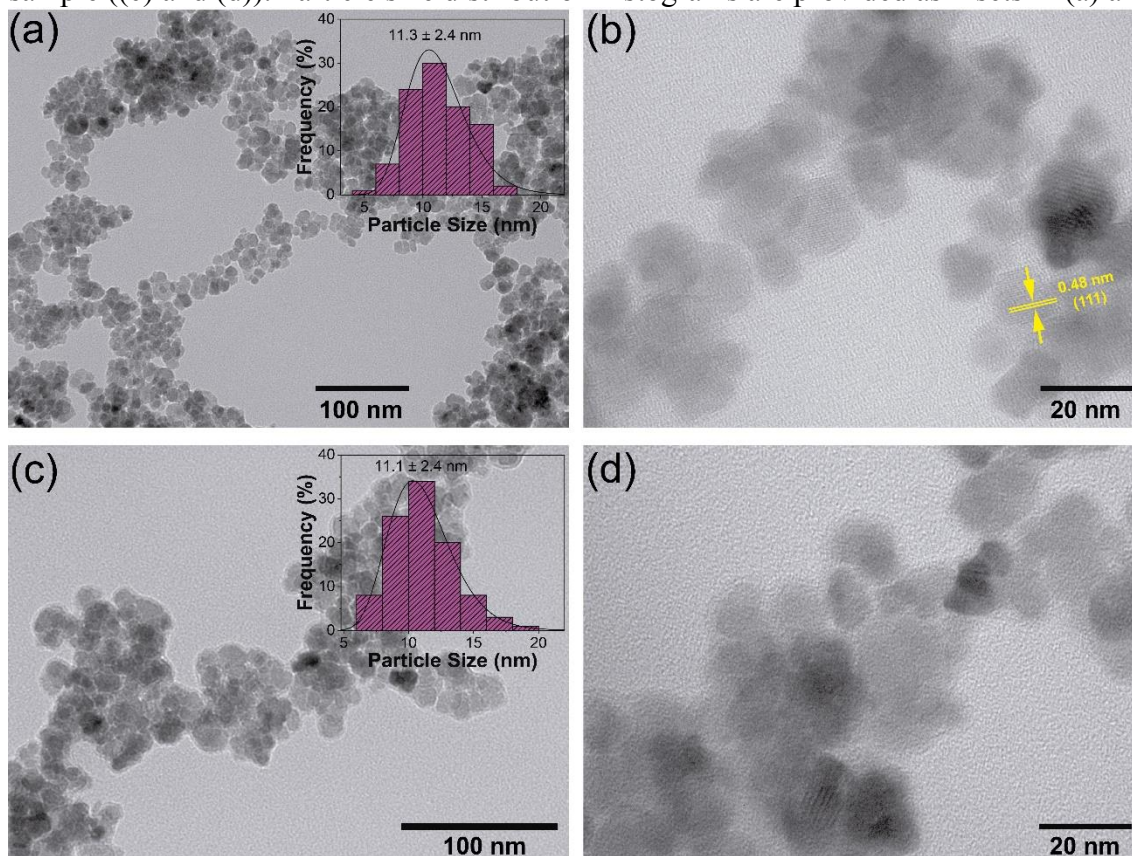
Source: the author.

3.3.1.7 XPS

To further assess the mechanism of interaction between cysteine and Fe_3O_4 on the support, XPS analysis was carried out. Fig. 26 shows the survey spectrum, complemented by high-resolution spectra for the elements Fe, O, N, C, and S.

Figure 26 – XPS analysis: (a) Survey spectrum and high-resolution spectra for (b) Fe, (c) O, (d) N, (e) C, and (f) S, providing insights into the elemental composition and bonding characteristics of the biocatalyst surface.
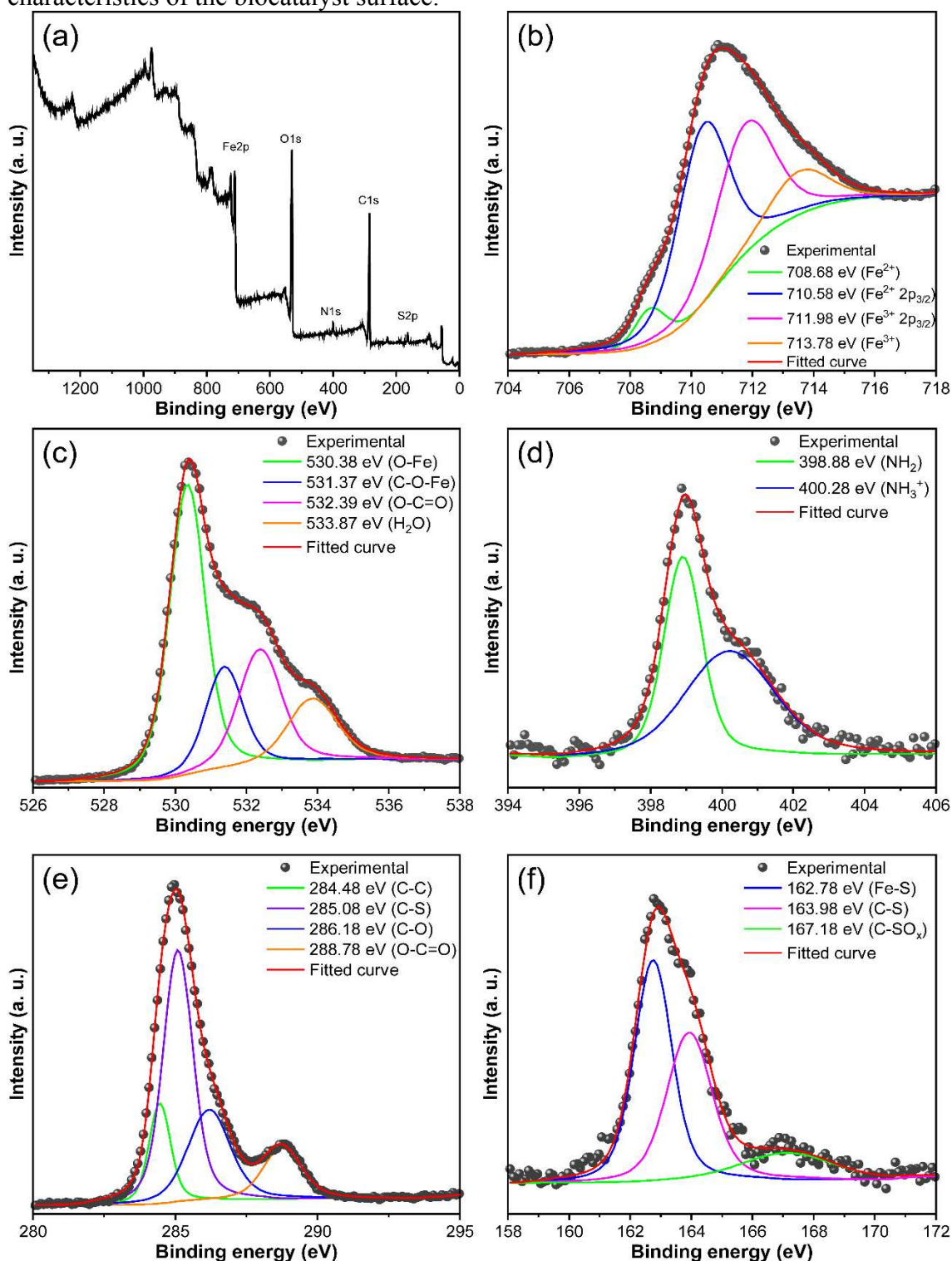
Source: the author.

Deconvolution of the Fe 2p spectrum (Fig. 26b) revealed the presence of two doublets at approximately 708.68 and 711.98 eV, corresponding to the Fe^{2+} and Fe^{3+} states,

respectively, intrinsic to magnetite (BASHIR *et al.*, 2021; BIESINGER *et al.*, 2011; COHEN; GEDANKEN; ZHONG, 2008). In the O 2s spectrum (Fig. 26c), four discernible peaks at 530.38 eV, 531.37 eV, 532.39 eV, and 533.87 eV were identified, attributed to the Fe-O bonds, carboxyl group interactions with iron (C-O-Fe), bonding in carboxylate groups, and adsorbed water on the nanoparticle surface (ZUBIR *et al.*, 2014). This observation strongly suggests that cysteine primarily interacts through carboxylate groups. The N 1s spectrum revealed two contributions, corresponding to deprotonated (400.28 eV) and protonated (398.88 eV) amino groups (BASHIR *et al.*, 2021). The presence of -NH$_3^+$ on the surface partially contributes to nanoparticle stabilization and -NH$_2$ groups serves as an anchoring site for CALA through its linkage with glutaraldehyde. Deconvolution of the C 1s spectrum exhibited four distinctive peaks at 284.48 eV, 285.08 eV, 286.18 eV, and 288.78 eV, corresponding to C-C, C-S, C-O, and O=C-O binding energies, affirming the successful functionalization of nanoparticles with cysteine (BASHIR *et al.*, 2021; ZUBIR *et al.*, 2014). The S 2p spectrum displayed three distinct components after deconvolution at approximately 162.78 eV, 163.98 eV, and 167.18 eV, attributed to Fe-S, C-S, and C-SO$_x$ binding energies, signifying that cysteine is partially linked via thiol groups, either directly to iron or oxygen atoms on the surface of the magnetite nanoparticles (BASHIR *et al.*, 2021). Through deconvolution of the high-resolution spectrum for S 2p, it was not possible to distinguish the thiol groups (-SH) of cysteine from the groups (S-S) of cystine, as both exhibit binding energies around 163.98 eV (SALLES *et al.*, 2018).

3.3.1.8 VSM

Given its heterogeneous nature, the recovery of these catalysts from the reaction medium is paramount. In this regard, magnetic separation is employed, making it crucial to assess the material's magnetic properties. Fig. 27a shows the magnetization curves of the materials obtained during the biocatalyst development.

The Fe$_3$O$_4$@LC support exhibited a saturation magnetization (represented as M_s, the maximum magnetization achieved by the sample under the applied field) of 58.72 emu g^{-1}, slightly lower than values reported in previous studies on bulk magnetite (FAN, Hong Lei *et al.*, 2016; SRIKHAOW *et al.*, 2020). This difference is partly attributed to the presence of diamagnetic cysteine in a fraction of the analyzed sample (SRIKHAOW *et al.*, 2020). As more molecules adsorb or are covalently bound onto the nanoparticles' surface, a reduction in M_s is observed. Materials such as Fe$_3$O$_4$@LC-CALA, Fe$_3$O$_4$@LC-GLU, and Fe$_3$O$_4$@LC-GLU-

CALA exhibited M_s values of 53.28, 45.54, and 41.96 emu g^{-1}, respectively. This reduction was expected due to decreased magnetic fraction within the samples.

Figure 27 – Magnetization curves at room temperature (25°C) for the Fe$_3$O$_4$@LC, Fe$_3$O$_4$@LC-CALA, and Fe$_3$O$_4$@LC-GLU-CALA samples (a) and comparison of the saturation magnetization (MS), remanent magnetization (Mr) and coercive field (Hc) of the samples (b).
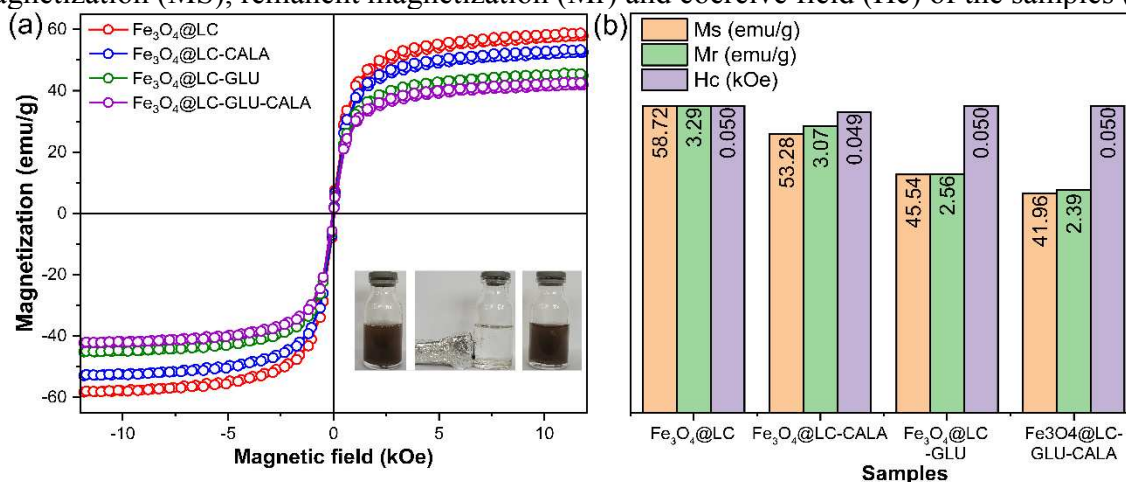
It is worth noting that all samples displayed low hysteresis, with remanent magnetization (M_r) values of 3.29, 3.07, 2.56, and 2.39 emu g^{-1}, and coercive field (H_c) values of 0.050, 0.049, 0.050, and 0.050 kOe, respectively, for Fe$_3$O$_4$@LC, Fe$_3$O$_4$@LC-CALA, Fe$_3$O$_4$@LC-GLU, and Fe$_3$O$_4$@LC-GLU-CALA, as shown in Fig. 27b. Thus, based on a magnetite core, a typical ferrimagnetic material, these materials exhibited characteristics very close to superparamagnetic. This is due to their ultra-small particle size, which enables natural Brownian motion to disorient the magnetic moments without a magnetic field (SOARES *et al.*, 2021).

Therefore, these observed magnetic properties align with the application's requirements. The nanocatalysts disperse quickly within the reaction mixture through vigorous shaking, as depicted in the inset in Fig. 27a for the Fe$_3$O$_4$@LC-GLU-CALA sample. Upon cessation of agitation and the approach of a magnet, the immobilized enzyme is swiftly recovered and can be reused, as evidenced by the clear solution. This phenomenon also suggests that obtaining a product free from enzymatic impurities is simplified. Given that the Fe$_3$O$_4$ magnetic core retains minimal magnetization, as evidenced by the low M_r values, interparticle magnetic attraction does not lead to aggregation. Hence, gentle agitation is sufficient to homogeneously redisperse the enzyme in the reaction medium. This behavior is explicitly

illustrated Fig. 27a's inset, where subsequent stirring uniformly disperses the suspension, confirming that stability remains unaffected by this separation method.

3.3.2 Immobilization parameters

The immobilization parameters were evaluated using the *p*-NPB hydrolysis reaction (50 mM) after 5 hours of immobilization, employing a protein load of 1 mg of protein per g of support in the presence of 0.01% Triton X-100 in phosphate buffer 25 mM pH 7.0. This surfactant, commonly used to desorb enzymes from hydrophobic supports, was used to prevent the formation of enzyme-enzyme aggregates because studies have already shown a positive effect on enzyme activity (DOS SANTOS *et al.*, 2015; SÁNCHEZ-OTERO *et al.*, 2008).

The immobilization yield (IY) was calculated by the decrease of activity in the supernatant, compared to a reference enzyme solution under identical conditions in the absence of NPs. As shown in Table 6 and in Fig. 28a, CALA immobilized in the glutaraldehyde-activated support performed better than in non-activated NPs, achieving an IY around 85.0±2.6%. This substantial role of glutaraldehyde in the immobilization could be attributed to the Schiff base formation when aldehydes groups react with CALA amino-terminal groups, avoiding its desorption from the support (MONTEIRO, Rodolpho R. C. *et al.*, 2019). Furthermore, glutaraldehyde is a relatively hydrophobic molecule and acts as a spacer, facilitating the enzyme accommodation on the NPs surface. The more hydrophobic surface for Fe_3O_4@LC-GLU, compared to Fe_3O_4@LC, facilitates enzyme immobilization by interfacial activation.

Table 6 – Immobilization of CALA (1 mg of protein per 1 g of support) performed in sodium phosphate buffer solution (pH 7.0 and 25 mM) for 5h at 25 °C. Immobilization Yield (IY), Theoretical Activity (At_T), Derivative Activity (At_D) and Recovery Activity (At_R).

Sample	IY (%)	At_T (U/g)	At_D (U/g)	At_R (%)
Fe_3O_4@LC-GLU-CALA	85.0 ± 2.6	212.5 ± 1.3	186.4 ± 4.3	87.7 ± 0.9
Fe_3O_4@LC-CALA	33.0 ± 2.4	82.5 ± 0.6	51.7 ± 2.7	62.7± 1.5

Source: the author.

Dutt and Upadhyay used glutaraldehyde to immobilize lipase from *Bacillus subtilis* onto cysteine-capped silver nanoparticles and found an immobilization yield of 70% and a recovery activity of 66% (DUTT; UPADHYAY, 2018). Monteiro et al. immobilized CALA on chitosan-coated Fe_3O_4 NPs and found an IY of 84.1±1.0% using glutaraldehyde-activated support, which also had better performance than the non-activated NPs (MONTEIRO,

Rodolpho R. C. *et al.*, 2019). Covalent CALA immobilization was also performed on APTES-coated magnetic NPs, which achieved an IY of 100±1.2%, superior to this work (MONTEIRO, Rodolpho R.C. *et al.*, 2019). However, the At_D values were not so far from the 198.3 ± 2.7 U/g obtained by the authors.

Figure 28 – Immobilization parameters of CALA on Fe_3O_4@LC and Fe_3O_4@LC-GLU supports and pH profile for free and covalently bound enzyme on Fe_3O_4@LC-GLU: (a) Comparison of the CALA immobilization parameters (1 mg of protein per 1 g of support) carried out in 25 mM phosphate buffer, pH 7.0, at 25 degrees for 5 hours; (b) Immobilization course under similar loading conditions, pH, and temperature, but with varying times from 0.5 to 6 hours; (c) Loading capacity of Fe_3O_4@LC-GLU for CALA (1-25 mg of protein per 1 g of support) conducted under conditions of pH, time, and temperature like (a); (d) pH profile of CALA and Fe_3O_4@LC-GLU-CALA, where 100% represents CALA activity at pH 7.0 (optimal conditions for the enzyme).
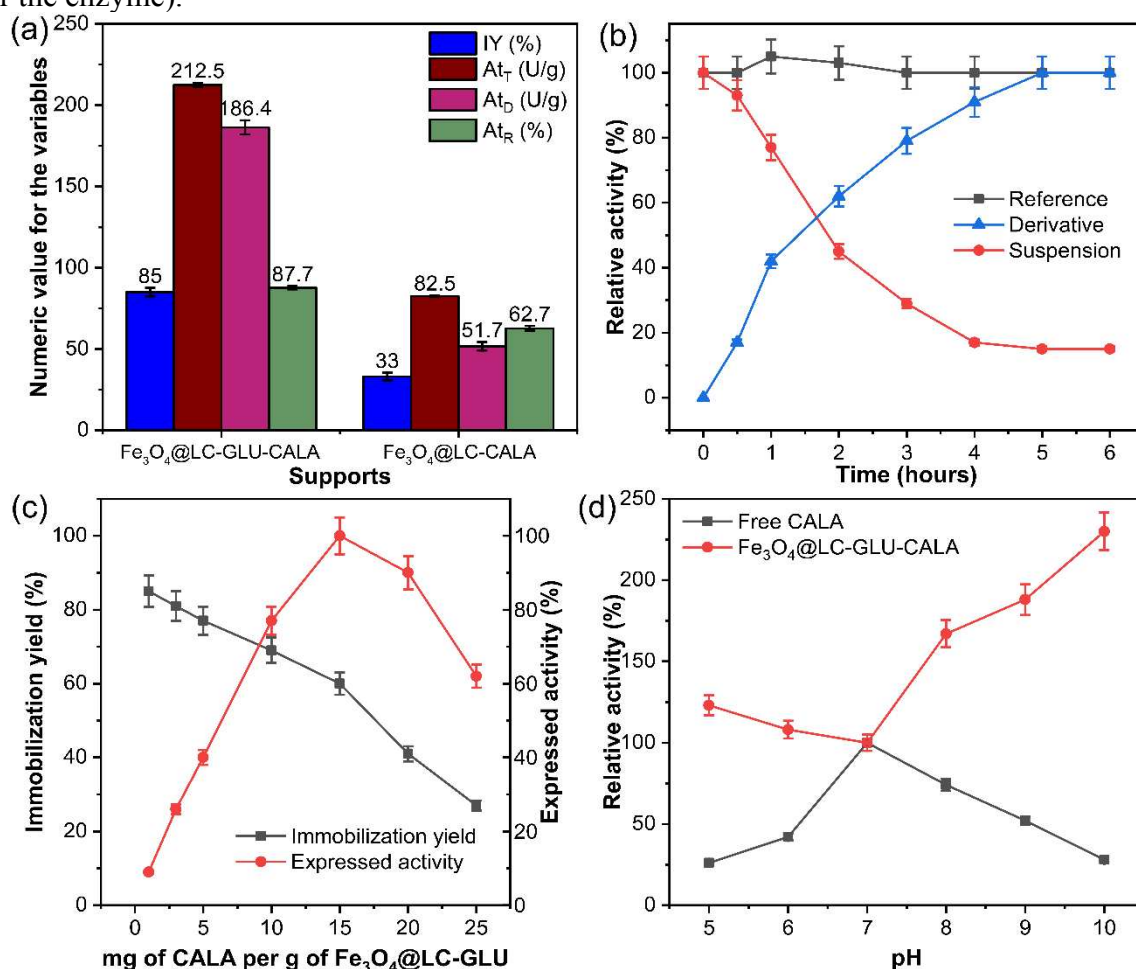
Source: the author.

The time dependence on CALA immobilization at pH 7.0 (PBS 25 mM), 25 °C and enzyme loading of 1 g of enzyme per g of support was investigated by measuring the reduction in the activity of the supernatant over 30 min to 6 h. As shown in Fig. 28b, the relative activity for the derivative increases over time and remains constant (close to the activity for the free

enzyme) after 5 h. Although the reaction between glutaraldehyde and amino groups is usually fast, more excellent activities for the derivative were favored by longer incubation time. This observation indicates the occurrence of slower processes involving the mechanism of CALA immobilization, such as the well-oriented enzymatic adsorption before the formation of enzyme-support multipoint covalent bonds. The previous adsorption on the support is particularly necessary for the immobilization of enzymes with pI close to 7.0 at a low ionic strength medium (BEZBRADICA; MATEO; GUISAN, 2014). Besides, slower immobilization processes minimize proteins stacking and promote a more homogenous enzyme distribution across the support's surface [9].

Bezbradica et al. used glutaraldehyde to immobilize CALB onto cysteine-activated epoxy-agarose and found a long immobilization time (BEZBRADICA; MATEO; GUISAN, 2014). They attributed this fact to reversible processes involving the formation/cleavage of Schiff bases until a derivative is irreversibly formed. The chemistry of glutaraldehyde reactions is complex, and this mechanism has not been clarified (BEZBRADICA; MATEO; GUISAN, 2014; ZHANG, Ting *et al.*, 2022).

3.3.3 Loading capacity

In order to investigate how many enzyme units can be immobilized on the support and how the enzyme activity is influenced by high enzyme loading, the IY (%) and the expressed activity for the biocatalyst suspension were evaluated at several enzyme loadings (1-25 mg of enzyme/g of support). As shown in Fig. 28c, higher IY were obtained with lower enzyme loading and the optimal condition was observed with 1 mg of enzyme per g of Fe_3O_4@LC-GLU. As the enzyme covers the support's surface, it becomes increasingly tricky to immobilize new ones, and they remain in the supernatant. However, using high enzyme loads in the immobilization protocol, higher expressed activity is obtained for the biocatalyst, reaching the maximum with 15 mg of CALA per g of Fe_3O_4@LC-GLU. From that peak, the expressed activity drastically reduces. This phenomenon is probably caused by enzyme-enzyme interactions and stacks, which generate steric hindrances, inhibiting the flexible stretching of enzyme conformation and inactivating it (TANG *et al.*, 2019).

3.3.4 pH profile

Enzymes have their structure stabilized by groups very sensitive to pH changes. To evaluate pH influence on free and immobilized CALA performance, these biocatalysts' relative activities were evaluated at pH range from 5.0 to 9.0, as shown in Fig. 28d. Free CALA presented the highest activity at pH 7 and lower activity at acidic and alkaline pH, which is in line the findings of other studies (CAVALCANTE *et al.*, 2022; MONTEIRO, R.R.C. Rodolpho R.C. *et al.*, 2022). This optimum pH for the free enzyme's activity is very close to its isoelectric point (pI = 7.5) and represents the condition in which this enzyme is explicitly in its most favorable conformation for catalysis. Neither does an enzyme's optimum pH always coincide with its pI. At neutral pH, covalently immobilized CALA presented the same free CALA activity. Still, acidic and alkaline pH increased its relative activity, a behavior somewhat similar to that found by Monteiro using chitosan-coated magnetite nanoparticles as a support (MONTEIRO, Rodolpho R. C. *et al.*, 2019). The coincidence between the activities of the free and immobilized enzyme is because CALA was immobilized at pH 7, its optimum pH. In this condition, the interaction between the enzyme and the support did not affect its conformation (no decrease in activity), due to the partially zwitterionic microenvironment on the support surface. However, the catalyst's activity tends to increase at pHs other than neutrality. This can occur due to changes in the enzyme's conformation resulting from protonation-deprotonation of its amino acids (while maintaining the integrity of the active site), or due to enhanced dispersion of the catalyst resulting from surface charge formation, typically facilitated by amino or carboxylate groups (JAMES *et al.*, 2003; STAUCH; FISHER; CIANCI, 2015). Such dispersion prevents the formation of aggregates that would occur in the free enzyme under changes in pH, temperature, and solvent (GUISAN *et al.*, 2022). Nevertheless, the mechanism behind these observations still requires further study.

3.3.5 Thermal deactivation

Biocatalysts are more sensitive to reactional conditions, such as pH, ionic strength, and temperature, unlike inorganic catalysts. To assess the resistance of these free and immobilized CALA in the face of deactivating conditions, the half-lives of these biocatalysts were measured at 70 °C and pH 5, 7 and 10. As shown in Table 7, free CALA was more stable under thermal treatment at acidic pH (5.0) and performed worse at alkaline pH (10.0), with a half-life of just 3.1 hours. However, the performance of CALA was substantially increased after

covalent immobilization, which presented a longer half-life at neutral and alkaline conditions (> 24 h).

Table 7 – Half-life for CALA and Fe_3O_4@LC-GLU-CALA at 70 °C and pHs 5, 7 and 10.

Sample	Half-life ($t_{1/2}$, hours)		
	pH 5.0	pH 7.0	pH 10.0
CALA	16.3	12.8	3.1
Fe_3O_4@LC-GLU-CALA	22.9	>24	>24

Source: the author.

3.4 Conclusion

Magnetite nanoparticles coated with L-cysteine were successfully synthesized, as confirmed by XRD, TEM, SEM, FTIR, XPS, and VSM analyses. Lipase A *Candida antarctica* (CALA) was immobilized onto these supports through physical interactions and multipoint binding facilitated by glutaraldehyde. The immobilization parameters for covalent binding (85.0% ± 2.6 for immobilization yield and 212.5 ± 1.3 U/g for specific activity) outperformed physical adsorption (33.0% ± 2.4 for immobilization yield and 82.5 ± 0.6 U/g for specific activity). Under optimal immobilization conditions – employing an enzyme load of 1 mg CALA/g of glutaraldehyde-activated support, a reaction time of 5 hours at 25°C, and pH 7.00 (25 mM) – thermal and pH inactivation analysis revealed that the half-life of the Fe_3O_4@LC-GLU-CALA catalyst exceeded that of free CALA (by more than 8 times at pH 10). These results, along with the XPS and FTIR analyses, corroborate the successful immobilization of CALA on this new support.

4 CHAPTER 4 – GENERAL CONCLUSIONS

In conclusion, the research presented in Chapters 1 and 2 offers valuable insights into the synthesis and application of innovative nanocatalysts for environmental and enzymatic processes. In Chapter 1, the synthesis of FeCo nanoparticles through the polyol method showcased the influence of precursor composition on the resulting material's properties. Optimal conditions, characterized by [OH-] / [Metal] = 26 and [Fe] / [Co] = 2, led to the formation of well-defined FeCo nanoparticles with enhanced catalytic properties, particularly in the degradation of RhB. However, the challenge of metal leaching was observed, emphasizing the need for further investigations to address this issue.

Chapter 2 delved into the synthesis of magnetite nanoparticles coated with L-cysteine and their application as a support for immobilizing Lipase A *Candida antarctica* (CALA). The detailed characterization using various techniques confirmed the successful synthesis and immobilization processes. Covalent binding, with impressive results in terms of immobilization yield and specific activity, outperformed physical adsorption. Moreover, the Fe3O4@LC-GLU-CALA catalyst exhibited superior stability compared to free CALA, especially under conditions of higher pH.

Together, these chapters contribute to the expanding field of nanocatalysts, providing not only insights into synthesis optimization but also addressing challenges related to catalytic efficiency and stability. The identified areas for further research, such as preventing metal leaching in Chapter 2 and optimizing immobilization strategies in Chapter 3, open avenues for future investigations in the quest for more sustainable and effective catalytic processes.

5 CHAPTER 5 – SCIENTIFIC PRODUCTION

5.1 Published articles

1. **De Menezes, Fernando Lima**; Andrade Neto, Davino Machado; Rodrigues, Maria Do Livramento Linhares; Lima, Helder Levi Silva; Paiva, Denis Valony Martins; Da Silva, Marcelo Antônio Santos; Fechine, Lillian Maria Uchôa Dutra; Sombra, Antônio Sérgio Bezerra; Freire, Rafael Melo; Denardin, Juliano Casagrande; Rosa, Morsyleide De Freitas; De Souza Filho, Men De Sá Moreira; Mazzetto, Selma Elaine; Fechine, Pierre Basílio Almeida. From Magneto-Dielectric Biocomposite Films to Microstrip Antenna Devices. JOURNAL OF COMPOSITES SCIENCE, v. 4, p. 144, 2020.

2. Moreira, Katerine Da S.; De Oliveira, André L. B.; Júnior, Lourembergue S. De M.; Monteiro, Rodolpho R. C.; Da Rocha, Thays N.; **Menezes, Fernando L.**; Fechine, Lillian M. U. D.; Denardin, Juliano C.; Michea, Sebastian; Freire, Rafael M.; Fechine, Pierre B. A.; Souza, Maria C. M.; Dos Santos, José C. S. Lipase From Rhizomucor miehei Immobilized on Magnetic Nanoparticles: Performance in Fatty Acid Ethyl Ester (FAEE) Optimized Production by the Taguchi Method. FRONTIERS IN BIOENGINEERING AND BIOTECHNOLOGY, v. 8, p. 1-17, 2020.

3. Pinto, Daiane Dos Santos; Silva, Sandra Dos Santos; Figueiredo, Raimundo Wilane De; **Menezes, Fernando Lima De**; Castro, Janevane Silva De; Pimenta, Antônia Torres Ávila; Santos, João Evangelista De Ávila Dos; Nascimento, Ronaldo Ferreira Do; Gaban, Socorro Vanesca Frota. Production of healthy mixed vegetable beverage: antioxidant capacity, physicochemical and sensorial properties. CIÊNCIA E TECNOLOGIA DE ALIMENTOS (ONLINE), v. 42, p. 1, 2021.

4. Nunes, Yale Luck; **De Menezes, Fernando Lima**; De Sousa, Isamayra Germano; Cavalcante, Antônio Luthierre Gama; Cavalcante, Francisco Thálysson Tavares; Da Silva Moreira, Katerine; De Oliveira, André Luiz Barros; Mota, Gabrielly Ferreira; Da Silva Souza, José Erick; De Aguiar Falcão, Italo Rafael; Rocha, Thales Guimaraes; Valério, Roberta Bussons Rodrigues; Fechine, Pierre Basílio Almeida; De Souza, Maria Cristiane Martins; Dos Santos, José C.S. Chemical and physical Chitosan modification for designing enzymatic industrial biocatalysts: How to choose the best strategy?. INTERNATIONAL JOURNAL OF BIOLOGICAL MACROMOLECULES, v. 181, p. 1124-1170, 2021.

5. Santana, Allan M.; Freire, Tiago M.; Da Silva, Francisco L.F.; **Menezes, Fernando L.**; Ramos, Lauren L.; Cavalcante, Giovanna R.; Fechine, Lillian M.U.D.; Vieira, Laís

H.S.; Ferreira, Odair P.; Freire, Rafael M.; Denardin, Juliano C.; Lopes, Gisele S.; Matos, Wladiana O.; Fechine, Pierre B.A. Organophosphorus halloysite nanotubes as adsorbent for lead preconcentration in wine and grape juice. APPLIED CLAY SCIENCE, v. 200, p. 105912, 2021.

6. Da Silva, Francisco L.F.; Neto, Davino M. Andrade; **De Menezes, Fernando L.**; as, Ivero P.; De Higuera, Julymar M.; Fechine, Pierre B.A.; Da Costa, Luelc S.; Nogueira, Ana R.A.; Lopes, Gisele S.; Matos, Wladiana O. Non-chromatographic arsenic speciation analyses in wild shrimp (Farfantepenaeus brasiliensis) using functionalized magnetic iron-nanoparticles. FOOD CHEMISTRY, v. 345, p. 128781, 2021.

7. Neto, Davino M.A.; Da Costa, Luelc S.; **De Menezes, Fernando L.**; Fechine, Lillian M.U.D.; Freire, Rafael M.; Denardin, Juliano C.; Bañobre-López, Manuel; Vasconcelos, Igor F.; Ribeiro, Thiago S.; Leal, Luzia Kalyne A.M.; De Sousa, João A.C.; Gallo, Juan; Fechine, Pierre B.A. A novel amino phosphonate-coated magnetic nanoparticle as MRI contras99ficient. APPLIED SURFACE SCIENCE, v. 543, p. 148824, 2021.

8. Monteiro, Rodolpho R.C.; De Oliveira, André Luiz Barros; **De Menezes, Fernando L.**; De Souza, Maria Cristiane Martins; Fechine, Pierre B.A.; Dos Santos, José C.S. Improvement of enzymatic activity and stability of lipase A from Candid99ficienteca onto halloysite nanotubes with Taguchi method for optimized immobilization. APPLIED CLAY SCIENCE, v. 228, p. 106634, 2022.

9. Silva, Francisca Mayla Rodrigues; Da Silva, Larissa Morais Ribeiro; De Figueiredo, Raimundo Wilane; **De Menezes, Fernando Lima**; Garruti, Debora; Torres, Lucicléia Barros Vasconcelos. Yellow Mombin Nectar Enriched with Encapsulated Green Tea (*Camellia Sinensis Var Assamica*): Physical-chemical, Rheological and Sensory Aspects. JOURNAL OF CULINARY SCIENCE & TECHNOLOGY, v. 20, p. 1-14, 2022.

10. Cunha, Francisco Afranio; Agressott, Enzo Victorino Hernandez; Paschoal, Alexandre Rocha; **De Menezes, F.L.**; Martins, R.T.; Barbosa, Rita De Cássia C.; Cunha, M.C.S.O.; Menezes, E.A.; Coutinho, Henrique Douglas Melo; Fechine, P.B.A. . Ceftazidime and 4-nitrophenol inactivation using alginate-based spheres inlaid with mycogenic silver nanoparticles. MATERIALS TODAY SUSTAINABILITY, v. 18, p. 100114, 2022.

11. Maciel, Antônio Auberson Martins; Cunha, Francisco Afrânio; Freire, Tiago Melo; **De Menezes, Fernando Lima**; Fechine, Lillian Maria Uchoa Dutra; Rocha, Janaina Sobreira; De Cássia Carvalho Barbosa, Rita; Martins, Roxeane Teles; Da Conceição

Dos Santos Oliveira Cu, Maria; Santos-Oliveira, Ralph; Queiroz, Maria Veraci Oliveira; Fechine, Pierre Basílio Almeida. Development and evaluation of an anti-candida cream based on silver nanoparticles. 3 Biotech, v. 13, p. 352, 2023.

12. Mallmann, Eduardo José Juca; Cunha, Francisco Afrânio; Agressott, Enzo Victorino Hernandez; **De Menezes, Fernando Lima**; De Cássia Carvalho Barbosa, Rita; Martins, Roxeane Teles; Dos Santos Oliveira Cunha, Maria Da Conceição; Queiroz, Maria Veraci Oliveira; Coutinho, Henrique Douglas Melo; De Vasconcelos, John Eversong Lucena; Fechine, Pierre Basílio Almeida. Antifungal Activity of Nanobiocomposite Films Based on Silver Nanoparticles Obtained Through Green Synthesis. CURRENT MICROBIOLOGY, v. 80, p. 251, 2023.

13. Barros, Sâmela Leal; Frota, Maryana Melo; **De Menezes, Fernando Lima**; De Brito Araújo, Ana Júlia; Dos Santos Lima, Marcos; Fernandes, Victor Borges; Santos, Newton Carlos; Vieira, Ícaro Gusmão Pinto; De Vasconcelos, Lucicléia Barros. Physical-Chemical, Functional and Antioxidant Properties of Dehydrated Pumpkin Seeds: Effects of Ultrasound Time and Amplitude and Drying Temperature. WASTE AND BIOMASS VALORIZATION, v. 80, p. 1, 2023.

14. Da Silva, Francisco L.F.; Lima, Francisco E.H.; Andrade Neto, Davino M.; **De Menezes, Fernando L.**; M.U.D. Fechine, Lillian; Akhdhar, Abdullah; Ribeiro, Livia P.D.; Nogueira, Ana R.A.; Fechine, Pierre B.A.; Lopes, Gisele S.; Matos, Wladiana O. Magnetic solid phase extraction as a nonchromatographic method for the quantification of ultratrace inorganic arsenic in rice by inductively coupled plasma-optical emission spectrometry (ICP OES). FOOD CHEMISTRY, v. 412, p. 135461, 2023.

5.2 Submitted articles

1. **Menezes, Fernando L. de.**; Freire, Tiago M.; Nascimento, Carlos P. G..; Fechine, Líllian M. U. D.; Costa, Victor M.; Freire, Rafael M.; Longhinotti, Elisane; Nascimento, José H. O.; Denardin, Juliano C.; Fechine, Pierre B. A. FeCo@C nanocomposites a100ficientent peroxymonosulfate activator for organic pollutants degradation. ENVIRONMENTAL SCIENCE AND POLLUTION RESEARCH.

2. **Menezes, Fernando L. de.**; Freire, Tiago M.; Monteiro, Rodolpho R. C.; Antunes, Renato A.; Melo, Rafael L. F.; Freire, Rafael M.; Santos, José C. S.; Fechine, Pierre B. A. L-Cysteine-Coated Magnetite Nanoparticles as a New Platform for enzymes

Immobilization: Amplifying Biocatalytic Activity for Industrial Applications. MATERIALS TODAY NANO.

5.3 Book chapter

1. Rocha, J. S.; Freire, T. M.; Silva, C. S. F.; Chaves, J. M. C.; **Menezes, F. L.**; Amorim, L.; Araujo, E. V.; Fechine, P. B. A.; Freire, R. M. Nanopartículas magnéticas. In: Pierre Basílio Almeida Fechine. (Org.). Avanços no desenvolvimento de nanomateriais. 1ed. Fortaleza: Imprensa Universitária UFC, 2020, v. Único, p. 88-138.

2. Fechine, L. M. U. D.; **Menezes, F. L.**; Xavier, L. N.; Oliveira, A. S.; Fechine, Pierre Basílio Almeida. Nanoparticles by Ultrasound Irradiation: Organic and Inorganic Materials. In: Ronaldo Ferreira do Nascimento; Vicente de Oliveira Sousa Neto; Pierre Basílio Almeida Fechine; Paulo de Tarso Cavalcante Freire. (Org.). Nanomaterials and Nanotechnology: Biomedical, Environmental, and Industrial Applications. 1ed.Singapore: Springer Nature, 2021, v. 1, p. 313-.

REFERENCES

ABBAS, Mohamed *et al.* One-Pot Synthesis of High Magnetization Air-Stable FeCo Nanoparticles by Modified Polyol Method. **Materials Letters**, [*s. l.*], v. 91, p. 326–329, 15 Jan. 2013.

ABDEL-SALAM, M. O.; YOON, Taeho. Cobalt-Ferrite/Ag-FMWCNT Hybrid Nanocomposite Catalyst for Efficient Degradation of Synthetic Organic Dyes via Peroxymonosulfate Activation. **Environmental Research**, [*s. l.*], v. 205, p. 112424, 1 Apr. 2022.

AHMAD, Alamri Rahmah Dhahawi *et al.* Fenton Degradation of Ofloxacin Antibiotic Using Calcium Alginate Beads Impregnated with Fe_3O_4-Montmorillonite Composite. **International Journal of Biological Macromolecules**, [*s. l.*], v. 229, p. 838–848, 28 Feb. 2023.

ALBAAJI, Amar J. *et al.* Effect of Ball-Milling Time on Mechanical and Magnetic Properties of Carbon Nanotube Reinforced FeCo Alloy Composites. **Materials and Design**, [*s. l.*], v. 122, p. 296–306, 15 May 2017.

ALEJALDRE, Lorea *et al.* Tuning Selectivity in CalA Lipase: Beyond Tunnel Engineering. **Biochemistry**, [*s. l.*], v. 62, n. 2, p. 396–409, 17 Jan. 2023. Disponível em: https://pubs.acs.org/doi/full/10.1021/acs.biochem.2c00513. Acesso em: 19 sep. 2023.

ALI, Fayaz *et al.* Bactericidal and Catalytic Performance of Green Nanocomposite Based-on Chitosan/Carbon Black Fiber Supported Monometallic and Bimetallic Nanoparticles. **Chemosphere**, [*s. l.*], v. 188, p. 588–598, 1 Dec. 2017.

ALINEZHAD, Heshmatollah *et al.* SO3H-Functionalized Nano-MGO-D-NH2: Synthesis, Characterization and Application for One-Pot Synthesis of Pyrano[2,3-d]Pyrimidinone and Tetrahydrobenzo[b]Pyran Derivatives in Aqueous Media. **Applied Organometallic Chemistry**, [*s. l.*], v. 33, n. 3, p. e4661, 1 Mar. 2019. Disponível em: https://onlinelibrary.wiley.com/doi/full/10.1002/aoc.4661. Acesso em: 20 nov. 2023.

ALIREZVANI, Zahra; DEKAMIN, Mohammad G.; VALIEY, Ehsan. Cu(II) and Magnetite Nanoparticles Decorated Melamine-Functionalized Chitosan: A Synergistic Multifunctional Catalyst for Sustainable Cascade Oxidation of Benzyl Alcohols/Knoevenagel Condensation. **Scientific Reports 2019 9:1**, [*s. l.*], v. 9, n. 1, p. 1–12, 28 Nov. 2019. Disponível em: https://www.nature.com/articles/s41598-019-53765-3. Acesso em: 28 nov. 2023.

AMSARAJAN, Subbiah; JAGIRDAR, Balaji R. Air-Stable Magnetic Cobalt-Iron (Co_7Fe_3) Bimetallic Alloy Nanostructures via Co-Digestive Ripening of Cobalt and Iron Colloids. **Journal of Alloys and Compounds**, [*s. l.*], v. 816, p. 152632, 5 Mar. 2020.

AN, Li *et al.* A Highly Active and Durable Iron/Cobalt Alloy Catalyst Encapsulated in N-Doped Graphitic Carbon Nanotubes for Oxygen Reduction Reaction by a Nanofibrous Dicyandiamide Template. **Journal of Materials Chemistry A**, [*s. l.*], v. 6, n. 14, p. 5962–5970, 14 Apr. 2018. Disponível em: https://pubs.rsc.org/en/content/articlehtml/2018/ta/c8ta01247d. Acesso em: 9 feb. 2021.

ANASTAS, Paul; EGHBALI, Nicolas. Green Chemistry: Principles and Practice. **Chemical

Society Reviews, [*s. l.*], v. 39, n. 1, p. 301–312, 14 Dec. 2009. Disponível em: https://pubs.rsc.org/en/content/articlehtml/2010/cs/b918763b. Acesso em: 8 nov. 2023.

ANDRADE NETO, Davino M. *et al.* Rapid Sonochemical Approach Produces Functionalized Fe_3O_4 Nanoparticles with Excellent Magnetic, Colloidal, and Relaxivity Properties for MRI Application. **Journal of Physical Chemistry C**, [*s. l.*], v. 121, n. 43, p. 24206–24222, 25 Oct. 2017. Disponível em: http://pubs.acs.org/doi/abs/10.1021/acs.jpcc.7b04941. Acesso em: 27 oct. 2017.

ANDREEV, Andrey S. *et al.* Thermal Stability and Hcp-Fcc Allotropic Transformation in Supported Co Metal Catalysts Probed near Operando by Ferromagnetic NMR. **Physical Chemistry Chemical Physics**, [*s. l.*], v. 17, n. 22, p. 14598–14604, 14 Jun. 2015. Disponível em: www.rsc.org/pccp. Acesso em: 27 jan. 2021.

ANSARI, Sumayya M. *et al.* Particle Size, Morphology, and Chemical Composition Controlled $CoFe_2O_4$ Nanoparticles with Tunable Magnetic Properties via Oleic Acid Based Solvothermal Synthesis for Application in Electronic Devices. **ACS Applied Nano Materials**, [*s. l.*], v. 2, n. 4, p. 1828–1843, 26 Apr. 2019.

ARANA-PEÑA, Sara; LOKHA, Yuliya; FERNÁNDEZ-LAFUENTE, Roberto. Immobilization on Octyl-Agarose Beads and Some Catalytic Features of Commercial Preparations of Lipase a from *Candida Antarctica* (Novocor ADL): Comparison with Immobilized Lipase B from *Candida Antarctica*. **Biotechnology Progress**, [*s. l.*], v. 35, n. 1, p. e2735, 1 Jan. 2019. Disponível em: http://doi.wiley.com/10.1002/btpr.2735. Acesso em: 13 oct. 2020.

BABAEI, Ali Akbar *et al.* Comparative Treatment of Textile Wastewater by Adsorption, Fenton, UV-Fenton and US-Fenton Using Magnetic Nanoparticles-Functionalized Carbon (MNPs@C). **Journal of Industrial and Engineering Chemistry**, [*s. l.*], v. 56, p. 163–174, 25 Dec. 2017.

BAGBI, Yana *et al.* Lead and Chromium Adsorption from Water Using L-Cysteine Functionalized Magnetite (Fe_3O_4) Nanoparticles. **Scientific Reports 2017 7:1**, [*s. l.*], v. 7, n. 1, p. 1–15, 9 Aug. 2017. Disponível em: https://www.nature.com/articles/s41598-017-03380-x. Acesso em: 28 jun. 2023.

BARBOSA, Felipe Fernandes *et al.* Synthesis of the Fe–Co Alloy from Hybrid Spheres Using Carboxymethylcellulose as Template and Its Application in Catalysis. **Materials Chemistry and Physics**, [*s. l.*], v. 242, p. 122550, 15 Feb. 2020.

BARBOSA, Felipe Fernandes; PERGHER, Sibele B.C.; BRAGA, Tiago Pinheiro. Synthesis of Highly Stable FeCo Alloy Encapsulated in Organized Carbon from Ethylbenzene Using H_2, CH_4, C_2H_4 Generated in Situ. **Journal of Alloys and Compounds**, [*s. l.*], v. 772, p. 625–636, 25 Jan. 2019.

BARBOSA, J.S. *et al.* Ultrafast Sonochemistry-Based Approach to Coat TiO_2 Commercial Particles for Sunscreen Formulation. **Ultrasonics Sonochemistry**, [*s. l.*], v. 48, p. 340–348, 1 Nov. 2018. Disponível em: https://www.sciencedirect.com/science/article/pii/S1350417718306643?via%3Dihub. Acesso em: 14 sep. 2019.

BARBOSA, Oveimar *et al.* Strategies for the One-Step Immobilization–Purification of Enzymes as Industrial Biocatalysts. **Biotechnology Advances**, [*s. l.*], v. 33, n. 5, p. 435–456, 1 Sep. 2015.

BASHIR, Arshid *et al.* Magnetically Recyclable L-Cysteine Capped Fe_3O_4 Nanoadsorbent: A Promising PH Guided Removal of Pb(II), Zn(II) and $HCrO_4^-$ Contaminants. **Journal of Environmental Chemical Engineering**, [*s. l.*], v. 9, n. 5, p. 105880, 1 Oct. 2021.

BEZ, R. *et al.* Comparative Study of Nanoparticles $Fe_{100-x}Co_x$ Alloy Synthesized by High Energy Ball Milling and by Polyol Process. **Journal of Superconductivity and Novel Magnetism**. [s.l.]: Springer New York LLC. Disponível em: https://link.springer.com/article/10.1007/s10948-015-3229-9. Acesso em: 16 apr. 2021. , 1 Dec. 2015

BEZBRADICA, Dejan I.; MATEO, Cesar; GUISAN, Jose M. Novel Support for Enzyme Immobilization Prepared by Chemical Activation with Cysteine and Glutaraldehyde. **Journal of Molecular Catalysis B: Enzymatic**, [*s. l.*], v. 102, p. 218–224, 1 Apr. 2014.

BEZERRA, Rayanne M. *et al.* Design of a Lipase-Nano Particle Biocatalysts and Its Use in the Kinetic Resolution of Medicament Precursors. **Biochemical Engineering Journal**, [*s. l.*], v. 125, p. 104–115, 15 Sep. 2017.

BIESINGER, Mark C. *et al.* Resolving Surface Chemical States in XPS Analysis of First Row Transition Metals, Oxides and Hydroxides: Cr, Mn, Fe, Co and Ni. **Applied Surface Science**, [*s. l.*], v. 257, n. 7, p. 2717–2730, 15 Jan. 2011.

BORTHAKUR, Sukanya; SAIKIA, Lakshi. $ZnFe_2O_4$@g-C_3N_4 Nanocomposites: An Efficient Catalyst for Fenton-like Photodegradation of Environmentally Pollutant Rhodamine B. **Journal of Environmental Chemical Engineering**, [*s. l.*], v. 7, n. 2, p. 103035, 1 Apr. 2019.

BRADFORD, Marion M. A Rapid and Sensitive Method for the Quantitation of Microgram Quantities of Protein Utilizing the Principle of Protein-Dye Binding. **Analytical Biochemistry**, [*s. l.*], v. 72, n. 1–2, p. 248–254, 7 May 1976.

BRANDÃO JÚNIOR, João *et al.* Performance of Eversa Transform 2.0 Lipase in Ester Production Using Babassu Oil (Orbignya Sp.) and Tucuman Oil (Astrocaryum Vulgar): A Comparative Study between Liquid and Immobilized Forms in Fe_3O_4 Nanoparticles. **Catalysts 2023**, [*s. l.*], v. 13, n. 3, p. 571, 11 Mar. 2023. Disponível em: https://www.mdpi.com/2073-4344/13/3/571/htm. Acesso em: 22 nov. 2023.

BRITOS, Tatiane N. *et al.* In Vivo Evaluation of Thiol-Functionalized Superparamagnetic Iron Oxide Nanoparticles. **Materials Science and Engineering: C**, [*s. l.*], v. 99, p. 171–179, 1 Jun. 2019.

CAMPOS, Alex Fabiano Cortez *et al.* Reusable Cysteine-Ferrite-Based Magnetic Nanopowders for Removal of Lead Ions from Water. **Materials Research**, [*s. l.*], v. 24, n. 4, p. e20210217, 27 Aug. 2021. Disponível em: https://www.scielo.br/j/mr/a/Njb4wWB7YYPNvXfvWH3XxNS/?lang=en. Acesso em: 28 jun. 2023.

CAO, Jiao *et al.* Peroxymonosulfate Activation of Magnetic Co Nanoparticles Relative to an N-Doped Porous Carbon under Confinement: Boosting Stability and Performance. **Separation and Purification Technology**, [*s. l.*], v. 250, p. 117237, 1 Nov. 2020.

CARROLL, Kyler J. *et al.* Preparation of Elemental Cu and Ni Nanoparticles by the Polyol Method: An Experimental and Theoretical Approach. **Journal of Physical Chemistry C**, [*s. l.*], v. 115, n. 6, p. 2656–2664, 17 Feb. 2011. Disponível em: https://pubs.acs.org/sharingguidelines. Acesso em: 15 apr. 2021.

CARVALHO, Tamires *et al.* Simple Physical Adsorption Technique to Immobilize Yarrowia Lipolytica Lipase Purified by Different Methods on Magnetic Nanoparticles: Adsorption Isotherms and Thermodynamic Approach. **International Journal of Biological Macromolecules**, [*s. l.*], v. 160, p. 889–902, 1 Oct. 2020.

CAVALCANTE, Antônio Luthierre Gama *et al.* Chemical Modification of Clay Nanocomposites for the Improvement of the Catalytic Properties of Lipase A from Candida Antarctica. **Process Biochemistry**, [*s. l.*], v. 120, p. 1–14, 1 Sep. 2022.

ÇELIK, Özer; FIRAT, Tezer. Synthesis of FeCo Magnetic Nanoalloys and Investigation of Heating Properties for Magnetic Fluid Hyperthermia. **Journal of Magnetism and Magnetic Materials**, [*s. l.*], v. 456, p. 11–16, 15 Jun. 2018.

CHANDRA, Prem *et al.* Microbial Lipases and Their Industrial Applications: A Comprehensive Review. **Microbial Cell Factories**, [*s. l.*], v. 19, n. 1, p. 1–42, 26 Aug. 2020. Disponível em: https://microbialcellfactories.biomedcentral.com/articles/10.1186/s12934-020-01428-8. Acesso em: 20 sep. 2023.

CHANGMAI, Bishwajit *et al.* A Novel Citrus Sinensis Peel Ash Coated Magnetic Nanoparticles as an Easily Recoverable Solid Catalyst for Biodiesel Production. **Fuel**, [*s. l.*], v. 286, p. 119447, 15 Feb. 2021.

CHAUBEY, Girija S. *et al.* Synthesis and Stabilization of FeCo Nanoparticles. **Journal of the American Chemical Society**, [*s. l.*], v. 129, n. 23, p. 7214–7215, 13 Jun. 2007. Disponível em: http://pubs.acs.org. Acesso em: 19 apr. 2021.

CHEN, Changlun *et al.* Synthesis of Ag Nanoparticles Decoration on Magnetic Carbonized Polydopamine Nanospheres for Effective Catalytic Reduction of Cr(VI). **Journal of Colloid and Interface Science**, [*s. l.*], v. 526, p. 1–8, 15 Sep. 2018.

CHEN, Ning *et al.* Cysteine-Modified Poly(Glycidyl Methacrylate) Grafted onto Silica Nanoparticles: New Supports for Significantly Enhanced Performance of Immobilized Lipase. **Biochemical Engineering Journal**, [*s. l.*], v. 145, p. 137–144, 15 May 2019.

CHEN, Tianju *et al.* Oxygen-Enriched Gasification of Lignocellulosic Biomass: Syngas Analysis, Physicochemical Characteristics of the Carbon-Rich Material and Its Utilization as an Anode in Lithium Ion Battery. **Energy**, [*s. l.*], v. 212, p. 118771, 1 Dec. 2020.

CHEN, Yong *et al.* Fenton-like Degradation of Sulfamerazine at Nearly Neutral PH Using Fe-Cu-CNTs and Al^0-CNTs for in-Situ Generation of $H_2O_2/OH/O_2^-$. **Chemical Engineering**

Journal, [*s. l.*], v. 396, p. 125329, 15 Sep. 2020.

CHENG, Siyao *et al.* Highly Efficient Removal of Antibiotic from Biomedical Wastewater Using Fenton-like Catalyst Magnetic Pullulan Hydrogels. **Carbohydrate Polymers**, [*s. l.*], v. 262, p. 117951, 15 Jun. 2021.

COHEN, Hua; GEDANKEN, Aharon; ZHONG, Ziyi. One-Step Synthesis and Characterization of Ultrastable and Amorphous Fe_3O_4 Colloids Capped with Cysteine Molecules. **Journal of Physical Chemistry C**, [*s. l.*], v. 112, n. 39, p. 15429–15438, 2 Oct. 2008.

COPÉRET, Christophe *et al.* Homogeneous and Heterogeneous Catalysis: Bridging the Gap through Surface Organometallic Chemistry. **Angewandte Chemie International Edition**, [*s. l.*], v. 42, n. 2, p. 156–181, 13 Jan. 2003. Disponível em: https://onlinelibrary.wiley.com/doi/full/10.1002/anie.200390072. Acesso em: 8 nov. 2023.

DANTAS, J. *et al.* Biodiesel Production Evaluating the Use and Reuse of Magnetic Nanocatalysts $Ni_{0.5}Zn_{0.5}Fe_2O_4$ Synthesized in Pilot-Scale. **Arabian Journal of Chemistry**, [*s. l.*], v. 13, n. 1, p. 3026–3042, 1 Jan. 2020.

DAS, Tushar Kanti *et al.* In-Situ Synthesis of Magnetic Nanoparticle Immobilized Heterogeneous Catalyst through Mussel Mimetic Approach for the Efficient Removal of Water Pollutants. **Colloid and Interface Science Communications**, [*s. l.*], v. 33, p. 100218, 1 Nov. 2019.

DENG, Jing *et al.* Synthesis of Magnetic $CoFe_2O_4$/Ordered Mesoporous Carbon Nanocomposites and Application in Fenton-like Oxidation of Rhodamine B. **Environmental Science and Pollution Research**, [*s. l.*], v. 24, n. 16, p. 14396–14408, 1 Jun. 2017. Disponível em: https://link.springer.com/article/10.1007/s11356-017-8941-5. Acesso em: 30 nov. 2022.

DINDARLOO INALOO, Iman *et al.* Air-Stable Fe_3O_4@SiO_2-EDTA-Ni(0) as an Efficient Recyclable Magnetic Nanocatalyst for Effective Suzuki-Miyaura and Heck Cross-Coupling via Aryl Sulfamates and Carbamates. **Applied Organometallic Chemistry**, [*s. l.*], v. 34, n. 8, p. e5662, 1 Aug. 2020a. Disponível em: https://onlinelibrary.wiley.com/doi/full/10.1002/aoc.5662. Acesso em: 26 nov. 2023.

DINDARLOO INALOO, Iman *et al.* Nickel(II) Nanoparticles Immobilized on EDTA-Modified Fe_3O_4@SiO_2 Nanospheres as Efficient and Recyclable Catalysts for Ligand-Free Suzuki-Miyaura Coupling of Aryl Carbamates and Sulfamates. **ACS Omega**, [*s. l.*], v. 5, n. 13, p. 7406–7417, 7 Apr. 2020b. Disponível em: https://pubs.acs.org/doi/full/10.1021/acsomega.9b04450. Acesso em: 27 nov. 2023.

DING, Yaobin *et al.* Nonradicals Induced Degradation of Organic Pollutants by Peroxydisulfate (PDS) and Peroxymonosulfate (PMS): Recent Advances and Perspective. **Science of the Total Environment**. [S.l.]: Elsevier B.V. , 15 Apr. 2021

DO NASCIMENTO, Carlos Pedro G. *et al.* Redox Cycling of Copper Mediated by Hydrazine: Efficient Catalyst Systems for Oxidative Degradation of Rhodamine B. **Journal of Environmental Science and Health, Part A**, [*s. l.*], v. 56, n. 8, p. 849–860, 2021.

Disponível em: https://www.tandfonline.com/doi/abs/10.1080/10934529.2021.1932170. Acesso em: 30 nov. 2023.

DODDS, John *et al.* The Effect of Ultrasound on Crystallisation-Precipitation Processes: Some Examples and a New Segregation Model. **Particle & Particle Systems Characterization**, [*s. l.*], v. 24, n. 1, p. 18–28, 1 Jun. 2007. Disponível em: https://onlinelibrary.wiley.com/doi/full/10.1002/ppsc.200601046. Acesso em: 20 nov. 2023.

DONG, H.; CHEN, Y. C.; FELDMANN, C. Polyol Synthesis of Nanoparticles: Status and Options Regarding Metals, Oxides, Chalcogenides, and Non-Metal Elements. **Green Chemistry**, [*s. l.*], v. 17, n. 8, p. 4107–4132, 1 Aug. 2015. Disponível em: www.rsc.org/greenchem. Acesso em: 14 apr. 2021.

DOS SANTOS, Jose C.S. *et al.* Versatility of Divinylsulfone Supports Permits the Tuning of CALB Properties during Its Immobilization. **RSC Advances**, [*s. l.*], v. 5, n. 45, p. 35801–35810, 16 Apr. 2015. Disponível em: https://pubs.rsc.org/en/content/articlehtml/2015/ra/c5ra03798k. Acesso em: 18 oct. 2023.

DU, Yunchen *et al.* Magnetic $CoFe_2O_4$ Nanoparticles Supported on Titanate Nanotubes ($CoFe_2O_4$/TNTs) as a Novel Heterogeneous Catalyst for Peroxymonosulfate Activation and Degradation of Organic Pollutants. **Journal of Hazardous Materials**, [*s. l.*], v. 308, p. 58–66, 5 May 2016.

DUAN, Meng *et al.* Recent Progress in Magnetic Nanoparticles: Synthesis, Properties, and Applications. **Nanotechnology**, [*s. l.*], v. 29, n. 45, p. 452001, 9 Nov. 2018. Disponível em: http://stacks.iop.org/0957-4484/29/i=45/a=452001?key=crossref.7fcd9c1286f919bc810f161799c8e97c. Acesso em: 3 jul. 2019.

DUTT, Aditya; UPADHYAY, Lata Sheo Bachan. Synthesis of Cysteine-Functionalized Silver Nanoparticles Using Green Tea Extract with Application for Lipase Immobilization. **Analytical Letters**, [*s. l.*], v. 51, n. 7, p. 1071–1086, 3 May 2018. Disponível em: https://www.tandfonline.com/doi/full/10.1080/00032719.2017.1367399. Acesso em: 16 oct. 2020.

EASTERDAY, R. *et al.* Design of Ruthenium/Iron Oxide Nanoparticle Mixtures for Hydrogenation of Nitrobenzene. **Catalysis Science & Technology**, [*s. l.*], v. 5, n. 3, p. 1902–1910, 26 Feb. 2015. Disponível em: https://pubs.rsc.org/en/content/articlehtml/2015/cy/c4cy01277a. Acesso em: 25 nov. 2023.

ELLMAN, George L. Tissue Sulfhydryl Groups. **Archives of Biochemistry and Biophysics**, [*s. l.*], v. 82, n. 1, p. 70–77, 1 May 1959.

ES'HAGHZADE, Zahra *et al.* Facile Synthesis of Fe_3O_4 Nanoparticles via Aqueous Based Electro Chemical Route for Heterogeneous Electro-Fenton Removal of Azo Dyes. **Journal of the Taiwan Institute of Chemical Engineers**, [*s. l.*], v. 71, p. 91–105, 1 Feb. 2017.

EVRARD, Quentin *et al.* Sonocrystallization as an Efficient Way to Control the Size, Morphology, and Purity of Coordination Compound Microcrystallites: Application to a Single-Chain Magnet. **Inorganic Chemistry**, [*s. l.*], v. 59, n. 13, p. 9215–9226, 6 Jul. 2020.

Disponível em: https://pubs.acs.org/doi/full/10.1021/acs.inorgchem.0c01126. Acesso em: 20 nov. 2023.

FAN, Hong Lei *et al.* Continuous Preparation of Fe_3O_4 Nanoparticles Combined with Surface Modification by L-Cysteine and Their Application in Heavy Metal Adsorption. **Ceramics International**, [*s. l.*], v. 42, n. 3, p. 4228–4237, 15 Feb. 2016.

FAN, Yanan *et al.* $CoMoO_4$ as a Novel Heterogeneous Catalyst of Peroxymonosulfate Activation for the Degradation of Organic Dyes. **RSC Advances**, [*s. l.*], v. 7, n. 57, p. 36193–36200, 17 Jul. 2017. Disponível em: https://pubs.rsc.org/en/content/articlehtml/2017/ra/c7ra04761d. Acesso em: 6 apr. 2021.

FANG, Gang *et al.* Immobilization of Pectinase onto $Fe_3O_4@SiO_2–NH_2$ and Its Activity and Stability. **International Journal of Biological Macromolecules**, [*s. l.*], v. 88, p. 189–195, 1 Jul. 2016.

FENTON, H. J.H. LXXIII.—Oxidation of Tartaric Acid in Presence of Iron. **Journal of the Chemical Society, Transactions**, [*s. l.*], v. 65, n. 0, p. 899–910, 1 Jan. 1894. Disponível em: https://pubs.rsc.org/en/content/articlehtml/1894/ct/ct8946500899. Acesso em: 21 nov. 2023.

FERRANDO, Riccardo; JELLINEK, Julius; JOHNSTON, Roy L. Nanoalloys: From Theory to Applications of Alloy Clusters and Nanoparticles. **Chemical Reviews**. [s.l.]: American Chemical Society. Disponível em: https://pubs.acs.org/sharingguidelines. Acesso em: 13 apr. 2021. , 2008

FIEVET, F. *et al.* The Polyol Process: A Unique Method for Easy Access to Metal Nanoparticles with Tailored Sizes, Shapes and Compositions. **Chemical Society Reviews**, v. 47, n. 14, p. 5187–5233, 21 Jul. 2018. Disponível em: https://pubs.rsc.org/en/content/articlehtml/2018/cs/c7cs00777a. Acesso em: 26 jan. 2021.

FIEVET, F.; LAGIER, J. P.; FIGLARZ, M. Preparing Monodisperse Metal Powders in Micrometer and Submicrometer Sizes by the Polyol Process. **MRS Bulletin**, [*s. l.*], v. 14, n. 12, p. 29–34, 1989. Disponível em: https://doi.org/10.1557/S0883769400060930. Acesso em: 14 apr. 2021.

FORTES, Cristiano C.S. *et al.* Optimization of Enzyme Immobilization on Functionalized Magnetic Nanoparticles for Laccase Biocatalytic Reactions. **Chemical Engineering and Processing: Process Intensification**, [*s. l.*], v. 117, p. 1–8, 1 Jul. 2017.

GAETA, Michele *et al.* Magnetism of Materials: Theory and Practice in Magnetic Resonance Imaging. **Insights into Imaging**, v. 12, n. 1, p. 1–18, 1 Dec. 2021. Disponível em: https://insightsimaging.springeropen.com/articles/10.1186/s13244-021-01125-z. Acesso em: 18 nov. 2023.

GALVÃO, W. S. *et al.* Cubic Superparamagnetic Nanoparticles of $NiFe_2O_4$ via Fast Microwave Heating. **Journal of Nanoparticle Research**, [*s. l.*], v. 16, n. 12, p. 2803, 23 Dec. 2014. Disponível em: http://link.springer.com/10.1007/s11051-014-2803-6. Acesso em: 4 jul. 2019.

GALVÃO, W. S. *et al.* Novel Nanohybrid Biocatalyst: Application in the Kinetic Resolution

of Secondary Alcohols. **Journal of Materials Science**, [*s. l.*], v. 53, n. 20, p. 14121–14137, 1 Oct. 2018. Disponível em: https://link.springer.com/article/10.1007/s10853-018-2641-5. Acesso em: 22 nov. 2023.

GALVÃO, Wesley S. *et al.* Super-Paramagnetic Nanoparticles with Spinel Structure: A Review of Synthesis and Biomedical Applications. **Solid State Phenomena**, [*s. l.*], v. 241, p. 139–176, Oct. 2015. Disponível em: http://www.scientific.net/SSP.241.139. Acesso em: 28 jun. 2017.

GASIM, Mohamed Faisal *et al.* Can Biochar and Hydrochar Be Used as Sustainable Catalyst for Persulfate Activation? **Chemosphere**, [*s. l.*], v. 287, p. 132458, 1 Jan. 2022.

GEBRE, Shushay Hagos. Recent Developments of Supported and Magnetic Nanocatalysts for Organic Transformations: An up-to-Date Review. **Applied Nanoscience**, [*s. l.*], v. 13, n. 1, p. 15–63, 27 May 2021. Disponível em: https://link.springer.com/article/10.1007/s13204-021-01888-3. Acesso em: 7 nov. 2023.

GHAMARI KARGAR, Pouya; BAGHERZADE, Ghodsieh; ESHGHI, Hossein. Design and Synthesis of Magnetic Fe_3O_4@NFC-ImSalophCu Nanocatalyst Based on Cellulose Nanofibers as a New and Highly Efficient, Reusable, Stable and Green Catalyst for the Synthesis of 1,2,3-Triazoles. **RSC Advances**, [*s. l.*], v. 10, n. 54, p. 32927–32937, 1 Sep. 2020. Disponível em: https://pubs.rsc.org/en/content/articlehtml/2020/ra/d0ra06251k. Acesso em: 28 nov. 2023.

GHAMARI KARGAR, Pouya; LEN, Christophe; LUQUE, Rafael. Cu/Cellulose-Modified Magnetite Nanocomposites as a Highly Active and Selective Catalyst for Ultrasound-Promoted Aqueous O-Arylation Ullmann and Sp-Sp2 Sonogashira Cross-Coupling Reactions. **Sustainable Chemistry and Pharmacy**, [*s. l.*], v. 27, p. 100672, 1 Jun. 2022.

GHANBARI, Farshid; MORADI, Mahsa. Application of Peroxymonosulfate and Its Activation Methods for Degradation of Environmental Organic Pollutants: Review. **Chemical Engineering Journal**, [*s. l.*], v. 310, p. 41–62, 15 Feb. 2017.

GHAVIDEL, Hassan; MIRZA, Behrooz; SOLEIMANI-AMIRI, Somayeh. A Novel, Efficient, and Recoverable Basic Fe_3O_4@C Nano-Catalyst for Green Synthesis of 4H-Chromenes in Water via One-Pot Three Component Reactions. **Polycyclic Aromatic Compounds**, [*s. l.*], v. 41, n. 3, p. 604–625, 2021. Disponível em: https://www.tandfonline.com/doi/abs/10.1080/10406638.2019.1607413. Acesso em: 22 nov. 2023.

GHOBADI, Massoud *et al.* Nanomagnetic Reusable Catalysts in Organic Synthesis. **Synthetic Communications**, [*s. l.*], v. 51, n. 5, p. 647–669, 2021. Disponível em: https://www.tandfonline.com/doi/abs/10.1080/00397911.2020.1819328. Acesso em: 8 nov. 2023.

GHORBANI-CHOGHAMARANI, Arash; MOHAMMADI, Masoud; TAHERINIA, Zahra. $(ZrO)_2Fe_2O_5$ as an Efficient and Recoverable Nanocatalyst in C–C Bond Formation. **Journal of the Iranian Chemical Society**, [*s. l.*], v. 16, n. 2, p. 411–421, 14 Feb. 2019. Disponível em: https://link.springer.com/article/10.1007/s13738-018-1522-9. Acesso em: 22 nov. 2023.

GILROY, Kyle D. *et al.* Bimetallic Nanocrystals: Syntheses, Properties, and Applications. **Chemical Reviews**, v. 116, n. 18, p. 10414–10472, 28 Sep. 2016. Disponível em: https://pubs.acs.org/sharingguidelines. Acesso em: 13 apr. 2021.

GONG, Cheng *et al.* Heterogeneous Activation of Peroxymonosulfate by Fe-Co Layered Doubled Hydroxide for Efficient Catalytic Degradation of Rhoadmine B. **Chemical Engineering Journal**, [*s. l.*], v. 321, p. 222–232, 1 Aug. 2017.

GONG, Zhengjie; MA, Tao; LIANG, Feng. Syntheses of Magnetic Blackberry-like Ni@Cu@Pd Nanoparticles for Efficient Catalytic Reduction of Organic Pollutants. **Journal of Alloys and Compounds**, [*s. l.*], v. 873, p. 159802, 25 Aug. 2021.

GRANDVIEW RESEARCH. **Catalyst Market Size, Share & Growth Analysis Report, 2030**. San Francisco, USA: [s.n.], 2023. Disponível em: https://www.grandviewresearch.com/industry-analysis/catalyst-market. Acesso em: 8 nov. 2023.

GRAZÚ, Valeria *et al.* Stabilization of Enzymes by Multipoint Immobilization of Thiolated Proteins on New Epoxy-Thiol Supports. **Biotechnology and Bioengineering**, [*s. l.*], v. 90, n. 5, p. 597–605, 5 Jun. 2005. Disponível em: https://onlinelibrary.wiley.com/doi/full/10.1002/bit.20452. Acesso em: 17 oct. 2023.

GRIBANOV, N. M. *et al.* Physico-Chemical Regularities of Obtaining Highly Dispersed Magnetite by the Method of Chemical Condensation. **Journal of Magnetism and Magnetic Materials**, [*s. l.*], v. 85, n. 1–3, p. 7–10, 1 Apr. 1990.

GUBIN, Sergey P. **Magn. Nanoparticles**. [s.l.]: Wiley, 2009. Disponível em: https://onlinelibrary.wiley.com/doi/book/10.1002/9783527627561. Acesso em: 13 apr. 2021.

GUISAN, Jose M. *et al.* Enzyme Immobilization Strategies for the Design of Robust and Efficient Biocatalysts. **Current Opinion in Green and Sustainable Chemistry**, [*s. l.*], v. 35, p. 100593, 1 Jun. 2022.

HADDAD, P. S. *et al.* Synthesis, Characterization and Cytotoxicity Evaluation of Nitric Oxide-Iron Oxide Magnetic Nanoparticles. **Journal of Physics: Conference Series**, [*s. l.*], v. 617, n. 1, p. 012022, 1 May 2015. Disponível em: https://iopscience.iop.org/article/10.1088/1742-6596/617/1/012022. Acesso em: 19 oct. 2023.

HALILU, Ahmed *et al.* Highly Selective Hydrogenation of Biomass-Derived Furfural into Furfuryl Alcohol Using a Novel Magnetic Nanoparticles Catalyst. **Energy and Fuels**, [*s. l.*], v. 30, n. 3, p. 2216–2226, 17 Mar. 2016. Disponível em: https://pubs.acs.org/doi/full/10.1021/acs.energyfuels.5b02826. Acesso em: 22 nov. 2023.

HARISH, Vancha *et al.* Cutting-Edge Advances in Tailoring Size, Shape, and Functionality of Nanoparticles and Nanostructures: A Review. **Journal of the Taiwan Institute of Chemical Engineers**, [*s. l.*], v. 149, p. 105010, 1 Aug. 2023.

HASSAN, Muhammad *et al.* Energy-Efficient Degradation of Antibiotics in Microbial Electro-Fenton System Catalysed by M-Type Strontium Hexaferrite Nanoparticles. **Chemical Engineering Journal**, [*s. l.*], v. 380, p. 122483, 15 Jan. 2020.

HOU, Jifei *et al.* Recent Advances in Cobalt-Activated Sulfate Radical-Based Advanced Oxidation Processes for Water Remediation: A Review. **Science of the Total Environment**. [S.l.]: Elsevier B.V. , 20 May 2021

HOU, Yanglong; SELLMYER, David J. **Magn. Nanomater. - Fundam. Synth. Appl.** 1. ed. Weinheim, Germany: Wiley-VCH Verlag GmbH & Co. KGaA, 2017. Disponível em: http://doi.wiley.com/10.1002/9783527803255. Acesso em: 21 apr. 2021.

HUANG, Pingquan *et al.* Palladium Nanoparticles Anchored on Thiol Functionalized Xylose Hydrochar Microspheres: An Efficient Heterogeneous Catalyst for Suzuki Cross-Coupling Reactions. **Catalysis Letters**, [*s. l.*], v. 150, n. 4, p. 1011–1019, 1 Apr. 2020. Disponível em: https://doi.org/10.1007/s10562-019-02984-4. Acesso em: 28 jan. 2021.

I. SCHWERDT, Jose *et al.* Magnetic Field-Assisted Gene Delivery: Achievements and Therapeutic Potential. **Current Gene Therapy**, [*s. l.*], v. 12, n. 2, p. 116–126, 1 Mar. 2012. Disponível em: http://www.eurekaselect.com/openurl/content.php?genre=article&issn=1566-5232&volume=12&issue=2&spage=116. Acesso em: 5 feb. 2021.

ISARI, Ali Akbar *et al.* Photocatalytic Degradation of Rhodamine B and Real Textile Wastewater Using Fe-Doped TiO_2 Anchored on Reduced Graphene Oxide (Fe-TiO_2 /RGO): Characterization and Feasibility, Mechanism and Pathway Studies. **Applied Surface Science**, [*s. l.*], v. 462, p. 549–564, 31 Dec. 2018.

JAMES, Jayasundar J. *et al.* Insights from Molecular Dynamics Simulations into PH-dependent Enantioselective Hydrolysis of Ibuprofen Esters by Candida Rugosa Lipase. **Protein Engineering, Design and Selection**, [*s. l.*], v. 16, n. 12, p. 1017–1024, 1 Dec. 2003. Disponível em: https://dx.doi.org/10.1093/protein/gzg135. Acesso em: 19 oct. 2023.

JANG, Jung-tak *et al.* Critical Enhancements of MRI Contrast and Hyperthermic Effects by Dopant-Controlled Magnetic Nanoparticles. **Angewandte Chemie International Edition**, [*s. l.*], v. 48, n. 7, p. 1234–1238, 2 Feb. 2009. Disponível em: http://doi.wiley.com/10.1002/anie.200805149. Acesso em: 6 dec. 2019.

JEGANNATHAN, Kenthorai Raman; NIELSEN, Per Henning. Environmental Assessment of Enzyme Use in Industrial Production – a Literature Review. **Journal of Cleaner Production**, [*s. l.*], v. 42, p. 228–240, 1 Mar. 2013.

JIANG, Yanjun *et al.* Virus-like Organosilica Nanoparticles for Lipase Immobilization: Characterization and Biocatalytic Applications. **Biochemical Engineering Journal**, [*s. l.*], v. 144, p. 125–134, 15 Apr. 2019.

JOSEYPHUS, R. Justin *et al.* Size Controlled Fe Nanoparticles through Polyol Process and Their Magnetic Properties. **Materials Chemistry and Physics**, [*s. l.*], v. 123, n. 2–3, p. 487–493, 1 Oct. 2010.

JOSEYPHUS, R.J. *et al.* Designed Synthesis of Cobalt and Its Alloys by Polyol Process. **Journal of Solid State Chemistry**, [*s. l.*], v. 180, n. 11, p. 3008–3018, 1 Nov. 2007. Disponível em: https://www.sciencedirect.com/science/article/pii/S002245960700299X. Acesso em: 5 jul. 2019.

JOSHIBA, G. Janet *et al.* Investigation of Magnetic Silica Nanocomposite Immobilized Pseudomonas Fluorescens as a Biosorbent for the Effective Sequestration of Rhodamine B from Aqueous Systems. **Environmental Pollution**, [*s. l.*], v. 269, p. 116173, 15 Jan. 2021.

KALANTARI, Fatemeh *et al.* Magnetic Nanoparticles Functionalized with Copper Hydroxyproline Complexes as an Efficient, Recoverable, and Recyclable Nanocatalyst: Synthesis and Its Catalytic Application in a Tandem Knoevenagel-Michael Cyclocondensation Reaction. **Inorganic Chemistry**, [*s. l.*], v. 60, n. 19, p. 15010–15023, 4 Oct. 2021. Disponível em: https://pubs.acs.org/doi/abs/10.1021/acs.inorgchem.1c02470. Acesso em: 28 nov. 2023.

KALANTARI, Fatemeh *et al.* Proline-Cu Complex Based 1,3,5-Triazine Coated on Fe_3O_4 Magnetic Nanoparticles: A Nanocatalyst for the Knoevenagel Condensation of Aldehyde with Malononitrile. **ACS Applied Nano Materials**, [*s. l.*], v. 5, n. 2, p. 1783–1797, 25 Feb. 2022. Disponível em: https://pubs.acs.org/doi/abs/10.1021/acsanm.1c03169. Acesso em: 28 nov. 2023.

KALYAN KAMAL, S. S. *et al.* Synthesis of Cobalt Nanoparticles by a Modified Polyol Process Using Cobalt Hydrazine Complex. **Journal of Alloys and Compounds**, [*s. l.*], v. 474, n. 1–2, p. 214–218, 17 Apr. 2009.

KANG, Shimin *et al.* Characterization of Hydrochars Produced by Hydrothermal Carbonization of Lignin, Cellulose, d-Xylose, and Wood Meal. 4 Jul. 2012, [S.l.]: American Chemical Society, 4 Jul. 2012. p. 9023–9031. Disponível em: https://pubs.acs.org/sharingguidelines. Acesso em: 28 jan. 2021.

KARAOGLU, E.; BAYKAL, A. CoFe2O4–Pd (0) Nanocomposite: Magnetically Recyclable Catalyst. **Journal of Superconductivity and Novel Magnetism**, [*s. l.*], v. 27, n. 9, p. 2041–2047, 1 Sep. 2014. Disponível em: https://link.springer.com/article/10.1007/s10948-014-2522-3. Acesso em: 20 nov. 2023.

KARIMI, Sabah; SEIDI, Farzad; *et al.* Catalytic Dehydration of Fructose into 5-Hydroxymethylfurfural by Propyl Sulfonic Acid Functionalized Magnetic Graphene Oxide Nanocomposite. **Renewable Energy**, [*s. l.*], v. 180, p. 132–139, 1 Dec. 2021.

KARIMI, Sabah; SHEKAARI, Hemayat; *et al.* Solvent-Free Production of 5-Hydroxymethylfurfural from Deep Eutectic Substrate Reaction Mixtures over a Magnetically Recoverable Solid Acid Catalyst. **ACS Sustainable Chemistry and Engineering**, [*s. l.*], v. 9, n. 1, p. 326–336, 11 Jan. 2021. Disponível em: https://pubs.acs.org/doi/abs/10.1021/acssuschemeng.0c07272. Acesso em: 28 nov. 2023.

KARIPOTH, Prakash *et al.* Magnetic Properties of FeCo Alloy Nanoparticles Synthesized through Instant Chemical Reduction. **Journal of Applied Physics**, [*s. l.*], v. 120, n. 12, p. 123906, 28 Sep. 2016. Disponível em: http://aip.scitation.org/doi/10.1063/1.4962637. Acesso em: 5 jul. 2019.

KHASHEI SIUKI, Hossein; GHAMARI KARGAR, Pouya; BAGHERZADE, Ghodsieh. New Acetamidine Cu(II) Schiff Base Complex Supported on Magnetic Nanoparticles Pectin for the Synthesis of Triazoles Using Click Chemistry. **Scientific Reports**, [*s. l.*], v. 12, n. 1, p.

1–17, 8 Mar. 2022. Disponível em: https://www.nature.com/articles/s41598-022-07674-7. Acesso em: 28 nov. 2023.

KHOOBI, Mehdi *et al.* Polyethyleneimine-Modified Superparamagnetic Fe_3O_4 Nanoparticles for Lipase Immobilization: Characterization and Application. **Materials Chemistry and Physics**, [*s. l.*], v. 149–150, p. 77–86, 15 Jan. 2015.

KOHANTORABI, Mona; MOUSSAVI, Gholamreza; GIANNAKIS, Stefanos. A Review of the Innovations in Metal- and Carbon-Based Catalysts Explored for Heterogeneous Peroxymonosulfate (PMS) Activation, with Focus on Radical vs. Non-Radical Degradation Pathways of Organic Contaminants. **Chemical Engineering Journal**. [S.l.]: Elsevier B.V. , 1 May 2021

KOŁODZIEJCZAK-RADZIMSKA, Agnieszka; JESIONOWSKI, Teofil. A Novel Cysteine-Functionalized MxOy Material as Support for Laccase Immobilization and a Potential Application in Decolorization of Alizarin Red S. **Processes**, [*s. l.*], v. 8, n. 8, p. 885, 1 Aug. 2020. Disponível em: www.mdpi.com/journal/processes. Acesso em: 4 nov. 2020.

KUCHKINA, Nina V. *et al.* Polyphenylenepyridyl Dendrons with Functional Periphery and Focal Points: Syntheses and Applications. **Macromolecules**, [*s. l.*], v. 46, n. 15, p. 5890–5898, 13 Aug. 2013. Disponível em: https://pubs.acs.org/doi/full/10.1021/ma401043u. Acesso em: 25 nov. 2023.

LANDARANI-ISFAHANI, Amir *et al.* Xylanase Immobilized on Novel Multifunctional Hyperbranched Polyglycerol-Grafted Magnetic Nanoparticles: An Efficient and Robust Biocatalyst. **Langmuir**, [*s. l.*], v. 31, n. 33, p. 9219–9227, 25 Aug. 2015. Disponível em: https://pubs.acs.org/doi/full/10.1021/acs.langmuir.5b02004. Acesso em: 22 nov. 2023.

LI, Tong *et al.* Efficient Degradation of Rhodamine B by Magnetically Recoverable Fe_3O_4-Modified Ternary CoFeCu-Layered Double Hydroxides via Activating Peroxymonosulfate. **Journal of Environmental Sciences (China)**, [*s. l.*], v. 108, p. 188–200, 1 Oct. 2021.

LI, Xiaowan *et al.* Cobalt Ferrite Nanoparticles Supported on Drinking Water Treatment Residuals: An Efficient Magnetic Heterogeneous Catalyst to Activate Peroxymonosulfate for the Degradation of Atrazine. **Chemical Engineering Journal**, [*s. l.*], v. 367, p. 208–218, 1 Jul. 2019.

LI, Xinyuan *et al.* Size-Effect Induced Cation Redistribution on the Magnetic Properties of Well-Dispersed $CoFe_2O_4$ Nanocrystals. **Journal of Alloys and Compounds**, [*s. l.*], v. 841, p. 155710, 15 Nov. 2020.

LIANG, Jinping; FU, Ling. Activation of Peroxymonosulfate (PMS) by Co3O4 Quantum Dots Decorated Hierarchical C@Co3O4 for Degradation of Organic Pollutants: Kinetics and Radical-Nonradical Cooperation Mechanisms. **Applied Surface Science**, [*s. l.*], v. 563, p. 150335, 15 Oct. 2021.

LIU, Dongdong *et al.* Efficient Degradation of Rhodamine B in Water by $CoFe_2O_4/H_2O_2$ and $CoFe_2O_4$/PMS Systems: A Comparative Study. **Chemosphere**, [*s. l.*], v. 307, p. 135935, 1 Nov. 2022.

MAJIDI, Sima *et al.* Current Methods for Synthesis of Magnetic Nanoparticles. **Artificial Cells, Nanomedicine, and Biotechnology**, [*s. l.*], v. 44, n. 2, p. 722–734, 17 Feb. 2016. Disponível em: http://www.tandfonline.com/doi/full/10.3109/21691401.2014.982802. Acesso em: 2 jul. 2019.

MALEKI, Ali *et al.* Palladium-Decorated o-Phenylenediamine-Functionalized Fe_3O_4/SiO_2 Magnetic Nanoparticles: A Promising Solid-State Catalytic System Used for Suzuki–Miyaura Coupling Reactions. **Journal of Physics and Chemistry of Solids**, [*s. l.*], v. 136, p. 109200, 1 Jan. 2020.

MALEKI, Ali; VARZI, Z.; HASSANZADEH-AFRUZI, Fereshte. Preparation and Characterization of an Eco-Friendly $ZnFe_2O_4$@alginic Acid Nanocomposite Catalyst and Its Application in the Synthesis of 2-Amino-3-Cyano-4H-Pyran Derivatives. **Polyhedron**, [*s. l.*], v. 171, p. 193–202, 1 Oct. 2019.

MANZOLI, Maela *et al.* Microwave-Assisted Reductive Amination with Aqueous Ammonia: Sustainable Pathway Using Recyclable Magnetic Nickel-Based Nanocatalyst. **ACS Sustainable Chemistry and Engineering**, [*s. l.*], v. 7, n. 6, p. 5963–5974, 18 Mar. 2019. Disponível em: https://pubs.acs.org/doi/full/10.1021/acssuschemeng.8b06054. Acesso em: 28 nov. 2023.

MIAO, Changlin *et al.* Lipase Immobilization on Amino-Silane Modified Superparamagnetic Fe_3O_4 Nanoparticles as Biocatalyst for Biodiesel Production. **Fuel**, [*s. l.*], v. 224, p. 774–782, 15 Jul. 2018.

MOHAMMADI, Masoud; GHORBANI-CHOGHAMARANI, Arash. Complexation of Guanidino Containing L-Arginine with Nickel on Silica-Modified Hercynite MNPs: A Novel Catalyst for the Hantzsch Synthesis of Polyhydroquinolines and 2,3-Dihydroquinazolin-4(1H)-Ones. **Research on Chemical Intermediates**, [*s. l.*], v. 48, n. 6, p. 2641–2663, 1 Jun. 2022. Disponível em: https://link.springer.com/article/10.1007/s11164-022-04706-9. Acesso em: 28 nov. 2023.

MONTEIRO, R.R.C. Rodolpho R.C. *et al.* Improvement of Enzymatic Activity and Stability of Lipase A from Candida Antartica onto Halloysite Nanotubes with Taguchi Method for Optimized Immobilization. **Applied Clay Science**, [*s. l.*], v. 228, p. 106634, 1 Oct. 2022.

MONTEIRO, Rodolpho R. C. *et al.* Immobilization of Lipase A from Candida Antarctica onto Chitosan-Coated Magnetic Nanoparticles. **International Journal of Molecular Sciences**, [*s. l.*], v. 20, n. 16, p. 4018, 17 Aug. 2019. Disponível em: https://www.mdpi.com/1422-0067/20/16/4018. Acesso em: 22 jan. 2020.

MONTEIRO, Rodolpho R.C. *et al.* Biotechnological Relevance of the Lipase A from Candida Antarctica. **Catalysis Today**, [*s. l.*], 18 Mar. 2020.

MONTEIRO, Rodolpho R.C. *et al.* Ethyl Butyrate Synthesis Catalyzed by Lipases a and b from Candida Antarctica Immobilized onto Magnetic Nanoparticles. Improvement of Biocatalysts' Performance under Ultrasonic Irradiation. **International Journal of Molecular Sciences**, [*s. l.*], v. 20, n. 22, p. 5807, 2 Nov. 2019. Disponível em: https://www.mdpi.com/1422-0067/20/22/5807/htm. Acesso em: 28 jun. 2020.

MORADI, Parisa; HAJJAMI, Maryam. Magnetization of Graphene Oxide Nanosheets Using Nickel Magnetic Nanoparticles as a Novel Support for the Fabrication of Copper as a Practical, Selective, and Reusable Nanocatalyst in C–C and C–O Coupling Reactions. **RSC Advances**, [*s. l.*], v. 11, n. 42, p. 25867–25879, 27 Jul. 2021. Disponível em: https://pubs.rsc.org/en/content/articlehtml/2021/ra/d1ra03578a. Acesso em: 26 nov. 2023.

MORADI, Parisa; HAJJAMI, Maryam. Stabilization of Ruthenium on Biochar-Nickel Magnetic Nanoparticles as a Heterogeneous, Practical, Selective, and Reusable Nanocatalyst for the Suzuki C–C Coupling Reaction in Water. **RSC Advances**, [*s. l.*], v. 12, n. 21, p. 13523–13534, 28 Apr. 2022. Disponível em: https://pubs.rsc.org/en/content/articlehtml/2022/ra/d1ra09350a. Acesso em: 26 nov. 2023.

MOREIRA, Katerine S. *et al.* Lipase from Rhizomucor Miehei Immobilized on Magnetic Nanoparticles: Performance in Biodiesel Optimized Production by the Taguchi Method. **Frontiers in Bioengineering and Biotechnology**, [*s. l.*], v. 8, p. 693, 30 Jun. 2020.

MUTHUKUMAR, Harshiny *et al.* Immobilization of Xylose Reductase Enzyme on Cysteine-Functionalized Murraya Koenigii Mediated Magnetite Nanoparticles. **Materials Letters**, [*s. l.*], v. 261, p. 127125, 15 Feb. 2020.

NASROLLAHZADEH, Mahmoud; SAJADI, S. Mohammad. Preparation of Pd/Fe3O4 Nanoparticles by Use of Euphorbia Stracheyi Boiss Root Extract: A Magnetically Recoverable Catalyst for One-Pot Reductive Amination of Aldehydes at Room Temperature. **Journal of Colloid and Interface Science**, [*s. l.*], v. 464, p. 147–152, 15 Feb. 2016.

NEAMTU, Mariana *et al.* Functionalized Magnetic Nanoparticles: Synthesis, Characterization, Catalytic Application and Assessment of Toxicity. **Scientific Reports**, [*s. l.*], v. 8, n. 1, p. 1–11, 19 Apr. 2018. Disponível em: https://www.nature.com/articles/s41598-018-24721-4. Acesso em: 21 nov. 2023.

NEMATIAN, Tahereh *et al.* Lipase Immobilized on Functionalized Superparamagnetic Few-Layer Graphene Oxide as an Efficient Nanobiocatalyst for Biodiesel Production from Chlorella Vulgaris Bio-Oil. **Biotechnology for Biofuels**, [*s. l.*], v. 13, n. 1, p. 1–15, 20 Mar. 2020. Disponível em: https://biotechnologyforbiofuels.biomedcentral.com/articles/10.1186/s13068-020-01688-x. Acesso em: 22 nov. 2023.

NEMATIAN, Tahereh; SALEHI, Zeinab; SHAKERI, Alireza. Conversion of Bio-Oil Extracted from Chlorella Vulgaris Micro Algae to Biodiesel via Modified Superparamagnetic Nano-Biocatalyst. **Renewable Energy**, [*s. l.*], v. 146, p. 1796–1804, 1 Feb. 2020.

NETO, D.M.A. Davino M.A. *et al.* A Novel Amino Phosphonate-Coated Magnetic Nanoparticle as MRI Contrast Agent. **Applied Surface Science**, [*s. l.*], v. 543, p. 148824, 30 Mar. 2021.

NOQTA, Osama Abu *et al.* Recent Advances in Iron Oxide Nanoparticles (IONPs): Synthesis and Surface Modification for Biomedical Applications. **Journal of Superconductivity and Novel Magnetism**, [*s. l.*], v. 32, n. 4, p. 779–795, 20 Apr. 2019. Disponível em: http://link.springer.com/10.1007/s10948-018-4939-6. Acesso em: 3 jul. 2019.

PALAGUMMI, S.; YUAN, F. G. Magnetic Levitation and Its Application for Low Frequency Vibration Energy Harvesting. **Structural Health Monitoring (SHM) in Aerospace Structures**, [*s. l.*], p. 213–251, 1 Jan. 2016.

PANG, Yixiong *et al.* Facilely Synthesized Cobalt Doped Hydroxyapatite as Hydroxyl Promoted Peroxymonosulfate Activator for Degradation of Rhodamine B. **Journal of Hazardous Materials**, v. 384, p. 121447, 15 Feb. 2020.

PARANDI, Ehsan *et al.* Biodiesel Production from Waste Cooking Oil Using a Novel Biocatalyst of Lipase Enzyme Immobilized Magnetic Nanocomposite. **Fuel**, [*s. l.*], v. 313, p. 123057, 1 Apr. 2022.

PARK, J. H. *et al.* Effect of NaOH and Precursor Concentration on Size and Magnetic Properties of FeCo Nanoparticles Synthesized Using the Polyol Method. **AIP Advances**, [*s. l.*], v. 10, n. 11, p. 115220, 1 Nov. 2020. Disponível em: http://aip.scitation.org/doi/10.1063/5.0024622. Acesso em: 26 jan. 2021.

PAVITHRA, K. Grace *et al.* Removal of Colorants from Wastewater: A Review on Sources and Treatment Strategies. **Journal of Industrial and Engineering Chemistry**. [S.l.]: Korean Society of Industrial Engineering Chemistry. , 25 Jul. 2019

PEIMAN, Sahar; BAHARFAR, Robabeh; MALEKI, Behrooz. Immobilization of Trypsin onto Polyamidoamine Dendrimer Functionalized Iron Oxide Nanoparticles and Its Catalytic Behavior towards Spirooxindole-Pyran Derivatives in Aqueous Media. **Materials Today Communications**, [*s. l.*], v. 26, p. 101759, 1 Mar. 2021.

PIRKARAMI, Azam; OLYA, Mohammad Ebrahim. Removal of Dye from Industrial Wastewater with an Emphasis on Improving Economic Efficiency and Degradation Mechanism. **Journal of Saudi Chemical Society**, [*s. l.*], v. 21, p. S179–S186, 1 Jan. 2017.

PONRAJ, Rajesh *et al.* Morphology and Magnetic Properties of FeCo Alloy Synthesized through Polyol Process. **Applied Nanoscience (Switzerland)**, [*s. l.*], v. 10, n. 2, p. 477–483, 1 Feb. 2020. Disponível em: https://link.springer.com/article/10.1007/s13204-019-01128-9. Acesso em: 5 feb. 2021.

QIN, Hangdao *et al.* Degradation of Ofloxacin, Amoxicillin and Tetracycline Antibiotics Using Magnetic Core–Shell $MnFe_2O_4$@C-NH_2 as a Heterogeneous Fenton Catalyst. **Chemical Engineering Journal**, [*s. l.*], v. 396, p. 125304, 15 Sep. 2020.

QU, Jifeng *et al.* A Novel Magnetic Silica Supported Spinel Ferrites $NiFe_2O_4$ Catalyst for Heterogeneous Fenton-like Oxidation of Rhodamine B. **Chinese Chemical Letters**, [*s. l.*], v. 30, n. 6, p. 1198–1203, 1 Jun. 2019.

QUINN, Daniel M; SIKORSKI, R Steven. Enzymatic Rate Enhancements. **ELS**, 15 Jul. 2014. Disponível em: https://onlinelibrary.wiley.com/doi/full/10.1002/9780470015902.a0000717.pub3. Acesso em: 20 sep. 2023.

RAI, Prateek; GUPTA, Deepshikha. Magnetic Nanoparticles as Green Catalysts in Organic Synthesis-a Review. **Synthetic Communications**, [*s. l.*], v. 51, n. 20, p. 3059–3083, 18 Oct.

2021. Disponível em:
https://www.tandfonline.com/doi/abs/10.1080/00397911.2021.1968910. Acesso em: 7 nov. 2023.

RAJPUT, Jaspreet Kaur *et al.* CuFe$_2$O$_4$ Magnetic Heterogeneous Nanocatalyst: Low Power Sonochemical-Coprecipitation Preparation and Applications in Synthesis of 4H-Chromene-3-Carbonitrile Scaffolds. **Ultrasonics Sonochemistry**, [*s. l.*], v. 26, p. 229–240, 1 Sep. 2015.

RAO, Longjun *et al.* Highly Efficient Removal of Organic Pollutants via a Green Catalytic Oxidation System Based on Sodium Metaborate and Peroxymonosulfate. **Chemosphere**, [*s. l.*], v. 238, p. 124687, 1 Jan. 2020.

RIAL, Juliana Belen; FERREIRA, María Luján. Challenges of Dye Removal Treatments Based on IONzymes: Beyond Heterogeneous Fenton. **Journal of Water Process Engineering**, [*s. l.*], v. 41, p. 102065, 1 Jun. 2021.

RIETVELD, H.M.; IUCR. A Profile Refinement Method for Nuclear and Magnetic Structures. **Urn:Issn:0021-8898**, [*s. l.*], v. 2, n. 2, p. 65–71, 2 Jun. 1969. Disponível em: //scripts.iucr.org/cgi-bin/paper?a07067. Acesso em: 29 jan. 2023.

SAADATTALAB, Vahid *et al.* Effects of Metal Ions, Metal, and Metal Oxide Particles on the Synthesis of Hydrochars. **ACS Omega**, [*s. l.*], v. 5, n. 11, p. 5601–5607, 24 Mar. 2020. Disponível em: https://dx.doi.org/10.1021/acsomega.9b03926. Acesso em: 28 jan. 2021.

SAFAEI-GHOMI, Javad; EBRAHIMI, Seyyed Mohammad. Nano-Fe3O4–Cysteine as a Superior Catalyst for the Synthesis of Indeno[1,2-c]Pyrazol-4(1H)-Ones. **Polycyclic Aromatic Compounds**, [*s. l.*], v. 42, n. 5, p. 2693–2703, 2022. Disponível em: https://doi.org/10.1080/10406638.2020.1852276.

SALLES, R. C.M. *et al.* Surface Damage in Cystine, an Amino Acid Dimer, Induced by KeV Ions. **Journal of Chemical Physics**, [*s. l.*], v. 148, n. 4, p. 45107, 28 Jan. 2018. Disponível em: /aip/jcp/article/148/4/045107/75194/Surface-damage-in-cystine-an-amino-acid-dimer. Acesso em: 18 oct. 2023.

SÁNCHEZ-OTERO, M. Guadalupe *et al.* Immobilization in the Presence of Triton X-100: Modifications in Activity and Thermostability of Geobacillus Thermoleovorans CCR11 Lipase. **Journal of Industrial Microbiology and Biotechnology**, [*s. l.*], v. 35, n. 12, p. 1687–1693, 1 Dec. 2008. Disponível em: https://dx.doi.org/10.1007/s10295-008-0433-7. Acesso em: 18 oct. 2023.

SARNO, Maria; IULIANO, Mariagrazia. Highly Active and Stable Fe$_3$O$_4$/Au Nanoparticles Supporting Lipase Catalyst for Biodiesel Production from Waste Tomato. **Applied Surface Science**, [*s. l.*], v. 474, p. 135–146, 30 Apr. 2019.

SCHWAMINGER, Sebastian P. *et al.* Nature of Interactions of Amino Acids with Bare Magnetite Nanoparticles. **Journal of Physical Chemistry C**, [*s. l.*], v. 119, n. 40, p. 23032–23041, 8 Oct. 2015. Disponível em: https://pubs.acs.org/sharingguidelines. Acesso em: 3 nov. 2020.

SHARMA, Rimi; SINGHAL, Sonal. Photodegradation of Textile Dye Using Magnetically

Recyclable Heterogeneous Spinel Ferrites. **Journal of Chemical Technology & Biotechnology**, [*s. l.*], v. 90, n. 5, p. 955–962, 1 May 2015. Disponível em: https://onlinelibrary.wiley.com/doi/full/10.1002/jctb.4409. Acesso em: 21 nov. 2023.

SHI, Ning *et al.* Molecular Structure and Formation Mechanism of Hydrochar from Hydrothermal Carbonization of Carbohydrates. **Energy and Fuels**, [*s. l.*], v. 33, n. 10, p. 9904–9915, 17 Oct. 2019. Disponível em: https://pubs.acs.org/sharingguidelines. Acesso em: 28 jan. 2021.

SHOKUHFAR, A.; AFGHAHI, S. S.S. Size Controlled Synthesis of FeCo Alloy Nanoparticles and Study of the Particle Size and Distribution Effects on Magnetic Properties. **Advances in Materials Science and Engineering**, [*s. l.*], v. 2014, 2014.

SILVA, J. A. *et al.* Immobilization of Candida Antarctica Lipase B by Covalent Attachment on Chitosan-Based Hydrogels Using Different Support Activation Strategies. **Biochemical Engineering Journal**, [*s. l.*], v. 60, p. 16–24, 15 Jan. 2012.

SOARES, Paula I.P. *et al.* Design and Engineering of Magneto-Responsive Devices for Cancer Theranostics: Nano to Macro Perspective. **Progress in Materials Science**. [S.l.]: Elsevier Ltd. , 1 Feb. 2021

SOLTANI, Tayyebe; ENTEZARI, Mohammad H. Solar-Fenton Catalytic Degradation of Phenolic Compounds by Impure Bismuth Ferrite Nanoparticles Synthesized via Ultrasound. **Chemical Engineering Journal**, [*s. l.*], v. 251, p. 207–216, 1 Sep. 2014.

SOMWANSHI, Saurabh B.; SOMVANSHI, Sandeep B.; KHARAT, Prashant B. Nanocatalyst: A Brief Review on Synthesis to Applications. **Journal of Physics: Conference Series**, [*s. l.*], v. 1644, n. 1, p. 012046, 1 Oct. 2020. Disponível em: https://iopscience.iop.org/article/10.1088/1742-6596/1644/1/012046. Acesso em: 6 nov. 2023.

SOUFI, Amal *et al.* Heterogeneous Fenton-like Degradation of Tartrazine Using $CuFe_2O_4$ Nanoparticles Synthesized by Sol-Gel Combustion. **Applied Surface Science Advances**, [*s. l.*], v. 9, p. 100251, 1 Jun. 2022.

SPALDIN, Nicola A. **Magnetic Materials: Fundamentals and Applications**. 2. ed. [S.l.]: Cambridge University Press, 2010.

SPESSATO, Lucas *et al.* Optimization of Sibipiruna Activated Carbon Preparation by Simplex-Centroid Mixture Design for Simultaneous Adsorption of Rhodamine B and Metformin. **Journal of Hazardous Materials**, [*s. l.*], v. 411, p. 125166, 5 Jun. 2021.

SRIKHAOW, Assadawoot *et al.* Efficient Mercury Removal at Ultralow Metal Concentrations by Cysteine Functionalized Carbon-Coated Magnetite. **Applied Sciences, Switzerland**, v. 10, n. 22, p. 1–18, 2020.

STAUCH, Benjamin; FISHER, Stuart J.; CIANCI, Michele. Open and Closed States of Candida Antarctica Lipase B: Protonation and the Mechanism of Interfacial Activation. **Journal of Lipid Research**, [*s. l.*], v. 56, n. 12, p. 2348–2358, 1 Dec. 2015. Disponível em: http://www.jlr.org/article/S0022227520309536/fulltext. Acesso em: 19 oct. 2023.

SU, Yangyang *et al.* Crystalline Structures of L-Cysteine and l-Cystine: A Combined Theoretical and Experimental Characterization. **Amino Acids**, [*s. l.*], v. 54, n. 8, p. 1123–1133, 1 Aug. 2022. Disponível em: https://link.springer.com/article/10.1007/s00726-022-03144-6. Acesso em: 18 oct. 2023.

SUN, Xiaowei *et al.* Efficient Degradation of Methyl Orange in Water via Both Radical and Non-Radical Pathways Using Fe-Co Bimetal-Doped MCM-41 as Peroxymonosulfate Activator. **Chemical Engineering Journal**, [*s. l.*], v. 402, p. 125881, 15 Dec. 2020.

TANAKA, Shunsuke *et al.* Enhanced Peroxidase Mimetic Activity of Porous Iron Oxide Nanoflakes. **ChemNanoMat**, [*s. l.*], v. 5, n. 4, p. 506–513, 1 Apr. 2019. Disponível em: https://onlinelibrary.wiley.com/doi/full/10.1002/cnma.201800487. Acesso em: 21 nov. 2023.

TANG, Wen *et al.* Polyamine-Induced Tannic Acid Co-Deposition on Magnetic Nanoparticles for Enzyme Immobilization and Efficient Biodiesel Production Catalysed by an Immobilized Enzyme under an Alternating Magnetic Field. **Catalysis Science and Technology**, [*s. l.*], v. 9, n. 21, p. 6015–6026, 28 Oct. 2019. Disponível em: https://pubs.rsc.org/en/content/articlehtml/2019/cy/c9cy01350d. Acesso em: 11 nov. 2020.

TAO, Ping *et al.* A Novel Strategy for the Removal of Rhodamine B (RhB) Dye from Wastewater by Coal-Based Carbon Membranes Coupled with the Electric Field. **Separation and Purification Technology**, [*s. l.*], v. 179, p. 175–183, 31 May 2017.

TEO, Siow Hwa *et al.* Efficient Biodiesel Production from Jatropha Curcus Using $CaSO_4/Fe_2O_3-SiO_2$ Core-Shell Magnetic Nanoparticles. **Journal of Cleaner Production**, [*s. l.*], v. 208, p. 816–826, 20 Jan. 2019.

THIRUMAL, E. *et al.* Magnetic, Electric and Dielectric Properties of FeCo Alloy Nanoparticles Dispersed in Amorphous Matrix. **Physica Status Solidi (A)**, [*s. l.*], v. 207, n. 11, p. 2505–2510, 1 Nov. 2010. Disponível em: http://doi.wiley.com/10.1002/pssa.201000003. Acesso em: 28 jan. 2021.

TODERASCU, Luiza Izabela *et al.* Synthesis and Anti-Melanoma Activity of L-Cysteine-Coated Iron Oxide Nanoparticles Loaded with Doxorubicin. **Nanomaterials**, [*s. l.*], v. 13, n. 4, 2023.

TOUQEER, Tooba *et al.* Fe3O4-PDA-Lipase as Surface Functionalized Nano Biocatalyst for the Production of Biodiesel Using Waste Cooking Oil as Feedstock: Characterization and Process Optimization. **Energies**, [*s. l.*], v. 13, n. 1, p. 177, 31 Dec. 2019. Disponível em: https://www.mdpi.com/1996-1073/13/1/177/htm. Acesso em: 22 nov. 2023.

TZITZIOS, V. *et al.* Synthesis of Air Stable FeCo Nanoparticles. 1 Apr. 2011, [S.l.]: American Institute of PhysicsAIP, 1 Apr. 2011. p. 07A313. Disponível em: http://aip.scitation.org/doi/10.1063/1.3540387. Acesso em: 19 apr. 2021.

URBANSKI, T; HOFMAN, W; WITANOWSKI, M. The Infrared Spectra of Some Carbohydrates. **Bulletin de L'Academie Polonaise Des Sciences**, [*s. l.*], v. VII, n. 9, p. 619–624, 1959.

VADILLO, Virginia *et al.* High Magnetization FeCo Nanoparticles for Magnetorheological

Fluids with Enhanced Response. **Soft Matter**, [*s. l.*], v. 17, n. 4, p. 840–852, 28 Jan. 2021. Disponível em: https://pubs.rsc.org/en/content/articlehtml/2021/sm/d0sm01702g. Acesso em: 16 apr. 2021.

VEISI, Hojat *et al.* Palladium Nanoparticles Anchored Polydopamine-Coated Graphene Oxide/Fe_3O_4 Nanoparticles (GO/Fe_3O_4@PDA/Pd) as a Novel Recyclable Heterogeneous Catalyst in the Facile Cyanation of Haloarenes Using $K_4[Fe(CN)_6]$ as Cyanide Source. **Journal of Industrial and Engineering Chemistry**, [*s. l.*], v. 90, p. 379–388, 25 Oct. 2020.

VEISI, Hojat *et al.* Recent Advances in the Application of Magnetic Nanocatalysts in Multicomponent Reactions. **RSC Advances**, [*s. l.*], v. 13, n. 30, p. 20530–20556, 10 Jul. 2023. Disponível em: https://pubs.rsc.org/en/content/articlehtml/2023/ra/d3ra01208e. Acesso em: 7 nov. 2023.

VEISI, Hojat; HEMMATI, Saba; SAFARIMEHR, Parisa. In Situ Immobilized Palladium Nanoparticles on Surface of Poly-Methyldopa Coated-Magnetic Nanoparticles (Fe_3O_4@PMDA/Pd): A Magnetically Recyclable Nanocatalyst for Cyanation of Aryl Halides with $K_4[Fe(CN)_6]$. **Journal of Catalysis**, [*s. l.*], v. 365, p. 204–212, 1 Sep. 2018.

VEISI, Hojat; NAJAFI, Sepideh; HEMMATI, Saba. Pd(II)/Pd(0) Anchored to Magnetic Nanoparticles (Fe_3O_4) Modified with Biguanidine-Chitosan Polymer as a Novel Nanocatalyst for Suzuki-Miyaura Coupling Reactions. **International Journal of Biological Macromolecules**, [*s. l.*], v. 113, p. 186–194, 1 Jul. 2018.

VEISI, Hojat; PIRHAYATI, Mozhgan; KAKANEJADIFARD, Ali. Immobilization of Palladium Nanoparticles on Ionic Liquid-Triethylammonium Chloride Functionalized Magnetic Nanoparticles: As a Magnetically Separable, Stable and Recyclable Catalyst for Suzuki-Miyaura Cross-Coupling Reactions. **Tetrahedron Letters**, [*s. l.*], v. 58, n. 45, p. 4269–4276, 8 Nov. 2017.

VIAU, Guillaume; FIÉVET-VINCENT, Françoise; FIÉVET, Fernand. Monodisperse Iron-Based Particles: Precipitation in Liquid Polyols. **Journal of Materials Chemistry**, [*s. l.*], v. 6, n. 6, p. 1047–1053, 1 Jan. 1996. Disponível em: https://pubs.rsc.org/en/content/articlehtml/1996/jm/jm9960601047. Acesso em: 14 apr. 2021.

VOGT, Charlotte; WECKHUYSEN, Bert M. The Concept of Active Site in Heterogeneous Catalysis. **Nature Reviews Chemistry**, [*s. l.*], v. 6, n. 2, p. 89–111, 6 Jan. 2022. Disponível em: https://www.nature.com/articles/s41570-021-00340-y. Acesso em: 7 nov. 2023.

WACŁAWEK, S.; GRÜBEL, K.; ČERNÍK, M. Simple Spectrophotometric Determination of Monopersulfate. **Spectrochimica Acta Part A: Molecular and Biomolecular Spectroscopy**, [*s. l.*], v. 149, p. 928–933, 5 Oct. 2015.

WACŁAWEK, Stanisław *et al.* Revisit the Alkaline Activation of Peroxydisulfate and Peroxymonosulfate. **Current Opinion in Chemical Engineering**, [*s. l.*], v. 37, p. 100854, 1 Sep. 2022.

WAN, Qiqi *et al.* Oxidation of Organic Compounds by PMS/CuO System: The Significant Discrepancy in Borate and Phosphate Buffer. **Journal of Cleaner Production**, [*s. l.*], v. 339, p. 130773, 10 Mar. 2022.

WANG, Chao *et al.* Synthesis of High Magnetic Moment CoFe Nanoparticles via Interfacial Diffusion in Core/Shell Structured Co/Fe Nanoparticles. **Nano Research**, [*s. l.*], v. 2, n. 5, p. 380–385, 25 May 2009. Disponível em: http://link.springer.com/10.1007/s12274-009-9037-4. Acesso em: 2 apr. 2018.

WANG, Hui *et al.* Construction of $Fe_3O_4@\beta$-CD/g-C_3N_4 Nanocomposite Catalyst for Degradation of PCBs in Wastewater through Photodegradation and Heterogeneous Fenton Oxidation. **Chemical Engineering Journal**, [*s. l.*], v. 429, p. 132445, 1 Feb. 2022.

WANG, Jianlong; WANG, Shizong. Reactive Species in Advanced Oxidation Processes: Formation, Identification and Reaction Mechanism. **Chemical Engineering Journal**. [S.l.]: Elsevier B.V. , 1 Dec. 2020

WANG, Jingquan *et al.* Peroxymonosulfate Activation by Porous $BiFeO_3$ for the Degradation of Bisphenol AF: Non-Radical and Radical Mechanism. **Applied Surface Science**, [*s. l.*], v. 507, p. 145097, 30 Mar. 2020.

WEI, Shuoyun *et al.* Palladium Supported on Magnetic Nanoparticles as Recoverable Catalyst for One-Pot Reductive Amination of Aldehydes with Nitroarenes under Ambient Conditions. **Catalysis Communications**, [*s. l.*], v. 30, p. 40–44, 5 Jan. 2013.

XIA, Xinhui *et al.* A Review Study on Sulfate-Radical-Based Advanced Oxidation Processes for Domestic/Industrial Wastewater Treatment: Degradation, Efficiency, and Mechanism. **Frontiers in Chemistry**, [*s. l.*], v. 8, p. 592056, 27 Nov. 2020. Disponível em: www.frontiersin.org. Acesso em: 10 may 2021.

XIAO, Sa *et al.* Iron-Mediated Activation of Persulfate and Peroxymonosulfate in Both Homogeneous and Heterogeneous Ways: A Review. **Chemical Engineering Journal**. [S.l.]: Elsevier B.V. , 15 Mar. 2020

XIE, Wenlei; HAN, Yuxiang; WANG, Hongyan. Magnetic Fe_3O_4/MCM-41 Composite-Supported Sodium Silicate as Heterogeneous Catalysts for Biodiesel Production. **Renewable Energy**, [*s. l.*], v. 125, p. 675–681, 1 Sep. 2018.

XIE, Wenlei; HUANG, Mengyun. Immobilization of Candida Rugosa Lipase onto Graphene Oxide Fe3O4 Nanocomposite: Characterization and Application for Biodiesel Production. **Energy Conversion and Management**, [*s. l.*], v. 159, p. 42–53, 1 Mar. 2018.

XU, Yanting *et al.* FeCoOX/FeCoPX Nanoparticles Encapsulated N, S-Doped Porous Carbon Microspheres as Catalysts for the Elimination of Organic Pollutants. **Applied Surface Science**, [*s. l.*], v. 495, p. 143577, 30 Nov. 2019.

XUE, Xueyan *et al.* Biochar-Based Single-Atom Catalyst with Fe-N3O-C Configuration for Efficient Degradation of Organic Dyes by Peroxymonosulfate Activation. **ACS Applied Materials & Interfaces**, [*s. l.*], 30 Nov. 2023. Disponível em: https://pubs.acs.org/doi/full/10.1021/acsami.3c12518. Acesso em: 5 dec. 2023.

YANG, Bai *et al.* Chemical Synthesis of High-Stable Amorphous Feco Nanoalloys with Good Magnetic Properties. **Nanomaterials**, [*s. l.*], v. 8, n. 3, 1 Mar. 2018. Disponível em:

/pmc/articles/PMC5869645/. Acesso em: 20 apr. 2021.

YANG, Ruixia *et al.* Yolk-Shell Fe3O4@MOF-5 Nanocomposites as a Heterogeneous Fenton-like Catalyst for Organic Dye Removal. **Separation and Purification Technology**, [*s. l.*], v. 267, p. 118620, 15 Jul. 2021.

YAZDANI, Farshad; SEDDIGH, Mahdieh. Magnetite Nanoparticles Synthesized by Co-Precipitation Method: The Effects of Various Iron Anions on Specifications. **Materials Chemistry and Physics**, [*s. l.*], v. 184, p. 318–323, 1 Dec. 2016.

YI, Yufu *et al.* Hierarchically Porous Carbon Microsphere Doped with Phosphorus as a High Conductive Electrocatalyst for Oxidase-like Sensors and Supercapacitors. **ACS Sustainable Chemistry and Engineering**, [*s. l.*], v. 8, n. 26, p. 9937–9946, 6 Jul. 2020. Disponível em: https://dx.doi.org/10.1021/acssuschemeng.0c03978. Acesso em: 28 jan. 2021.

ZAHIRINEJAD, Sahar *et al.* Nano-Organic Supports for Enzyme Immobilization: Scopes and Perspectives. **Colloids and Surfaces B: Biointerfaces**, [*s. l.*], v. 204, p. 111774, 1 Aug. 2021.

ZAMANI KOUHPANJI, Mohammad Reza; STADLER, Bethanie J.H. H. A Guideline for Effectively Synthesizing and Characterizing Magnetic Nanoparticles for Advancing Nanobiotechnology: A Review. **Sensors**, v. 20, n. 9, p. 2554, 30 Apr. 2020. Disponível em: www.mdpi.com/journal/sensors. Acesso em: 5 mar. 2021.

ZAMANPOUR, Mehdi *et al.* Large-Scale Synthesis of High Moment FeCo Nanoparticles Using Modified Polyol Synthesis. **Journal of Applied Physics**, [*s. l.*], v. 111, n. 7, p. 07B528, 1 Apr. 2012. Disponível em: http://aip.scitation.org/doi/10.1063/1.3677773. Acesso em: 5 jul. 2019.

ZHANG, Mo *et al.* Supported Molybdenum on Graphene Oxide/Fe$_3$O$_4$: An Efficient, Magnetically Separable Catalyst for One-Pot Construction of Spiro-Oxindole Dihydropyridines in Deep Eutectic Solvent under Microwave Irradiation. **Catalysis Communications**, [*s. l.*], v. 88, p. 39–44, 5 Jan. 2017.

ZHANG, Rui *et al.* Singlet Oxygen-Dominated Non-Radical Oxidation in Biochar/Peroxymonosulfate System for Efficient Degradation of Tetracycline Hydrochloride: Surface Site and Catalytic Mechanism. **Journal of the Taiwan Institute of Chemical Engineers**, [*s. l.*], v. 145, p. 104815, 1 Apr. 2023.

ZHANG, Tao; ZHU, Haibo; CROUÉ, Jean-Philippe. Production of Sulfate Radical from Peroxymonosulfate Induced by a Magnetically Separable CuFe$_2$O$_4$ Spinel in Water: Efficiency, Stability, and Mechanism. **Environmental Science and Technology**, [*s. l.*], v. 47, n. 6, p. 2784–2791, 19 Mar. 2013. Disponível em: https://pubs.acs.org/doi/abs/10.1021/es304721g. Acesso em: 11 aug. 2021.

ZHANG, Ting *et al.* Modulating Physicochemical Properties of Collagen Films by Cross-Linking with Glutaraldehyde at Varied PH Values. **Food Hydrocolloids**, [*s. l.*], v. 124, p. 107270, 1 Mar. 2022.

ZHANG, Wenwen *et al.* Facile Synthesis of Porous NiCo$_2$O$_4$ Nanoflakes as Magnetic Recoverable Catalysts towards the Efficient Degradation of RhB. **RSC Advances**, [*s. l.*], v. 6,

n. 69, p. 64626–64633, 6 Jul. 2016. Disponível em: https://pubs.rsc.org/en/content/articlehtml/2016/ra/c6ra12706a. Acesso em: 30 nov. 2022.

ZHANG, Yang *et al.* Carbon Nanofibers Supported Co/Ag Bimetallic Nanoparticles for Heterogeneous Activation of Peroxymonosulfate and Efficient Oxidation of Amoxicillin. **Journal of Hazardous Materials**, [*s. l.*], v. 400, p. 123290, 5 Dec. 2020.

ZHAO, Guoqing *et al.* Iron-Based Catalysts for Persulfate-Based Advanced Oxidation Process: Microstructure, Property and Tailoring. **Chemical Engineering Journal**, [*s. l.*], p. 127845, 26 Nov. 2020.

ZHAO, Jujiao *et al.* Activation of Peroxymonosulfate by Metal–Organic Frameworks Derived $Co_{1+x}Fe_{2-x}O_4$ for Organic Dyes Degradation: A New Insight into the Synergy Effect of Co and Fe. **Journal of Environmental Chemical Engineering**, [*s. l.*], v. 9, n. 4, p. 105412, 1 Aug. 2021.

ZHOU, Yanbo; ZHANG, Yongli; HU, Xiaomin. Synergistic Coupling Co_3Fe_7 Alloy and $CoFe2O4$ Spinel for Highly Efficient Removal of 2,4-Dichlorophenol by Activating Peroxymonosulfate. **Chemosphere**, [*s. l.*], v. 242, p. 125244, 1 Mar. 2020.

ZHU, Jianyao *et al.* Efficient Degradation of Organic Pollutants by Peroxymonosulfate Activated with MgCuFe-Layered Double Hydroxide. **RSC Advances**, [*s. l.*], v. 9, n. 4, p. 2284–2291, 17 Jan. 2019. Disponível em: https://pubs.rsc.org/en/content/articlehtml/2019/ra/c8ra09841g. Acesso em: 5 dec. 2023.

ZUBIR, Nor Aida *et al.* Structural and Functional Investigation of Graphene Oxide-Fe_3O_4 Nanocomposites for the Heterogeneous Fenton-like Reaction. **Scientific Reports**, [*s. l.*], v. 4, n. 1, p. 1–8, 4 Apr. 2014. Disponível em: www.nature.com/scientificreports. Acesso em: 3 nov. 2020.

APPENDIX A – SUPPLEMENTARY MATERIALS FOR CHAPTER 2

Figure A1 – Linearized pseudo-first-order kinetic graph ($\ln(C/C_0)$) versus time) for the comparative study of the effects of NPs only, PMS only, and the mixture of both on rhodamine B degradation at 25°C using PMS at 2.0 mM and pH 7.0 (a). The graph also illustrates the effect of PMS dosage (without no pH control) (b) and initial pH with [PMS]=2.0 mM (c) on rhodamine B degradation at 25 °C. Additionally, (d) presents the fitting of the variation of PMS concentration with time in the pseudo-first-order kinetic model.
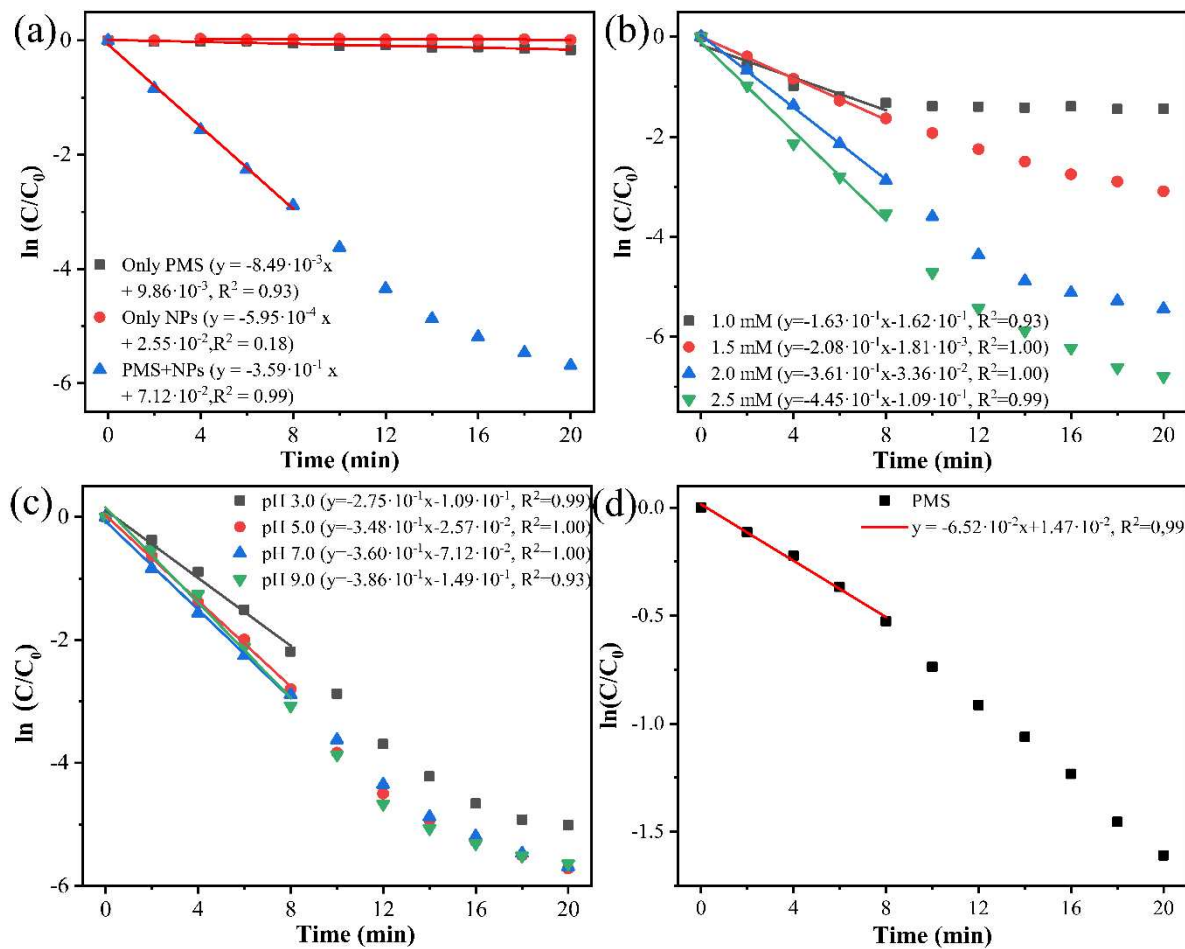
Source: the author.

Figure A2 – Linearized pseudo-first-order kinetic graph (ln(C/C₀) versus time) for the study of the effect of different scavengers – TBA (200 mM), Met-OH (2 M), L-hyst (15 mM) – in RhB degradation under optimized conditions (pH 7.0, [PMS] = 2.0 mM, 25°C) (a) and for the kinetics of each reuse cycle (b).

Source: the author.